Adaptive Estimation of Thermal Dynamics and Charge Imbalance in Battery Strings

by

Xinfan Lin

A dissertation submitted in partial fulfillment
of the requirements for the degree of
Doctor of Philosophy
(Mechanical Engineering)
in The University of Michigan
2014

Doctoral Committee:

Professor Anna G. Stefanopoulou, Chair
Technical Expert R. Dyche Anderson, Ford Motor Company
Professor Jessy W. Grizzle
Assistant Research Scientist Jason B. Siegel
Professor Jing Sun

To my mom,
for the unconditional love and support through all these years.

ACKNOWLEDGEMENTS

I would like to thank my advisor Professor Anna Stefanopoulou for all the advice, support and opportunities she offered me, which made it possible for me to finish this Ph.D. degree. I especially appreciate the way she motivated and encouraged me to explore the unknowns, which turned the research into a pleasant experience for me. My gratitude also go to the other members in my dissertation committee. In particular, Professor Jessy Grizzle and Professor Jing Sun equipped me with the critical tools to solve the most difficult problems in my research. Dr. Jason Siegel, whom I have known since he was still a graduate student, helped me with the laboratory set-up that laid the foundation of my work and was always willing to offer his advice and guidance as a pioneer and role model in the lab. Mr. Dyche Anderson mentored me in all aspects, from providing critical advices in industrial perspective to helping me improve English writing. I will never forget that he was doing all these for me on top of his managerial work at the Ford Motor Company. I also owe thanks to Professor James Freudenberg for guiding me through my first paper, which set the first and one of the most important milestones of my Ph.D. career.

My thanks then go to the Ford Motor Company, the United States Army Tank Automotive Research, Development and Engineering Center (TARDEC), the Automotive Research Center (ARC) at the University of Michigan, and the National Institute of Standard and Technology (NIST) for providing financial and technical support for my research.

I would also like to acknowledge the indispensable contribution to my research from the colleagues I have been working with. Thanks first go to the past and current members of the Battery Control Group in the Powertrain Control Lab (PCL), especially Hector Perez, Shankar Mohan, Youngki Kim, Nassim Samad, Boyun Wang, Yasha Parvini, Huan Fu, Thomas Smith, Patricia Laskowsky and Dr. Carmelo Speltino. Equally important are the help from the other members of PCL, including Jixin Chen, Toyoaki Matsuura, Rupert de Salis, Shyam Jade, Jacob Larimore, Patrick Gorzelic, Yi Chen and Dr. Erik Hellstrom. It is also my great honor to work with and learn from the outstanding individuals outside PCL, especially Professor

Levi Thompson, Professor Xiaohui Chen, Dr. Saemin Choi, Dr. Yonghua Li, Dr. Yi Ding, Dr. Matthew Castanier, Dr. Yi Ren and Sunbo Hwang.

I am also indebted to all my friends who gave me a colorful life here. It is them who made Ann Arbor my third hometown after Fuzhou and Beijing. Specifically, I want to thank those who started the journey here with me at the same time, especially Bo Yu, Jin Yan, Xianke Lin, Yingze Bao, Zhaoshi Meng, Lei Shao and Chenhui Shao; and those who I had a good time with on the basketball court, namely Roger Lv, Chang Liu, Hai Wang, Ye Tian, Li Zhao, Weichao Wang, Jiachao Liu, Zhengjia Lu, Shiwei Guo, Yiran Wang, Peng Tian, and Taozhi Li.

Last but not the least, I dedicate this dissertation to my mother, Haoping Lin, who is willing to sacrifice anything for her beloved son. Maternal love never diminishes. It only gets stronger with time.

TABLE OF CONTENTS

DEDICATION ii

ACKNOWLEDGEMENTS iii

LIST OF FIGURES viii

LIST OF TABLES xii

ABSTRACT xiii

CHAPTER

I. Introduction 1

1.1 Background on Lithium-ion Batteries 1
1.2 Challenges Facing Automotive Lithium Ion Batteries 2
1.3 Motivation 4
1.4 Estimation of Thermal Dynamics in Cylindrical Lithium Ion Batteries 5
1.4.1 Existing Thermal Models for Cylindrical Batteries . 5
1.4.2 Parameterization of the Two-state Thermal Model . 6
1.4.3 Temperature Estimation on the Battery Pack Level 7
1.5 Estimation of Battery Voltage and State of Charge 8
1.5.1 State of Art: SOC Estimation under Full Voltage Sensing 8
1.5.2 SOC and Voltage Estimation under Reduced Voltage Sensing 9
1.6 Dissertation Organization 10
1.7 Contributions 12

II. Adaptive Estimation of Single Cell Core Temperature and State of Health 14

2.1 Introduction 14
2.2 A Two-state Thermal Model for Cylindrical Batteries 15

2.3 Online Identification of the Two-state Battery Thermal Model 17
2.3.1 Parameterization Methodology 17
2.3.2 Application to the Battery Thermal Model 18
2.3.3 Experiment Validation 20
2.4 Adaptive Battery Core Temperature Estimation 27
2.5 Identification of the Time-varying Internal Resistance R_e . . . 31
2.5.1 Identification of the Temperature-dependent R_e . . 31
2.5.2 SOH Evaluation by Monitoring Long Term Growth in R_e 33
2.6 Conclusion 34

III. Temperature Estimation of Scalable Battery Strings 37

3.1 Introduction 37
3.2 A Scalable Thermal Model for 1-D Battery Strings 38
3.3 Model-based Estimation of the Battery String Temperatures . 40
3.3.1 Open-Loop Estimation 40
3.3.2 Closed-Loop Estimation 43
3.4 Sensor Deployment Strategy based on Observability Analysis 46
3.5 Observer Design and Sensor Deployment Strategy under Frugal Sensor Allocation 52
3.5.1 Problem Formulation for Temperature Estimation under Model Uncertainty 52
3.5.2 Robust H_∞ Observer Design 53
3.5.3 Observer Design for Minimizing the DC gain of the Estimation Error Transfer Function 57
3.5.4 Design Example: Optimal Observer Design to Estimate Temperature in a Battery String with 10 Cells and 1 Temperature Sensor 60
3.6 Conclusion 65

IV. Estimating Individual Cell States of Charge under Reduced Voltage Sensing 67

4.1 Introduction 67
4.2 Basic Idea and Model Assumptions 68
4.3 Observability Analysis 71
4.4 Candidate Nonlinear Observers 74
4.4.1 Extended Kalman Filter 76
4.4.2 Canonical Form Observer 78
4.4.3 Sliding Mode Observer 80
4.4.4 Extended Luenberger Observer 83
4.4.5 Newton Observer 85
4.4.6 Comparison of the Candidate Algorithms 86
4.5 Experimental Validation of the Newton Observer 87

4.6 Conclusions . . . 89

V. Estimating Individual Cell Capacities under Reduced Voltage Sensing . . . 91

5.1 Introduction . . . 91
5.2 Robustness of SOC Estimation under Imbalance and Uncertainty in Capacity and Resistance . . . 93
5.2.1 State of Charge Estimation Error under Model Uncertainty in Capacity and Resistance . . . 93
5.2.2 Robustness of SOC Estimation under Different Combinations of SOC and Capacity Imbalance . . . 95
5.3 Joint Estimation of Cell SOCs and Capacities . . . 101
5.3.1 Determination of Data Collection Strategy based on Cramer-Rao Bound . . . 101
5.3.2 SOC and Capacity Joint Estimation Algorithm based on the Newton-Raphson Method . . . 109
5.4 Overall Estimation Scheme - Combining Real-Time SOC Estimation and Off-line Joint Estimation of SOC and Capacity . 114
5.5 Conclusions . . . 116

VI. Conclusions and Future Work . . . 118

6.1 Conclusions . . . 118
6.2 Recommendations for Future Work . . . 119
6.2.1 Temperature Estimation on the Battery Pack Level 119
6.2.2 SOC and Capacity Estimation under Reduced Voltage Sensing . . . 119

APPENDIX . . . 122

BIBLIOGRAPHY . . . 125

LIST OF FIGURES

Figure

1.1	Battery Module of the Ford C-Max Hybrid.	3
1.2	Battery surface and core temperatures under a drive cycle.	4
2.1	Schematics of the single-cell radially-lumped thermal model.	15
2.2	Instrumentation of the battery core temperature.	21
2.3	Schematics of the flow chamber.	21
2.4	Scaled UAC current excitation.	22
2.5	Measured T_s and T_f under scaled UAC cycle.	23
2.6	Evolution of regressors ϕ in periodic steady state.	24
2.7	Evolution of the eigenvalues of U(t) in steady state.	25
2.8	Online Parameter Identification Results.	26
2.9	Experimental Validation.	27
2.10	Online Identification Scheme and Adaptive Observer Structure.	29
2.11	Response of the Closed loop Adaptive Observer.	30
2.12	Dependence of R_e on T_c.	31
2.13	Errors in R_e Estimation when the Temperature Varies Significantly.	32
2.14	Identification of Temperature Dependent Internal Resistance by the Least Square Algorithm with Non-uniform Forgetting Factors.	34

2.15 Adaptive Estimation of Battery with Temperature Dependent Internal Resistance by Forgetting Factors. 35

2.16 (Simulated) Identification of internal resistance subject to degradation. 36

2.17 Adaptive estimation of battery temperatures subject to degradation. 36

3.1 A possible battery pack configuration. 38

3.2 Simulated temperature profile of a 5-cell battery string under the UAC cycle. 40

3.3 Simulated battery pack temperature profile during shutdown. 42

3.4 Convergence of the open loop and the closed loop observers. 43

3.5 Convergence of the temperature estimation by the open loop and the closed loop observer. 44

3.6 Norms of the estimation errors for the open loop and the closed loop observer. 45

3.7 Sensor locations and observability. 48

3.8 Observability of the same sensor locations under different conditions. 49

3.9 The Worst-case H_∞ Norm of the Estimation Error Transfer Function under Different Sensor Locations. 61

3.10 Cases of ΔR_e giving the worst-case estimation errors under different sensor locations. 61

3.11 The Worst-case DC gain of the Estimation Error Transfer Function under Different Sensor Locations. 62

3.12 Cases of ΔR_e giving the worst-case estimation errors under different sensor locations. 62

3.13 Cases of ΔR_e giving the worst-case estimation errors under different sensor locations. 63

3.14 Drive-cycle Simulation. 65

3.15 Evolution of the maximum estimation error among all states over time during the drive-cycle simulation. 66

4.1 Voltage versus SOC relationship of a $LiFePO_4$ battery under a constant charging current. 69

4.2 Voltage trajectory over time under a constant charging current of the three SOC combinations in Table 4.1. 70

4.3 Voltage function $g(x)$ of a LiFePO4 battery under a constant charging current and its gradients. 74

4.4 Voltage function $g(x)$ of a LiNMC battery under a constant charging current and its gradients. 75

4.5 State of Charge Estimation of EKF under Reduced Voltage Sensing. 78

4.6 State of Charge Estimation of the Sliding Mode Observer under Reduced Voltage Sensing. 82

4.7 State of Charge Estimation of the Sliding Mode Observer under Reduced Voltage Sensing. 83

4.8 Measured SOCs and Voltages of Individual Cells under 5% SOC Imbalance. 88

4.9 Comparison of SOC Estimation with Experiment Measurement under 5% SOC Imbalance. 88

4.10 Comparison of Voltage Estimation with Experiment Measurement under 5% SOC Imbalance. 89

5.1 Data Collection Strategy for SOC and Capacity Joint Estimation. . 92

5.2 Singular Value σ_1 of the sensitivity matrix S at the End of Charging. 96

5.3 Singular Value σ_2 of the sensitivity matrix S at the End of Charging. 97

5.4 Simulated SOC Estimation under 5 Combinations of SOC Imbalance and Degradation. 98

5.5 Evolution of cell SOCs under constant charging current of 1 C when $x_{1,0} = 0.05 \quad x_{2,0} = 0, \quad Q_1 = Q_0, \quad Q_2 = 0.95Q_0$. 103

5.6 $\sigma_{CR,\%}$ of capacity and SOC estimation versus SOC variation covered by the voltage trajectory. 104

5.7 $\sigma_{CR,\%}$ of capacity and SOC estimation versus number of data points in the voltage trajectory. 105

5.8 $\sigma_{CR,\%}(x_{1,k+N})$ for all combinations of SOC and capacity imbalance in Eq.(5.22) when $\frac{NI\Delta t}{Q} = 90\%$ and $1/\Delta t = 0.2Hz$. 106

5.9 $\sigma_{CR,\%}(Q_1)$ for all combinations of SOC and capacity imbalance in Eq.(5.22) when $\frac{NI\Delta t}{Q} = 90\%$ and $1/\Delta t = 0.2Hz$. 106

5.10 Worst-case σ_{CR} of all considered combinations of SOC and capacity imbalance for voltage trajectories with different SOC variation and number of data points. 107

5.11 Directions of the observable and unobservable parts of capacity and SOC estimation for the case in Eq.(5.29). 111

5.12 Standard deviation of the estimate of Q_1 calculated based on simulation and Cramer-Rao bound. 113

5.13 Standard deviation of the estimate of Q_2 calculated based on simulation and Cramer-Rao bound. 113

5.14 Standard deviation of the estimate of $x_{1,k+N}$ calculated based on simulation and Cramer-Rao bound. 114

5.15 Standard deviation of the estimate of $x_{2,k+N}$ calculated based on simulation and Cramer-Rao bound. 114

5.16 Voltage trajectories used for real-time SOC estimation and off-line joint estimation of SOC and capacity. 115

LIST OF TABLES

Table

2.1 Initial guess and identification results of parameters. 24

2.2 Comparison of the identified parameters. 27

3.1 Minimum number of sensors rendering observability for battery strings with various lengths. 47

3.2 Number of sensor position combinations giving full observability for a string with 12 cells and 4 sensors. 49

4.1 State of Charge Combinations Giving the Same Total Voltage Instantaneously. 69

4.2 Comparison of Candidate Nonlinear Observers. 87

4.3 Final Estimates under 5% SOC Imbalance. 89

5.1 Robustness of SOC Estimation under Certain Combinations of Imbalance and Degradation. 100

5.2 Initial guess and identification results of parameters. 108

5.3 Comparison of the standard deviation calculated based on Cramer-Rao bound and simulation. 115

ABSTRACT

Adaptive Estimation of Thermal Dynamics and Charge Imbalance
in Battery Strings
by
Xinfan Lin

Chair: Prof. Anna G. Stefanopoulou

Effective battery management relies on accurate monitoring of battery states, including temperature, state of charge, and voltage among others. The large number of cells used in battery packs for vehicle applications require expensive monitoring hardware, which includes sensors, wiring, data acquisition and computation capacity. Due to the cost and complexity of the hardware, reduced sensing with limited and non-intrusive measurements is pursued by all manufacturers. In this dissertation, first, the monitoring of battery thermal dynamics based on only a limited number of sensors mounted on the surface of few cells is considered. Such scheme is augmented with model-based estimation techniques to capture the temperature gradient both across a single cell and among cells in the battery pack. Second, for lithium ion battery, the voltage of every single cell is currently measured to prevent overcharge and overdischarge. This dissertation develops nonlinear estimation techniques for reducing the individual cell voltage sensing requirement.

Specifically, in the first part of this dissertation, a model-based estimator using surface temperature measurement and continuously identified parameters is designed for adaptive prediction of the cell core temperature. The model-based estimation is then extended for the thermal network of cells inside a pack. Based on the battery string thermal model, the number of sensors and their location required for full observability is investigated, followed by an optimal observer design under the frugal sensor allocation and cell-to-cell variability.

In the second part of this dissertation, reduced voltage sensing, which relies on measuring the total voltage of multiple cells, is considered to replace the existing

single-cell voltage sensing system. The feasibility of state of charge estimation under reduced voltage sensing is first investigated based on observability analysis. Nonlinear observers are then designed for SOC estimation and validated by experiments. The results are later extended to the case when both SOC and capacity imbalance exist in the battery string due to non-uniform cell self-discharge rates, cell degradation, and manufacturing variability. The developed estimation technique provides the potential of reducing the voltage sensing in battery packs by half.

CHAPTER I

Introduction

1.1 Background on Lithium-ion Batteries

The past few decades have seen rapid increase in global energy consumption and deteriorating environmental conditions. Specifically, the energy consumption and the (energy-related) CO_2 emission increased by about 48% and 50% respectively over the past 20 years around the world [1]. The resulted energy and environmental issues have been some of the biggest challenges facing mankind today. One of the major contributor to these issues is the transportation sector, which accounted for about 70% of the oil consumption and 24% of the CO_2 emission in the U.S. in 2013 [2]. Vehicle electrification, including application of hybrid electric vehicles (HEV), plug-in electric vehicles (PHEV) and battery electric vehicles (BEV), has been considered as a promising way to reduce the fuel consumption and CO_2 emission in the transportation sector.

Batteries, which are the most common onboard energy storage system, are a major component of most electric vehicles (EV). Among all types of batteries, lithium ion batteries are nowadays widely used in EVs. Compared with other battery chemistries, such as lead acid and nickel metal hydride, lithium ion batteries have advantages over the following aspects [3, 4, 5, 6, 7]:

- higher energy density ($> 150Wh/kg$), which allows driving range between charges or reduce weight under the same driving range;
- higher open circuit voltage ($> 3.2V$), indicating higher power delivery;
- higher charge efficiency (97 - 99%) and lower self-discharge rate (5 - 10% per month), which equates to less energy waste;

- longer cycle life, which prolongs the lifetime and reduce the maintenance/replacement cost of the battery pack over vehicle life;
- no memory effect, avoiding significant capacity shrink due to repeated shallow charging and discharging.

Due to the above advantages, lithium ion battery has seen rapid growth in popularity. Nowadays, almost all major automakers have production electric vehicles powered by lithium ion battery [8, 9]. Besides in electric vehicles, lithium ion battery is also being considered for applications in conventional vehicles, e.g. in the engine start-stop system and as the replacement of the lead acid battery for the engine starter battery [10, 11, 12]. The global automotive lithium ion battery market is projected to reach $9 billion by 2015 [13].

Apart from automotive industry, lithium ion battery has also been widely applied in other fields. For example, it has a long history of being used as the main energy storage medium for consumer electronics and medical devices [14, 15]. It has also served as the backup or auxiliary power sources in aircraft and space applications [16, 17, 18]. Other applications include power generation plant, grid, power tools among others [19, 20].

1.2 Challenges Facing Automotive Lithium Ion Batteries

Some practical challenges prevent lithium ion battery-powered electric vehicles from replacing conventional internal combustion-powered vehicles at this time. Two of the prominent ones are safety and cost.

One of the important safety concerns is overcharge and overdischarge, which can be hazardous. Overcharge might lead to lithium deposition and electrolyte solvent decomposition, resulting in fire or even explosion [7, 21, 22]. Overdischarge may short the battery by causing copper dissolution and formation of dendrites [21, 22]. The other major safety concern is the vulnerability of lithium ion batteries to high temperature. Elevated temperature may trigger highly exothermic reactions, which will in turn increase the temperature further [3]. Such process occurring beyond certain temperature thresholds is referred to as thermal runaway [3, 23] and could lead to fire eventually.

As far as the cost is concerned, apart from that associated with materials and fabrication, issues related to management and design of battery systems add to the high price of EVs. First, because of the vulnerability of the lithium ion batteries,

safety measures are required for individual cells. The battery module of the Ford C-max hybrid electric vehicle is shown in Figure 1.1, where the cells are connected in series. It can be seen that the voltage of every single cell is measured to alert overcharge and overdischarge. Since the battery packs often consist of hundreds and even thousands of cells connected in series, single-cell voltage monitoring adds significant costs to the battery management system (BMS), including sensors, wiring and labor. Second, battery packs usually need to be sized with more energy and

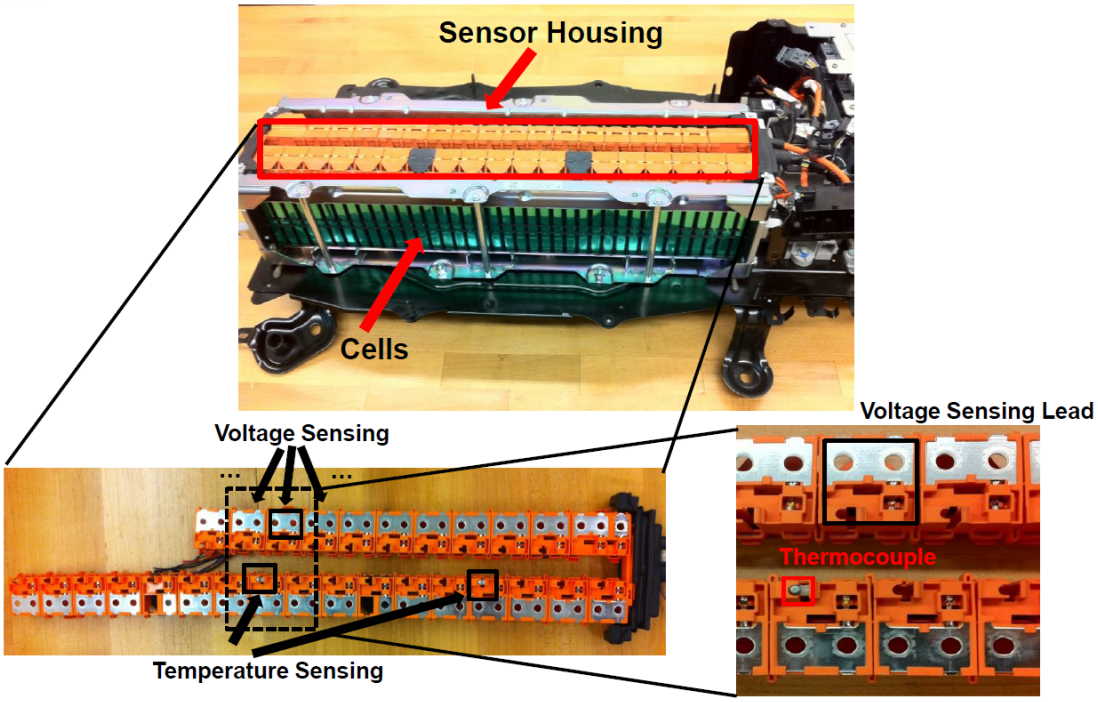

Figure 1.1: Battery Module of the Ford C-Max Hybrid.

power capacity than the requirement to accommodate degradation. As the battery ages, its internal resistance increases [16, 24] while its capacity shrinks [24, 25, 26]. Consequently, power and energy capacity of the battery will be reduced. In order to achieve the desired performance throughout the vehicle/battery life, the battery pack needs to be sized with redundant capacity in the design phase. The increase in the number or the size of the cells adds to the cost of the battery system.

1.3 Motivation

This dissertation is dedicated to exploring methods to enhance the safety of the lithium ion battery pack as well as reduce the cost of the battery management system.

First, better ways for monitoring the temperature of cylindrical batteries will be investigated. So far most BMSs only measure the surface temperature of some cells in the pack, but in fact the core temperature can be much higher, especially when the cells are operating under high currents. Measured surface temperature, T_s, and core temperature, T_c, of a 2.3 Ah $A123$ 26650 $LiFePO_4$/graphite battery under a realistic automotive drive cycle are shown in Figure 1.2. The maximum observed

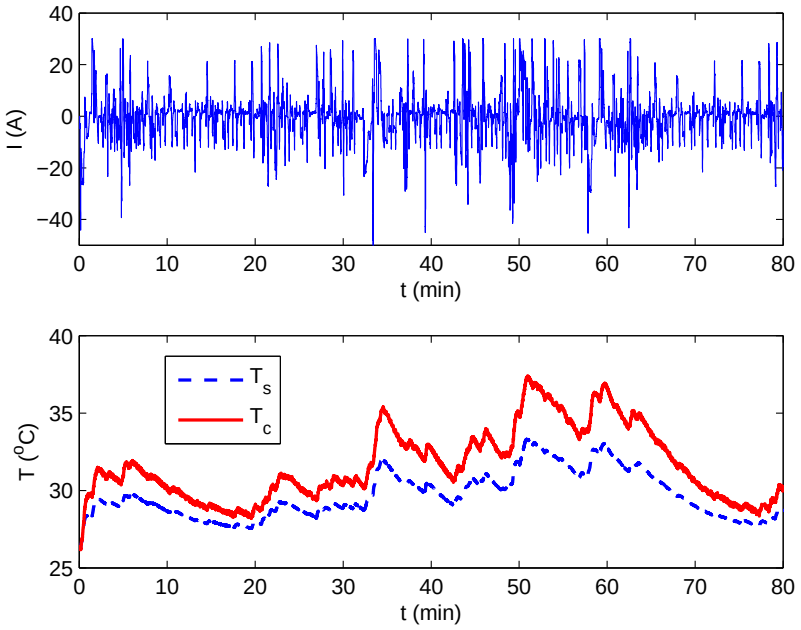

Figure 1.2: Battery surface and core temperatures under a drive cycle. (top: current profile of the drive cycle; bottom: surface and core temperatures)

temperature difference is more than 4 ^oC, which can be larger under higher current [27, 28]. Underestimating the temperature will put the battery at the risk of overheating. Apart from the safety concern, temperature monitoring is also the basis for battery thermal management strategies aiming at extending battery lifetime. It has been noticed that battery degradation is temperature dependent as the capacity and power fade is much more prominent at high temperature [3, 29, 30, 31]. Therefore, correct estimation of the battery core temperature can better assist the BMS strategy to avoid operation under high temperature [32]. In addition to serving the

thermal management, estimation of battery thermal dynamics can also be used for state of health (SOH) monitoring. As the internal resistance of the battery increases due to degradation, more heat will be generated during battery operation, resulting in temperature elevation. Therefore, it is possible to detect the growth in internal resistance through temperature monitoring. The identified resistance growth can be used to evaluate the SOH of the battery, and provide a reference for the life-extending battery management strategies.

Second, feasibility of reducing voltage sensing in BMS will be investigated. It has been mentioned that monitoring the voltages of all cells adds significant cost to the BMS. This cost may be reduced significantly if the cell voltage monitoring interval can be increased. For example, production HEVs with NiMH batteries typically only measure the total voltage of every 5 to 16 cells in series, and lead acid batteries are measured at every 6 cells or more. However, for lithium ion batteries, the need to prevent overcharge requires that reduced sensing should be pursued only if the individual cell SOCs and voltages can still be inferred accurately.

1.4 Estimation of Thermal Dynamics in Cylindrical Lithium Ion Batteries

In this section, problems concerning temperature monitoring of cylindrical lithium ion batteries are discussed. State of art of thermal modeling is first reviewed, and the two-state model is chosen as the best fit for cylindrical batteries. Parameterization of the two-state model is then identified as an issue to be addressed. In vehicle applications, a battery pack thermal model is needed for temperature estimation on the pack level, and temperature sensor deployment strategy can be investigated based on the model observability.

1.4.1 Existing Thermal Models for Cylindrical Batteries

Since temperature monitoring is a critical issue for lithium ion batteries, substantial efforts have been devoted to modeling the battery thermal dynamics.

Existing high fidelity thermal models can predict the detailed temperature distribution throughout a cell [33, 34, 35, 36]. In these models, an electrochemical model is often used to compute the heat generation by chemical reactions occurring during battery operation, and partial differential equations (PDE) are employed to calculate the resulting spatial and temporal temperature distribution. However, due to their

high computational load and limited capacity of the onboard processors, these models are not currently used in BMSs, where large numbers of cells need to be monitored.

At the other end of the spectrum in modeling complexity, single-state thermal models, featuring only the bulk (or average) temperature, are also widely used to capture the lumped thermal dynamics of the cell [36, 37, 38, 39]. This type of model has been adopted in onboard BMSs [40, 41] due to its computational efficiency. However, lumping the battery thermal dynamics to a single temperature might lead to over-simplification since the temperature in the battery core can be much higher than in the surface for cylindrical batteries [27]. Such temperature difference can be caused by various reasons. First, during battery operation, the battery core is exposed to the heat generated inside the cell while the battery casing is cooled down by the outside coolant. Second, physical properties of the electrode assembly and the battery casing, such as the heat capacity, are different. Thermal dynamics of the casing, which is usually made of metal, are much faster than those of the electrode assembly. The battery core temperature is more critical than the surface temperature since the breakdown and degradation take place in the electrode assembly.

A two-state thermal model [42] capturing both the surface and the core temperatures of a battery is a choice to better balance the computational load and model fidelity. In the model, the surface and core temperatures of a battery are defined as two states, and the thermal dynamics considered include the heat generation in the core, thermal conduction between the core and the surface, and the convective cooling between the surface and the outside coolant. Although this model is a simplification of a high fidelity model based on some assumptions, e.g. homogeneous temperature distribution in the core (electrode assembly), it appears to be an effective model for onboard application. Computing two states per cell is a manageable load for onboard processors, and provides the important benefit of capturing the critical core temperature.

1.4.2 Parameterization of the Two-state Thermal Model

The accuracy of the model parameters is of great importance since it determines the accuracy of the temperature estimation. Parameterization of the two-state thermal model remains an issue to be investigated.

In some attempts, model parameters are calculated based on the geometry of the battery and the volume-averaging physical properties of battery components [42]. Such approximation is not accurate due to the complicated layered structure of the cell and the interfaces between the layers.

The parameters can also be determined by fitting the model to data obtained from experiments [27] under designed current excitation. But such practice requires measurement of the battery core temperature, which is not be feasible for most batteries. In addition, this laboratory-oriented parameterization, while invaluable for determining the initial values of parameters, cannot ensure the parameter accuracy over battery lifetime. Some of the parameters, such as the internal resistance, may change due to degradation. In this case, parameter mismatch leads to inaccurate temperature estimation, and thus identification of present values of parameters is needed. Furthermore, if the internal resistance can be identified continuously over battery lifetime, the growth in internal resistance due to degradation can be detected to evaluate the state of health of the battery.

1.4.3 Temperature Estimation on the Battery Pack Level

So far thermal modeling of single-cell cylindrical battery has been discussed, but the BMS needs to monitor battery temperatures on the pack level. Cell temperatures in a pack can vary significantly [37, 43], due to pack geometry and cooling conditions among other factors. At this stage, most of the BMS rely on one or several temperature sensors for thermal management of the battery pack [44, 45, 46]. For example, in the battery module of the Ford C-max hybrid electric vehicle shown in Figure 1.1, only two thermocouples are installed to measure the surface temperature of two cells among a total of 38 cells in the module. The battery cooling (or heating) system is usually turned on or up when the measured temperature exceeds the predetermined thresholds. Such method could control the maximum temperature in the pack if the sensor is placed at the right spot, but it will have the following drawbacks. First, the temperature gradient across the battery pack, which is blind to the BMS, cannot be effectively controlled. Limiting temperature gradient is important for maintaining uniform performance among cells [3]. Second, with no prediction of the battery thermal dynamics, temperature control could be conservative at the cost of over-sized cooling hardware and non-optimal energy consumption of the cooling system. The model-based thermal management strategy, which uses a battery pack thermal model to predict and estimate the battery thermal dynamics, can be applied to address the above issues.

In a battery pack, cells are clustered in modules with physical connections, resulting in thermal interaction between cells. For example, heat conduction exists between adjacent cells either through the electrical connection or the air gap between them. In battery packs with active cooling, where coolant is cycled through the pack to

cool the cells, upstream cells will affect downstream cells through the coolant flow. Radiation might also occur between cell surfaces to transfer heat. These factors need to be considered in modeling the battery pack thermal dynamics.

Estimating battery temperatures solely based on the pack model, or open-loop temperature estimation, would be affected by noises or unknown initial conditions. More accurate estimation can be achieved with a closed-loop observer [47, 48], e.g. a Kalman filter, where surface temperature of some cells is measured and fed back to correct the estimation. Ideally, the measurements need to make the model observable. For economic reasons, it is desirable to use as few sensors as possible. Minimum number of sensors needed for a battery string and viable sensor locations can be determined by observability analysis of the pack thermal model.

1.5 Estimation of Battery Voltage and State of Charge

In this section, the issue of estimating individual cell SOC and voltage under reduced voltage sensing is introduced. State of art of SOC estimation under full voltage sensing is reviewed first. The motivation, challenges, and possible solutions of SOC estimation under reduced voltage sensing are then discussed.

1.5.1 State of Art: SOC Estimation under Full Voltage Sensing

As has been mentioned in Section 1.1, in order to prevent overcharge and overdischarge, voltages of all cells in the lithium ion battery pack are measured at present stage. Apart from voltage monitoring, the battery SOC, which is an indication of the amount of energy remained in the battery, also needs to be estimated. Model based observers have been widely adopted for SOC estimation. Most commonly used models for onboard applications include the coulomb counting model [49, 50], the equivalent circuit model [50, 51, 52], and the simplified electrochemical model [53, 54] among others. These models can be written in a state space representation with linear state equations and a nonlinear voltage output equation. The observers constructed based on these models include open-loop observers and closed-loop observers among others.

In open-loop observers, the battery SOC is calculated solely based on the model and the current input [49, 55]. Though easy to implement, open-loop observers are prone to noises in input measurement, uncertain initial conditions and errors in model parameters [56, 57]. This is especially true for SOC estimation, which is performed by simply integrating the input current over time. The (unstable) integrator will preserve errors in the initial guess of SOC and accumulate errors in current sensing.

Closed-loop observers, e.g. Kalman filters or Luenberger observers, can greatly improve the accuracy of the estimation [48, 58]. In closed-loop estimation, the battery SOC and voltage are first calculated based on the model and the current input. The estimated voltage is then compared with the real measurement and the error is fed back to correct the SOC estimation. Given an accurate model, the closed-loop observer can eliminate the errors induced by unknown initial conditions quickly. Even if the model parameters are not precise, the estimation errors of the closed-loop observer can be bounded within certain limits [56].

These advantages of the closed-loop observer (extended Kalman filter) are guaranteed if the voltage measurement renders the linearized battery model observability [59]. That is, the model states can be reconstructed based on the model and the output trajectory even if the initial conditions are unknown. In present BMSs, where measurement of single cell voltages make the battery model observable, the extended Kalman filter has been widely used based on various models [53, 60, 61, 62], achieving good estimation of both SOC and voltage.

1.5.2 SOC and Voltage Estimation under Reduced Voltage Sensing

To reduce the cost of the BMS for lithium ion batteries, it is highly desirable to replace the voltage sensing at every single cell (full sensing) with sensing at multiple cell increment (reduced sensing). Cells in a battery pack can be connected both in series and in parallel. Reduced voltage sensing is of interest in any battery cluster with two or more cells connected in series.

Under reduced voltage sensing, all the cells within one measuring increment can be viewed as a battery string whose total voltage is measured. To prevent overcharge and overdischarge, the SOC and voltage of every cell in the string need to be correctly estimated based on the measured total voltage. This goal can be easily achieved when all the cells have the same SOC and voltage. The single cell voltage can be obtained by simply dividing the total voltage by the number of cells, and the SOC can then be estimated based on the same methods used under full voltage sensing. However, when there is imbalance existing between cells, that is, cells have different SOCs and voltages, the task of SOC and voltage estimation will become far more complicated. To analyze this problem, a model of the series string needs to be constructed first. The states are composed by those of each single cell, and the model output is the summation of individual cell voltages. Existence of a solution to estimate the individual cell SOCs and voltages depends on the observability of the battery string model, which indicates the possibility of distinguishing model states based on the

model output [63]. If the battery string is proven to be observable, it is then possible to design an observer for the estimation problem.

There are various candidate algorithms that can potentially be applied for SOC and voltage estimation under reduced voltage sensing. The first category is the aforementioned closed-loop state observers, which are widely used under full voltage sensing. It needs to be pointed out that closed-loop state observers were originally invented for linear systems [48, 58], and later extended to nonlinear systems based on linearization. Such observers are usually referred to as the extended state observers, such as the extended Kalman filter (EKF) [59, 60]. To guarantee the asymptotic convergence of the state estimation under the closed-loop observers, in addition to satisfying the nonlinear observability condition, the battery string model also needs to be observable after linearization [59]. Such condition is easily satisfied under full voltage sensing, where the voltage of every single cell is measured. However, under reduced voltage sensing, it can be proven that the linearized battery models are generally not observable.

Candidate algorithms exist in addition to closed loop observers. Relevant algorithms and observer design approaches include and are not limited to the Newton observer [64, 65], canonical form observers based on observer error linearization [66, 67, 68], extended Luenberger observer [69], sliding mode observer [70, 71], high gain observers [72, 73], and Lyapunov-based observer design method [74].

1.6 Dissertation Organization

In this dissertation, Chapter II and Chapter III are dedicated to adaptive estimation of thermal dynamics in cylindrical batteries. Specifically, Chapter II addresses the problem on the single cell level, and Chapter III extends the solution to the battery pack level. Chapter IV and Chapter V investigate the issue of battery imbalance estimation under reduced voltage sensing, where Chapter IV focuses on estimating only the SOC imbalance, and Chapter V studies the more complicated case with both SOC and capacity imbalance.

In Chapter II, a two-state thermal model for single-cell cylindrical battery developed in [42] is first introduced. A method for model parameterization is then designed, which includes derivation of the parametric model, identifiability analysis and the least squares parameter identification algorithm. The methodology is then applied to an A123 26650 battery and validated with experimental data. The developed on-line parameterization method can be used for adaptive estimation of the

unmeasurable battery core temperature. Battery internal resistance is one of the parameters in the thermal model, whose value will change depending on operating condition or due to degradation. By incorporating a forgetting factor, the parameterization algorithm could identify the time-varying internal resistance, which provides a reference for battery state of health.

Temperature estimation is extended to the battery pack level in Chapter III. A thermal model of a one-dimensional battery string is first constructed based on the single-cell model in Chapter II and the considered thermal interaction between the cells. A closed-loop observer, which combines the model with measurement of some temperature states, can then be designed to estimate all the temperature states in the battery string. Ideally, the measurement needs to render all the temperature states observable. Therefore, temperature sensor deployment strategy is then studied based on observability analysis to determine the minimum number of sensors and their locations. Nevertheless, it is found that the number of sensors available in the battery pack of commercial electric vehicles is usually much less than the required number for observability. Optimal observer design approaches are then explored to achieve best observer performance under the unobservable condition imposed by the frugal sensor allocation.

Chapter IV is devoted to solving the SOC imbalance estimation problem under reduced voltage sensing. It is discovered that for battery chemistries with nonlinear voltage-SOC relationship, different combinations of SOC imbalance are distinguishable based on the total voltage evolution trajectory. Nonlinear observability analysis is then conducted to determine the observable conditions that need to be satisfied by the voltage-SOC relationship. Several candidate algorithms are investigated to solve the estimation problem, which include the extended Kalman filter, canonical form observer, sliding mode observer, extended Luenberger observer and Newton observer. The Newton observer is found to be the most suitable method, which is then applied to an A123 26650 $LiFePO_4$ battery and validated by experiment. Most of the analysis is conducted for reduced voltage sensing which measures two cell intervals under constant current charging conditions, targeting 50% reduction in voltage sensing. The methodology can be extended to longer intervals and real-world driving conditions subject to practical limitations.

The SOC imbalance algorithm developed in Chapter IV assumes known and equal capacity among cells. However, this assumption is not valid in many cases since capacity imbalance is also commonly presented in battery packs. This more complicated scenario is investigated in Chapter V. First, the robustness of the previously devel-

oped SOC estimation algorithm is analyzed under different combinations of SOC and capacity imbalance. It is found that SOC estimation is not always robust, which suggests the necessity of capacity estimation under reduced voltage sensing. Therefore, the Newton observer is then applied for joint estimation of SOC and capacity based on the measured total voltage trajectory. In order to guarantee the accuracy of capacity estimation, the voltage trajectory needs to cover a wide range of SOC variation and include many data points. The quantitative relationship between the measurement noise and the variance of the estimates is established based on Cramer-Rao bound analysis to guide the voltage data collection strategy. Furthermore, singular value decomposition is applied in the estimation algorithm to improve the robustness of joint SOC and capacity estimation. Finally, the overall estimation scheme, which combines the real-time SOC estimation algorithm developed in Chapter IV and the off-line SOC and capacity joint estimation algorithm designed in Chapter V, is discussed.

1.7 Contributions

The contributions of this dissertation include

- An adaptive observer for estimating the core temperature of a cylindrical battery is designed in Chapter II. The adaptive observer consists of an online parameter identifier, where the parameters of the two-state battery thermal model are identified based on onboard signals, and a closed-loop observer estimating the battery core temperature by using the identified parameters [75, 76]. Identified parameters include the internal resistance of the battery, which can be used to evaluate the battery SOH [76].

- Temperature sensor deployment strategy in a battery string is studied based on a string thermal model and observability analysis in Chapter III. The thermal model for a 1-D battery string is constructed based on the single cell model and thermal interaction between cells [77]. The minimum number of sensors and their locations required for full model observability is determined for battery strings with various lengths.

- Optimal observer design and sensor deployment strategy for temperature estimation of battery strings is also studied under frugal sensor allocation usually seen in commercial battery packs in Chapter III. Observer design faces two challenges in such case. First, the temperature states are not completely observable under the frugal sensor allocation. Second, estimation will be affected

by model uncertainty, such as that in battery internal resistance caused by cell-to-cell variability. Two robust observer design approaches are explored to find the optimal observer performance that can be achieved under such circumstance. It is guaranteed that the estimation error will not exceed the specified limits as long as the resistance uncertainty stays within the bounds.

- The feasibility of estimating individual cell SOCs and voltages under reduced voltage sensing is analyzed in Chapter IV. Based on nonlinear observability analysis, it is found that the individual cell SOCs are observable from the total voltage only if the voltage-SOC relationship of the battery chemistry is nonlinear. In such case, the SOC (imbalance) can be estimated based on the voltage trajectory over time.

- Nonlinear observers are designed for SOC estimation under reduced voltage sensing in Chapter IV. It is noted that the traditional linearization-based method for SOC estimation under full voltage sensing, such as the extended Kalman filter, is not applicable due to the lack of observability in the linearized battery model. The Newton observer, which is chosen from a pool of candidate algorithms, is designed and validated by experiment on a two-cell string under constant-current charging condition. The robustness of SOC estimation under model uncertainty caused by capacity and resistance imbalance is also investigated in Chapter V based on sensitivity analysis. The combinations of SOC and capacity imbalance that will lead to unrobust SOC estimation are identified.

- An algorithm for battery capacity estimation under reduced voltage sensing is developed based on the Newton observer in Chapter V. Compared with the capacity estimation method studied extensively in literature, the work in this dissertation has the following contributions. First, the designed algorithm can be used under reduced voltage sensing. Second, the requirements on the voltage data that could achieve certain estimation accuracy is studied based on Cramer-Rao bound analysis. The requirements include the SOC variation and the number of data points that need to be covered in the voltage trajectory.

CHAPTER II

Adaptive Estimation of Single Cell Core Temperature and State of Health

2.1 Introduction

An adaptive observer is designed in this chapter to monitor the core temperature of a cylindrical battery. First, an online parameterization algorithm [78] will be developed to identify the parameters of the two-state thermal model in [42]. The algorithm uses commonly measured onboard signals in a battery management system, such as the battery surface temperature, input current and coolant temperature, and is simple enough to be implemented on a typical automotive onboard controller. A closed loop observer is then built to estimate the battery core temperature using the parameters identified in real time.

The model with a constant internal resistance is investigated first, where the pure least square identification algorithm is sufficient for parameterization. In reality, the internal resistance of batteries can be temperature and/or state of charge (SOC) dependent [37, 79, 80, 81], and hence time-varying. The pure least square algorithm may introduce errors to the identification if the actual parameters are non-constant. Non-uniform forgetting factors are then augmented to identify the time-varying internal resistance.

Apart from the short-term variability due to conditions such as temperature, the internal resistance of lithium ion batteries may also increase over lifetime due to degradation. This is because the solid electrolyte interphase (SEI) may grow in thickness and change in composition [82, 83, 84], leading to reduction of SEI conductivity. Hence, the least square algorithm with non-uniform forgetting factors is also applied to track the long term growth of the internal resistance. The resistance growth is an important indication of the battery state of health (SOH), and can be used as a

reference for the onboard battery management system to extend battery life. Parameterization of battery models and adaptive monitoring of SOH have been explored previously in various seminal papers [85, 86, 87], mostly based on battery voltage dynamics. Our work is among the first ones to evaluate the battery SOH from a thermal perspective.

2.2 A Two-state Thermal Model for Cylindrical Batteries

The radial thermal dynamics of a cylindrical battery can be modeled as a classic heat transfer problem with heat generation located in the core and zero heat flux at the center, as shown in Figure 2.1. The two-state approximation of the radially

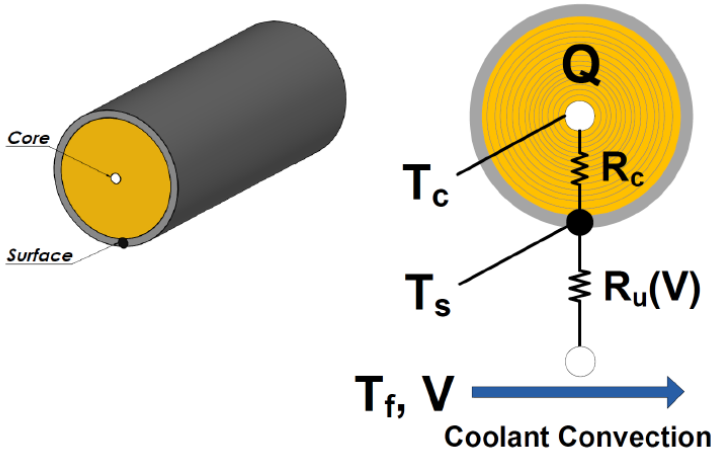

Figure 2.1: Schematics of the single-cell radially-lumped thermal model.

distributed thermal model is defined as [42, 76]

$$\begin{aligned} C_c\dot{T}_c =& I^2R_e + \frac{T_s - T_c}{R_c} \\ C_s\dot{T}_s =& \frac{T_f - T_s}{R_u} - \frac{T_s - T_c}{R_c}, \end{aligned} \tag{2.1}$$

where the two states are the surface temperature, T_s, and the core temperature, T_c. The temperature variation along the battery height is neglected here, assuming homogeneous longitudinal temperature distribution.

Heat generation is approximated as a Joule loss in the battery core, computed as the product of the current, I, squared and the internal resistance, R_e. The actual heat generation is a complex process involving various electrochemical reactions and

particle transport [3], complicated to model in detail. The simplification here can lead to cycle-dependent values for lumped resistance R_e, or even non-constant resistance within a single cycle. Such R_e can vary with conditions such as temperature, SOC and degradation [25, 37, 79, 80]. It is noted that heat generation can also be calculated based on the battery terminal voltage [81]. Heat exchange between the battery core and the surface is modeled as heat conduction over a thermal resistance, R_c, which is a lumped parameter aggregating the conduction and contact thermal resistance across the compact and inhomogeneous materials. A convection resistance R_u is modeled between the surface and the surrounding coolant to account for convective cooling. The value of R_u is a function of the coolant flow rate, and in some vehicle battery systems, the coolant flow rate is adjustable to control the battery temperature. Here, it is modeled as a constant as if the coolant flow rate is fixed to accommodate the required maximum cooling capacity. A model with a varying R_u has also been investigated in [75]. The rates of change of T_c and T_s depend on heat capacities of the battery core and casing. The parameter C_c is the heat capacity of the electrode assembly in the core, and C_s is the heat capacity of the aluminum casing.

The complete parameter set of this model includes C_c, C_s, R_e, R_c, and R_u, of which the values cannot be easily calculated. Consider the conduction resistance R_c as an example. Theoretically, R_c can be calculated based on the conductivity and dimensions of the wound cell electrode assembly and the aluminum casing. However, since the rolled electrodes are composed by the cathode, anode, current collectors and separator, it is difficult to obtain an accurate value for the overall conductivity. Moreover, R_c also includes the contact thermal resistance between the rolled electrodes and the casing, which involves various contact properties adding to the complexity of the calculation.

Therefore, a model identification algorithm is developed in the following section to obtain the phenomenological values of model parameters based on measurable model inputs and outputs.

2.3 Online Identification of the Two-state Battery Thermal Model

2.3.1 Parameterization Methodology

For model identification, a parametric model

$$z = \theta^T \phi \tag{2.2}$$

needs to be derived first by applying Laplace transformation to the model, where z is the observation, θ is the parameter vector and ϕ is the regressor [78]. Both z and ϕ should be measured signals.

With a parametric model, various algorithms can be chosen for parameter identification, such as the gradient and the least squares methods. The method of least squares is preferred for noise reduction [78]. The recursive least squares algorithm is applied in an online fashion, as parameters are updated continuously [78] by

$$\begin{aligned} \dot{\hat{\theta}} &= P\frac{\epsilon\phi}{m^2} \\ \dot{P} &= -P\frac{\phi\phi^T}{m^2}P \\ \epsilon &= z - \hat{\theta}^T\phi \\ m^2 &= 1 + \phi^T\phi, \end{aligned} \tag{2.3}$$

where m is a normalization factor to enhance the robustness of parameter identification. In some cases, to avoid differentiating the measured signals in observation z and regressors ϕ, a filter $\frac{1}{\Lambda(s)}$ needs to be applied. The parametric model will then become

$$\frac{1}{\Lambda}z = \theta^T\frac{1}{\Lambda}\phi. \tag{2.4}$$

Convergence and robustness of the identification are guaranteed if the regressors, ϕ, are stationary signals and satisfy the persistent excitation (PE) conditions [78]. The PE conditions are satisfied if there exist some time interval T_0, and positive number α_1 and α_0, such that

$$\alpha_1 I_M \geq U(t) = \frac{1}{T_0}\int_t^{t+T_0} \phi(\tau)\phi^T(\tau)d\tau \geq \alpha_0 I_M \quad \forall t \geq 0, \tag{2.5}$$

where I_M is an identity matrix with the same dimension as U(t) [78]. This criteria can be used to test whether a drive cycle can ensure robust parameter convergence.

2.3.2 Application to the Battery Thermal Model

In this section, the parameterization scheme described previously is applied to the cylindrical battery thermal model in (2.1). A parametric model is first derived by taking the Laplace transformation of (2.1) and replacing the unmeasured T_c with measured I, T_f, and T_s,

$$\begin{aligned} s^2T_s - sT_{s,0} = &\frac{R_e}{C_cC_sR_c}I^2 + \frac{1}{C_cC_sR_cR_u}(T_f - T_s) + \frac{1}{C_sR_u}s(T_f - T_s) \\ &- \frac{1}{C_cC_sR_c}\big((C_c + C_s)sT_s - C_sT_{s,0} - C_cT_{c,0}\big), \end{aligned} \tag{2.6}$$

where $T_{s,0}$ and $T_{c,0}$ are the initial surface and core temperatures. When the battery starts from thermal equilibrium, $T_{c,0}$ is the same as $T_{s,0}$, and (2.6) becomes

$$\begin{aligned} s^2T_s - sT_{s,0} = &\frac{R_e}{C_cC_sR_c}I^2 + \frac{1}{C_cC_sR_cR_u}(T_f - T_s) \\ &- \frac{C_c + C_s}{C_cC_sR_c}(sT_s - T_{s,0}) + \frac{1}{C_sR_u}s(T_f - T_s). \end{aligned} \tag{2.7}$$

It is assumed here that the coolant temperature, T_f, is regulated as a steady output of the air-conditioning unit and thus $sT_f = 0$, giving

$$s^2T_s - sT_{s,0} = \frac{R_e}{C_cC_sR_c}I^2 + \frac{1}{C_cC_sR_cR_u}(T_f - T_s) - \left(\frac{C_c + C_s}{C_cC_sR_c} + \frac{1}{C_sR_u}\right)(sT_s - T_{s,0}). \tag{2.8}$$

If T_f is a time-varying input to the model, sT_f should not be dropped. In this case, T_f can also be used as an input excitation in the parametric model. A second order filter should be applied to the observation and the regressors in (2.8) to make them proper. The filter takes the form

$$\frac{1}{\Lambda(s)} = \frac{1}{(s + \lambda_1)(s + \lambda_2)}, \tag{2.9}$$

where λ_1 and λ_2 are the time constants of the filter. The values of λ_1 and λ_2 can be chosen to filter the noises with frequencies higher than the temperature dynamics.

For the parametric model in (2.8), we have

$$\begin{aligned} Z(s) &= \frac{1}{\Lambda(s)}(s^2 T_s - s T_{s,0}) \\ \Phi(s) &= \frac{1}{\Lambda(s)}[I^2 \quad T_f - T_s \quad s T_s - T_{s,0}]^T \\ \theta &= [\alpha \quad \beta \quad \gamma]^T, \end{aligned} \tag{2.10}$$

where

$$\begin{aligned} \alpha &= \frac{R_e}{C_c C_s R_c} \\ \beta &= \frac{1}{C_c C_s R_c R_u} \\ \gamma &= -\left(\frac{C_c + C_s}{C_c C_s R_c} + \frac{1}{C_s R_u}\right). \end{aligned} \tag{2.11}$$

When implemented in real time, the identification algorithm is performed based on (2.3) with signals z and ϕ in continuous time domain, or based on equivalent formula in discrete time domain. For example, $z(t)$, whose Laplace transform is $\frac{s^2 T_s - s T_{s,0}}{\Lambda(s)}$, is obtained by calculating the convolution of $T_s(t) - T_{s,0}$ and the inverse Laplace transform of $\frac{s^2}{\Lambda(s)}$. In this way, calculation of the 2nd order derivative of T_s, $s^2 T_s$, which can be easily corrupted by noises, is avoided. The discrete-time version of the parameter identification algorithm is also provided in Appendix A. Such version is more convenient for application since it uses the sampled signals and does not need the filter.

By using the parametric model in (2.8), only three lumped parameters, α, β and γ, can be identified under persistent input excitation [78]. Prior knowledge of two of the five original physical parameters must be assumed to determine the rest three. Of the five physical parameters, the internal resistance R_e may vary due to aging and should be identified online. The conduction resistance R_c is difficult to estimate as explained previously. The convection resistance R_u will be influenced by the coolant flow conditions around the cell depending on the packaging. Therefore, it is not easy to obtain prior knowledge of those three parameters. The heat capacities C_c and C_s, which depend on the thermal properties and the mass of the rolled electrode assembly and the casing, are relatively constant over lifetime. In addition, the heat capacities only affect the transient response of the model without having any impact on the steady state temperatures. Consequently, C_c and C_s are chosen as the presumed parameters. With C_c and C_s presumed and α, β and γ identified, R_e, R_c and R_u can

be obtained by solving the following set of equations:

$$\begin{aligned} &\beta(C_c + C_s)C_s{R_u}^2 + \gamma C_s R_u + 1 = 0 \\ &R_c = \frac{1}{\beta C_s C_c R_u} \\ &R_e = \alpha C_c C_s R_c. \end{aligned} \tag{2.12}$$

The quadratic equation for R_u in (2.12) can lead to two solutions, and the right one can be decided based on the coolant flow conditions [88].

2.3.3 Experiment Validation

2.3.3.1 Experiment Set-Up and Measurements

Experiments have been conducted to validate the designed parameterization scheme. A 2.3Ah $A123^{\text{TM}}$ 26650 $LiFePO_4$/graphite battery is cycled with a Bitrode$^{\text{TM}}$ cycler under the control of a customized testing system by A&D Technology$^{\text{TM}}$. A Cincinnati Sub-Zero$^{\text{TM}}$ environmental simulation chamber is used to regulate the temperature of the coolant air flow around the battery.

T-type thermocouples are installed both on the battery casing to measure its surface temperature, and also inside the battery core to measure the core temperature. During the fabrication process of the 26650 cylindrical cell, the electrode assembly is wound up to form a roll, leaving a cavity in the center. To measure the core temperature, the battery was drilled inside an argon-filled glove box through to its central cavity, where the thermocouple was inserted, as shown in Figure 2.2. The battery was then sealed and taken out of the glove box for experiments.

Inside the thermal chamber, the battery was placed in a designed flow chamber as shown in Figure 2.3, where a fan was mounted at one end to regulate the air flow around the cell. A T-type thermocouple is placed near the battery inside the flow chamber to measure the air flow temperature T_f.

A driving cycle, the Urban Assault Cycle (UAC) [89], is applied as the current excitation to the battery in galvanostatic mode. The UAC is originally a velocity cycle for military vehicles. The current profile for a battery pack of a hybrid military vehicle under UAC is derived in [89] by applying a certain power management strategy. The type of battery used in the experiment ($LiFePO_4$ 26650) is different from the one in [89], hence the UAC cycle is rescaled for the experiments. The original 20-minute cycle is repeated 4 times to let the battery temperature reach periodic steady state. The scaled drive cycle current is plotted in Figure 2.4. The normalized unit of C-rate

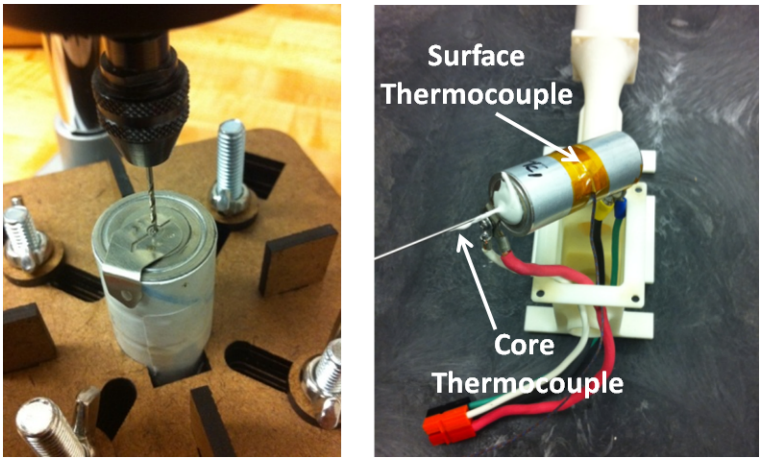

Figure 2.2: Instrumentation of the battery core temperature. (left: drill press setup of the battery; right: installation of the thermocouples)

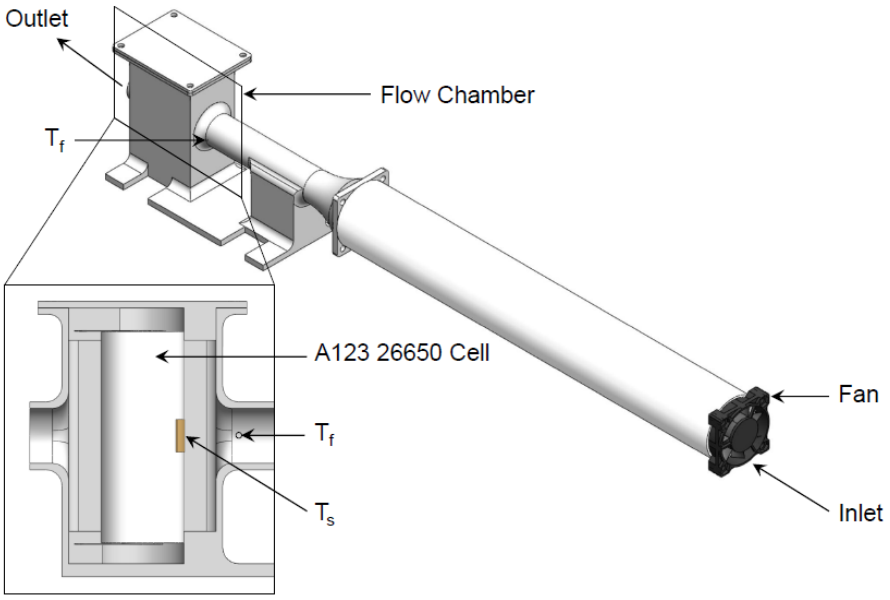

Figure 2.3: Schematics of the flow chamber.

is commonly used to describe the load applied to the battery, and 1 C corresponds to the magnitude of the current that depletes the battery in one hour (in this case 2.3 A). Negative current indicates discharge as the energy is drawn from the battery to drive the vehicle, and positive current represents the regenerative braking during which the battery is charged. The discharge load is fairly evenly distributed between 1 C and 7 C, except at around -8 C which indicates rapid acceleration. The charge load is mostly below 7C and occasionally reaches above 10 C during drastic braking.

SOC evolution under this cycle is plotted in Figure 2.4, showing a decrease from about 50% to roughly 35%. Temperature of the thermal chamber is controlled at 26

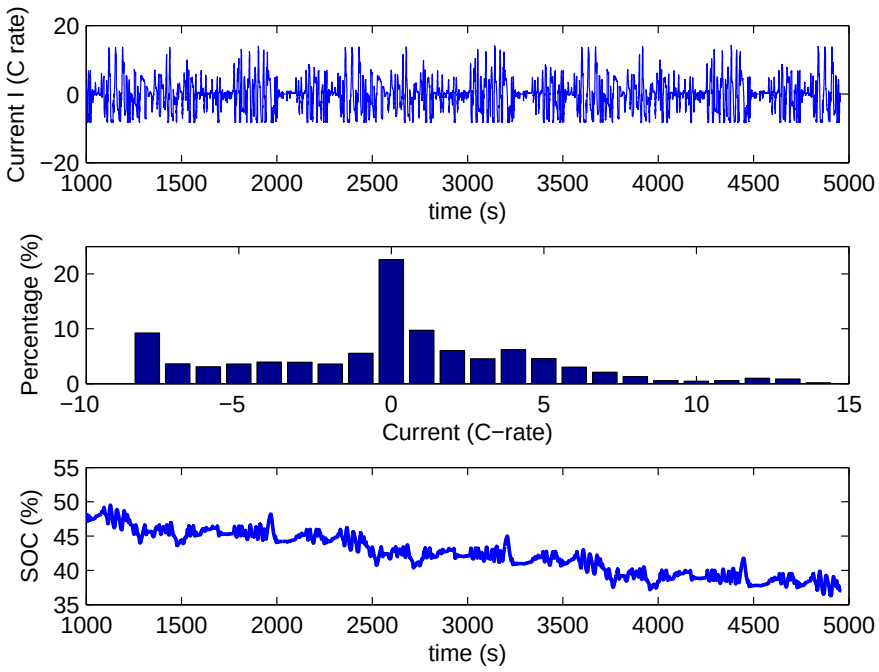

Figure 2.4: Scaled UAC current excitation. (top: currents in time; middle: histogram of the currents; bottom: SOC variation under the cycle)

^oC. The resulting battery surface temperature T_s and air flow temperature T_f are measured and recorded by the data acquisition system. The measured T_s and T_f are plotted in Figure 2.5, which along with I will be used for parameter identification.

2.3.3.2 Persistent Excitation of Input Signals

The criteria in (2.5) is first applied to check if the UAC cycle satisfies the PE condition, which requires the regressors to be stationary signals first. As can be seen in Figure 2.5, the surface temperature T_s will vary periodically after the battery finishes the warm-up phase at about 1000 second. Consequently, the regressors, which include the filtered I^2, $T_f - T_s$, and sT_s, will become stationary signals, as shown in Figure 2.6. The U(t) matrix can then be calculated to check the persistent excitation conditions.

Since the current input consists of repeated UAC cycles (each lasting for 1200s), U(t) only need to be calculated over a time interval $T_0 = 1200s$ for $1000s \leq t \leq 2200s$.

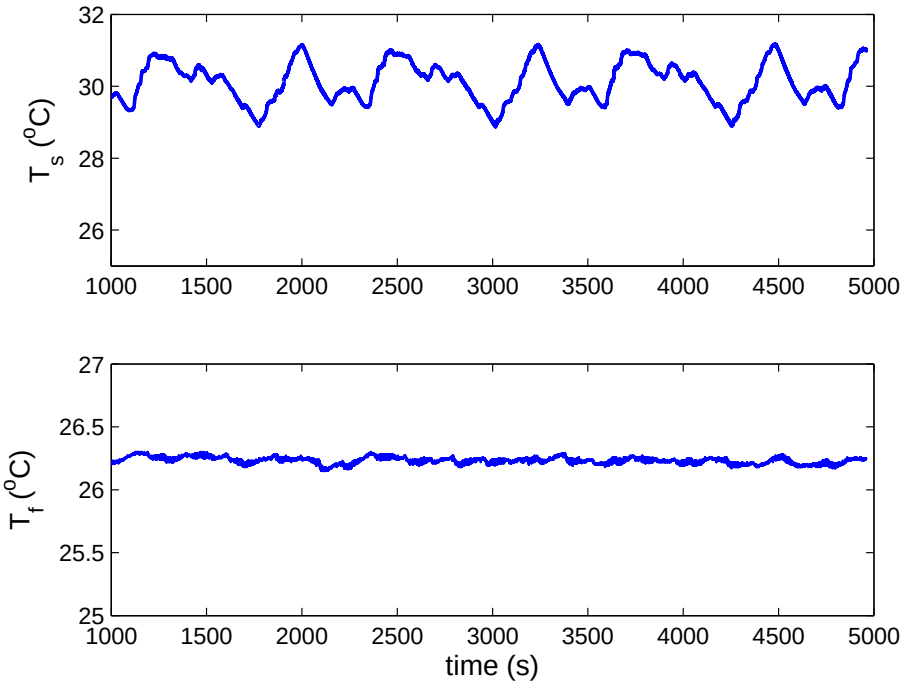

Figure 2.5: Measured T_s and T_f under scaled UAC cycle. (top: surface temperature T_s; bottom: flow temperature T_f)

It is noted that in this case, U(t) is not a diagonal matrix, and thus its eigenvalues are calculated to check the persistent excitation conditions. The smallest and the largest eigenvalues of U(t), λ_{max} and λ_{min}, are plotted in Figure 2.7. It can be concluded from Figure 2.7 that α_1 in (2.5) can be found as 0.086 s^{-1}, which is the maximum of $\lambda_{max}(t)$, and α_0 as 2.4×10^{-4} s^{-1}, which is the minimum of $\lambda_{min}(t)$. Consequently, under the UAC cycle, the regressors satisfy the conditions of persistent excitation. Furthermore, α_0 is related to the speed of the convergence for parameter identification. Specifically, when the gradient method is used, $2\alpha_0^{-1}$ is the upper limit of the time constant of the parameter convergence [78], which would be

$$\tau \leq 8333s \tag{2.13}$$

in this case. Based on (2.13), the 90% settling time for the convergence under the gradient search algorithm is expected to be less than $19186s$. It is noted that $19186s$ is a rather conservative estimation of the convergence time, in real application, the convergence is usually accelerated by increasing the adaptive gain [78, 90].

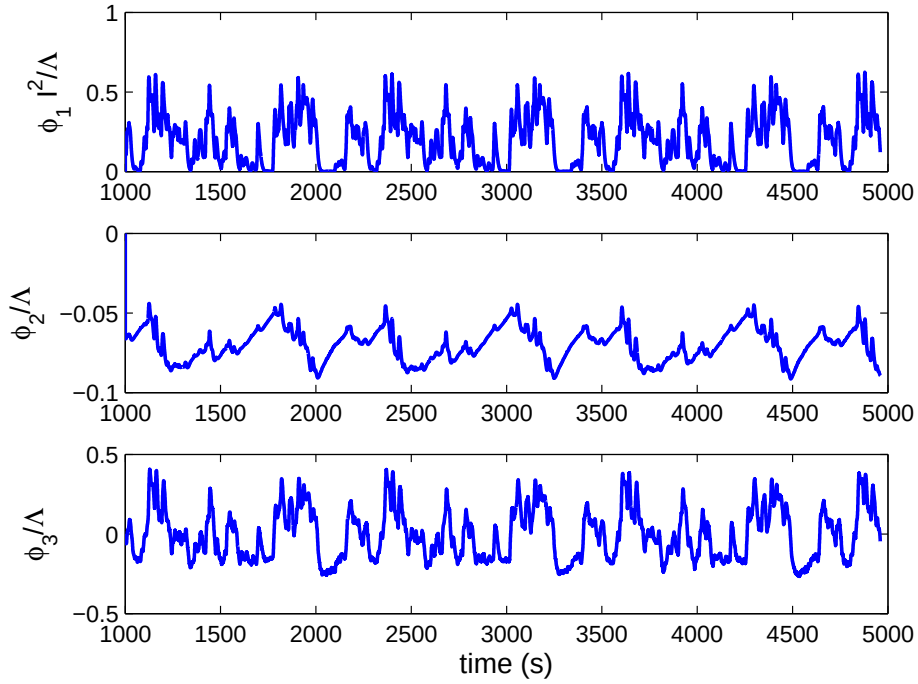

Figure 2.6: Evolution of regressors ϕ in periodic steady state.

Parameters	$R_u(KW^{-1})$	$R_e(m\Omega)$	$R_c(KW^{-1})$
Initial Guess	1.5	30	0.5
ID Results	3.03	11.4	1.83

Table 2.1: Initial guess and identification results of parameters.

2.3.3.3 Results and Discussion

The measured signals I, T_s and T_f in Figure 2.4 and Figure 2.5 are used for recursive least squares parameterization. The three parameters to be identified, R_u, R_e and R_c, are initialized with the initial guess values in Table 2.1. The core and surface heat capacities C_c and C_s need to be presumed based on some reference. In [27], a lumped bulk heat capacity, C_p, is identified for the same type of battery. Here, since C_p is split into C_c and C_s, C_c, taking most of the thermal mass, is assumed to be 67 JK^{-1}, slightly smaller than C_p in [27]. The heat capacity of the battery surface, C_s, is calculated to be 4.5 JK^{-1} based on the dimensions of the aluminum casing and the specific heat capacity of aluminum.

Results of the recursive identification are plotted in Figure 2.8. It is noted that the identification procedures are started after the first 1000 seconds when the temperature

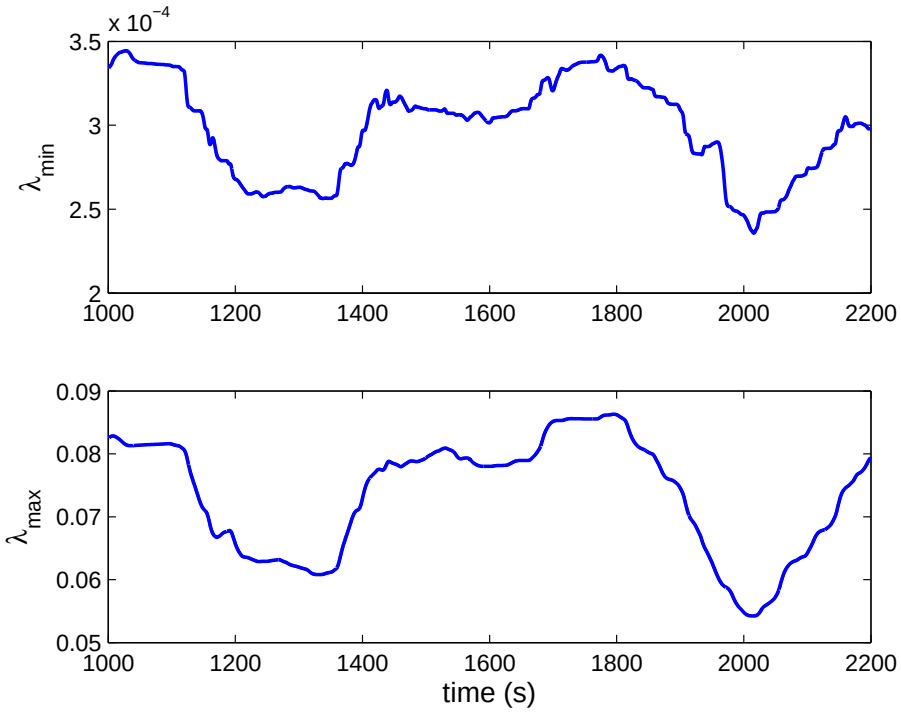

Figure 2.7: Evolution of the eigenvalues of U(t) in steady state. (top: smallest eigenvalue; bottom: largest eigenvalue)

enters periodic steady state. It can be seen that starting at some random initial values, the 3 parameters converge to the values listed in Table 2.1. The upper plot in Figure 2.8 shows the convergence of the lumped parameters α, β and γ in (2.8), and the lower plot shows the convergence of the physical parameters R_u, R_c and R_e, which are obtained by solving (2.12). It is noted that the convergence time is within the range (less than 19186 s) discussed in Section (2.3.3.2), which is strictly speaking only valid for the gradient method. The convergence rate is accelerated here by increasing the initial adaptive gain P_0 [90, 91], which is the initial value of $P(t)$ in (2.3).

For validation purpose, the identified parameters are applied to (2.1) to estimate both the battery surface temperature T_s and the core temperature T_c. The estimation is then compared with the measurement, as plotted in Figure 2.9. The estimated surface temperatures T_s match the measurement exactly, since T_s is directly used for identification. It is noted that the measured core temperature T_c also agrees closely with the measured T_c (which was not used for parameterization), showing the validity of the identified model parameters. Once the parameterization scheme is validated, it can be run in the onboard battery management system to estimate the

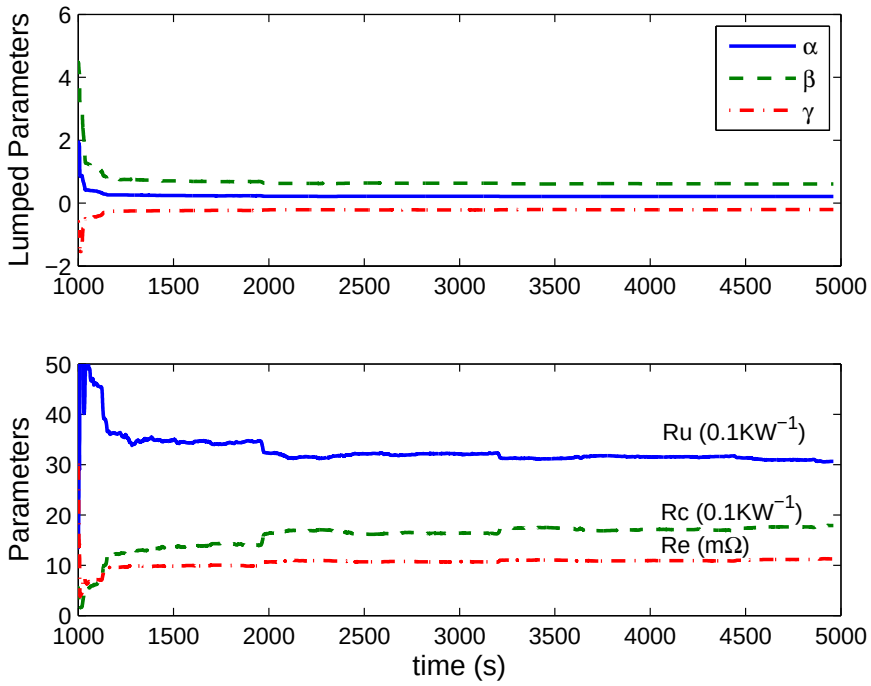

Figure 2.8: Online Parameter Identification Results. (top: convergence of the lumped parameters; convergence of the original parameters)

core temperature in real time without actually measuring it (as in the lab set-up).

The identification results are compared to those in [27], where thermal parameters of the same battery are identified based on the measurement of both surface and the core temperatures under designed current inputs. In [27], the battery is modeled with a single dynamic state (the core temperature), and the surface temperature is related to the core temperature with an algebraic equation by assuming the surface heat capacity to be zero. Heat generation in [27] is pre-calculated by resistive heat dissipation (due to ohmic voltage drop) plus entropic heat. In this work, the entropic heat is ignored and the heat generation is captured by the identified resistance, R_e. It is noted that the entropic heat is generally small comparing to the resistive heat, especially in the middle SOC range here as shown in Figure 2.4. Table 2.2 summarizes the comparison between the thermal parameters identified in [27] and in this work. It can be seen that the identified value of the conduction resistance, R_c, is smaller than that in [27]. This is probably because the surface temperature in this work is measured at the aluminum casing instead of at the outside paper cover (as in [27]), which indicates better heat conduction. The identified convection resistance between

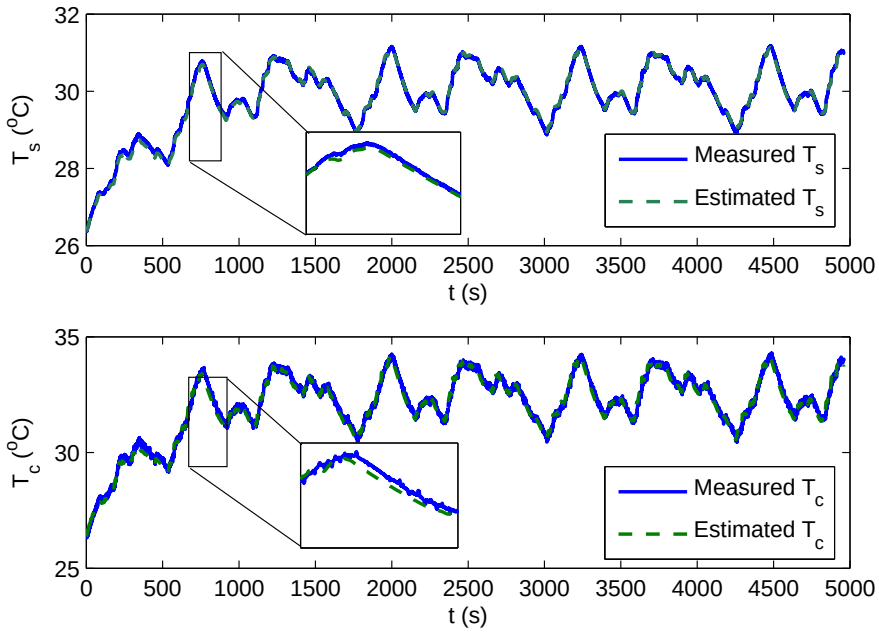

Figure 2.9: Experimental Validation. (top: estimated surface temperature T_s vs. measured; bottom: estimated core temperature T_c vs. measured)

Parameters	Value	Equivalence in [27]	Value
$R_c(KW^{-1})$	1.83	$R_{in}(KW^{-1})$	$3.2 \sim 3.4$
$R_u(KW^{-1})$	3.03	$R_{out}(KW^{-1})$	$8.4 \sim 9.1$
$C_c(JK^{-1})$	67	$C_p(JK^{-1})$	$73 \sim 78$
$C_s(JK^{-1})$	4.5	-	-

Table 2.2: Comparison of the identified parameters.

the surface and the coolant R_u is significantly smaller than that in [27]. Such difference can be explained by the fact that during the experiment, air flow is constantly blown into the flow chamber by the fan to enhance the convective cooling, whereas in [27], the battery is cooled by natural convection.

2.4 Adaptive Battery Core Temperature Estimation

In control applications, an observer is often designed based on a plant model to estimate the states of the plant, especially those not measured, e.g. the core temperature T_c of the battery in this case. Such model based observers can be categorized

as either an open loop observer or a closed loop observer. For a linear system

$$\dot{x} = Ax + Bu, \tag{2.14}$$

where x are the states and u are the inputs, an open loop observer is simply

$$\dot{\hat{x}} = A\hat{x} + Bu, \tag{2.15}$$

as the estimated states $\hat{x}$ are calculated by the model solely based on the inputs u. For the battery thermal model specifically, we have

$$\begin{aligned} x &= [T_c \quad T_s]^T \\ u &= [I^2 \quad T_f]^T \\ A &= \begin{bmatrix} -\frac{1}{R_c C_c} & \frac{1}{R_c C_c} \\ \frac{1}{R_c C_s} & -\frac{1}{C_s}(\frac{1}{R_c} + \frac{1}{R_u}) \end{bmatrix} \\ B &= \begin{bmatrix} \frac{R_e R_c}{C_c} & 0 \\ 0 & \frac{1}{R_u C_s} \end{bmatrix}. \end{aligned} \tag{2.16}$$

However, the estimation by such an open loop observer can often be corrupted by unknown initial conditions and noises in input measurement. To address such issues, a closed loop observer is often designed based on the model and feedback of some measurable outputs [47] as

$$\begin{aligned} \dot{\hat{x}} &= A\hat{x} + Bu + L(y - \hat{y}) \\ y &= Cx + Du \\ \hat{y} &= C\hat{x} + Du, \end{aligned} \tag{2.17}$$

where y are the measured system outputs, $\hat{x}$ and $\hat{y}$ are estimated states and outputs, L is the observer gain, and A, B, C and D are model parameters. For the battery thermal model, since the surface temperature T_s is measured, we have

$$\begin{aligned} C &= [0 \quad 1] \\ D &= 0. \end{aligned} \tag{2.18}$$

It is noted that the difference between the measured and the estimated output is used as the feedback to correct the estimated states. Comparing with an open loop observer, the closed loop observer can accelerate the convergence of the estimated

states to the real states under unknown initial conditions, e.g. a Luenberger observer [47], or optimize the estimation by balancing the effect of unknown initial conditions and noises, e.g. a Kalman filter [48].

By taking the structure of a closed loop observer, an adaptive observer is then designed based on the certainty equivalence principle [78],

$$\begin{aligned} C_c\dot{\hat{T}}_c =& I^2\hat{R}_e + \frac{\hat{T}_s - \hat{T}_c}{\hat{R}_c} + l_1(T_s - \hat{T}_s) \\ C_s\dot{\hat{T}}_s =& \frac{T_f - \hat{T}_s}{\hat{R}_u} - \frac{\hat{T}_s - \hat{T}_c}{\hat{R}_c} + l_2(T_s - \hat{T}_s), \end{aligned} \tag{2.19}$$

where $\hat{T}_s$ and $\hat{T}_c$ are the estimated surface and core temperatures, and the observer parameters $\hat{R}_e$, $\hat{R}_c$ and $\hat{R}_u$ are taken from the online identification results in Section (2.3.3). The block diagram of the adaptive observer is shown in Figure 2.10. The

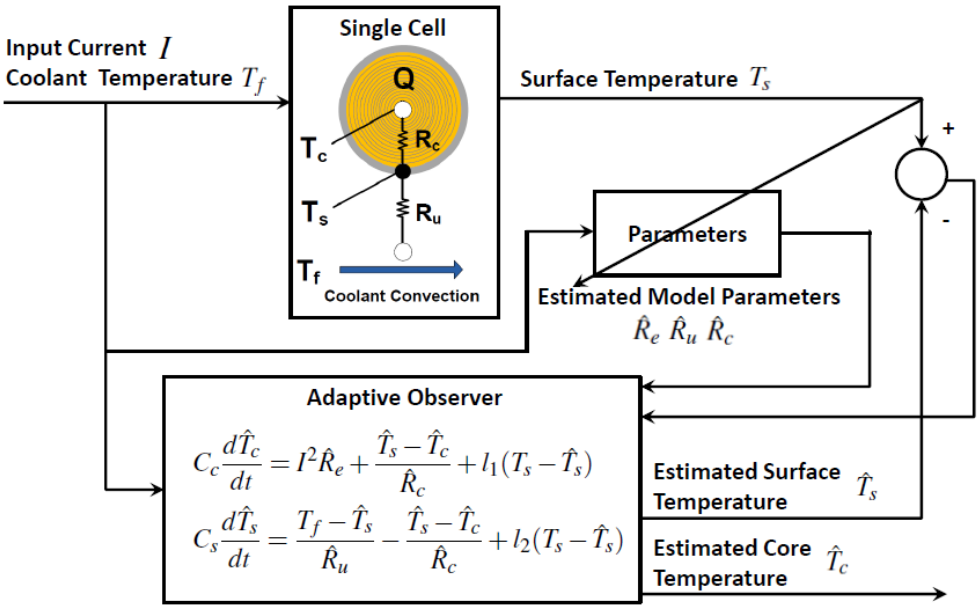

Figure 2.10: Online Identification Scheme and Adaptive Observer Structure.

measured input current I, coolant temperature T_f, and surface temperature T_s are fed into the parameter identifier to estimate model parameters R_u, R_e and R_c. The adaptive observer uses the estimated parameters to estimate the core and the surface temperatures. The estimated T_s is then compared to the measurement and the error is fed back to correct the estimation. Both the parameter and temperature estimation is updated at each time step.

The data in Section (2.3.3) are used to test the response of the adaptive observer, as plotted in Figure 2.11. The initial estimated temperatures of the adaptive observer are set at 30 ^oC for both the surface and the core, whereas the correct value is 26 ^oC, and the parameters are initialized with the initial guess values in Table 2.1. It can be seen from Figure 2.11 that the estimated surface temperature converges to the real value much faster than the estimated core temperature. The reason is that the surface temperature T_s is accessible by the adaptive observer both via parameter identification and closed loop error feedback, and thus the observer can adjust its estimation of T_s quickly based on direct reference of the measurement. But for the core temperature T_c, which is not measured, its estimation accuracy depends on the model fidelity. Therefore, convergence of T_c will only happen after the identified parameters converge to the correct model parameters (at approximately 3000 seconds).

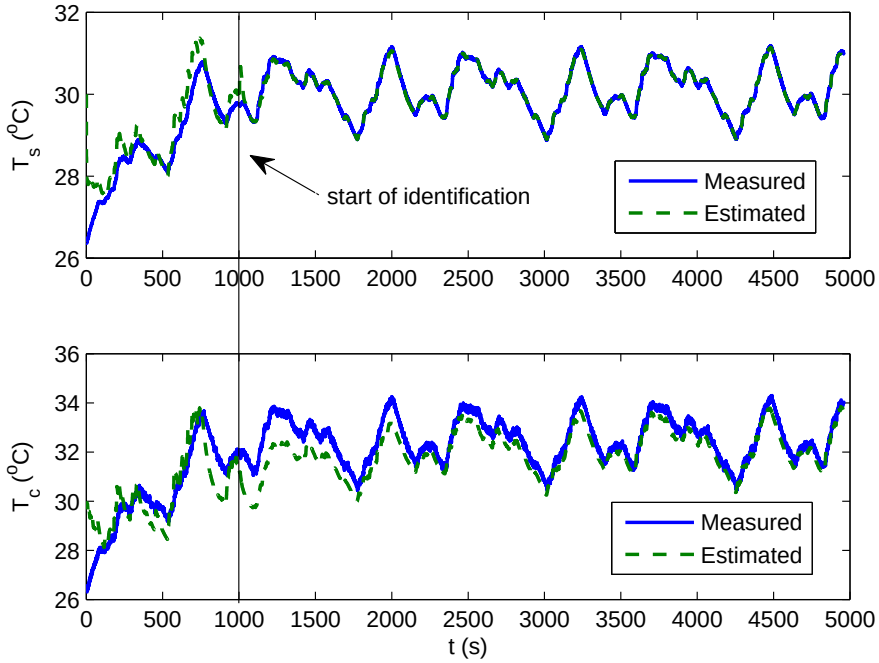

Figure 2.11: Response of the Closed loop Adaptive Observer. (top: adaptive estimation of the surface temperature vs. measurement; bottom: adaptive estimation of the core temperature vs. measurement)

2.5 Identification of the Time-varying Internal Resistance R_e

2.5.1 Identification of the Temperature-dependent R_e

For most lithium ion batteries, their internal resistance R_e is temperature and SOC dependent [37, 38, 80]. In general cases, R_e is high under low temperature and when the SOC is close to 0% or 100%. An exponential function is often used to describe the relationship between R_e and the battery (core) temperature T_c, as

$$R_e = R_{e,ref} \exp\left(\frac{T_{ref}}{T_c}\right), \tag{2.20}$$

where $R_{e,ref}$ is the reference resistance value at a certain reference temperature T_{ref}, and T_{ref} and T_c are in K. It is noted that the change in resistance with respect to SOC is negligible in the normal vehicle battery operating range ($20\% - 80\%$ SOC), and thus such dependency is not considered here. The relationship between R_e and T_c described by (2.20) is plotted in Figure 2.12, by taking $R_{e,ref} = 0.091\ m\Omega$ and $T_{ref} = 1543\ K$. Due to the temperature dependency, in real application, R_e will be

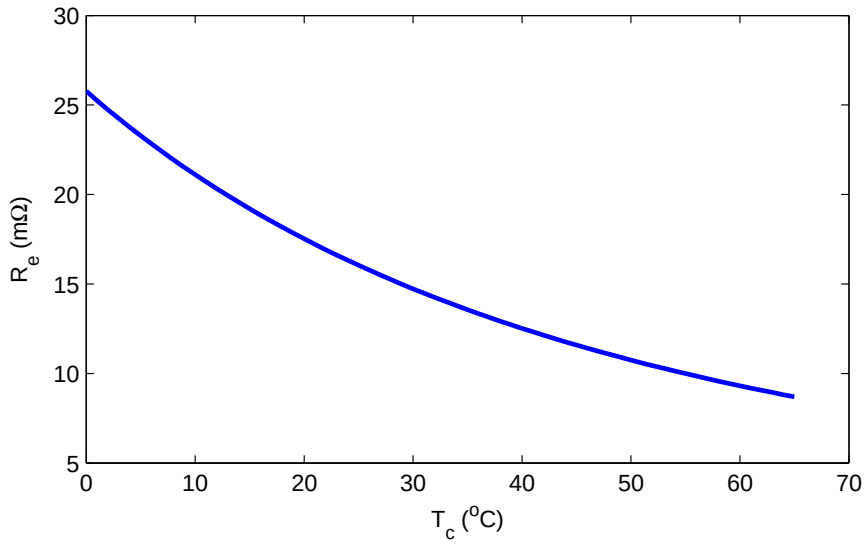

Figure 2.12: Dependence of R_e on T_c.

varying as the temperature fluctuates. Such variation can not be neglected when the power demands are high and dramatically varying. Simulation is used in this section for illustration. Simulated variation of R_e due to T_c fluctuation under a drastic current cycle is shown in Figure 2.13. It can be seen that the drastic current variation creates

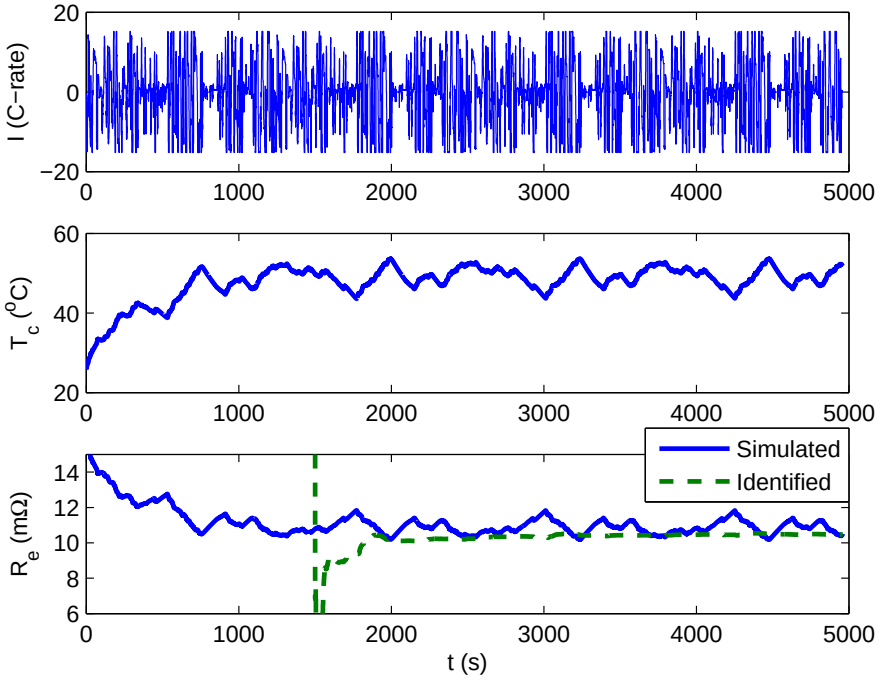

Figure 2.13: Errors in R_e Estimation when the Temperature Varies Significantly. (top: drive cycle current; middle: fluctuation of the battery core temperature; bottom: errors in R_e identification)

a 10 ^oC of fluctuation in the battery core temperature T_c. The resulting variation of R_e is about 20% as shown by the solid line in the bottom plot of Figure 2.13.

Since the least squares identification algorithm in (2.3) identifies each parameter as a constant, when R_e is varying, errors will be observed in R_e identification as shown in Figure 2.13. Such errors will affect the estimation of other parameters and eventually corrupt the estimation of the core temperature T_c. To address such issue, a least squares algorithm with forgetting factors is designed to identify R_e as a time-varying parameter.

When forgetting factors are adopted, most parts of the least square algorithm will be the same as (2.3), except that

$$\dot{P}(t) = \eta^T P(t)\eta - P(t)\frac{\phi(t)\phi^T(t)}{m^2(t)}P(t), \tag{2.21}$$

where η is the forgetting factor matrix [78]. The least square identification algorithm tries to find the optimal parameters that best fit the inputs and outputs over the

whole data set. A pure least square algorithm treats each data point as equal, no matter if it is acquired most recently, or obtained much earlier. However, when a forgetting factor is applied, the data points are weighted differently. Specifically, the newly acquired data are favored over the older ones. In the form shown in (2.21), the weight of the data will decay exponentially with time, and the larger the forgetting factor is, the faster the decay will be. Consequently, the least square algorithm can track the parameter variation based on newer data. Of the three lumped parameters, namely α, β, and γ in (2.7), only α is related to time varying R_e, and all the others are constant. Therefore, non-uniform forgetting factors should be adopted with the η matrix designed as

$$\eta = \begin{bmatrix} \eta_1 & 0 & 0 \\ 0 & 0 & 0 \\ 0 & 0 & 0 \end{bmatrix}, \tag{2.22}$$

where η_1 is the forgetting factor associated with α (and hence R_e).

Simulation has been conducted with $\eta_1 = 0.25$, and the identification results are shown in Figure 2.14. It can be seen that the identified R_e can follow the simulated varying R_e after the recursive identification algorithm with forgetting factors is activated at 1500s. As shown in Figure 2.15, the adaptive observer, taking the varying parameters identified online, can estimate the battery core temperature T_c accurately after the identified R_e converges to the simulated R_e at around $3700s$.

2.5.2 SOH Evaluation by Monitoring Long Term Growth in R_e

The growth in battery internal resistance due to degradation is a process that occurs slowly over the battery lifetime. Such growth can be substantial over hundreds of cycles or days according to [16, 25, 24]. The recursive least square algorithm with forgetting factors can also track the long term growth of the internal resistance, which can be used as an indication for the battery state of health.

In this paper, slow growth in internal resistance is simulated to test the capability of the identification algorithm to detect such growth. The internal resistance R_e, originally a function of the core temperature T_c, is now augmented with a term which is linearly increasing over time. The drive cycle used for simulation is the same as shown in the upper plot of Figure 2.13, but is repeated for 350 times and the rate of growth in internal resistance is set at 0.14%/cycle. Although not modeled here, the rate of degradation may also increase with the temperature according to [16, 25, 24].

The results of the online identification are shown in Figure 2.16. It can be seen

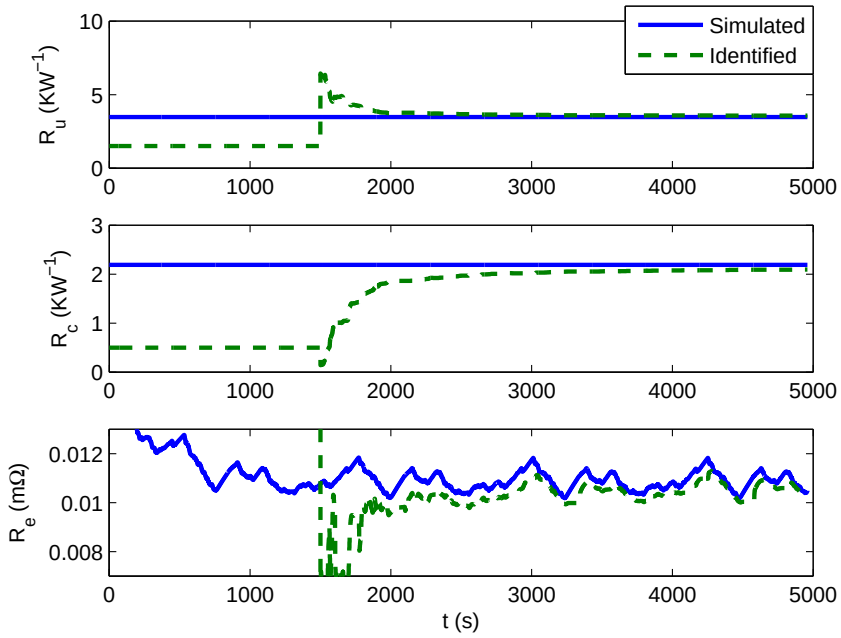

Figure 2.14: Identification of Temperature Dependent Internal Resistance by the Least Square Algorithm with Non-uniform Forgetting Factors.

from Figure 2.16 that the simulated internal resistance gradually increases over time while still subject to short-term variation due to the fluctuation of the battery core temperature. The identified R_e follows both the long-term and short-term variation of the simulated one with a small delay as shown in the inset of Figure 2.16. In real vehicle application, since R_e is varying all the time, it is difficult to evaluate SOH by the instantaneous value of R_e, and the time-averaged R_e might be a better choice. The mean value of R_e for each UAC cycle is plotted in the lower half of Figure 2.16, showing good match with the simulated value.

Adaptive monitoring of the temperature is also shown in Figure 2.17. It is noted that as the internal resistance grows, the temperature will also be elevated due to the increase of the heat generated. Since the observer is updated with the identified R_e in real time, it estimates both the core and the surface temperatures with high accuracy.

2.6 Conclusion

The core temperature of a lithium ion battery, which is usually not measurable, is of great importance to the onboard battery management system, especially when

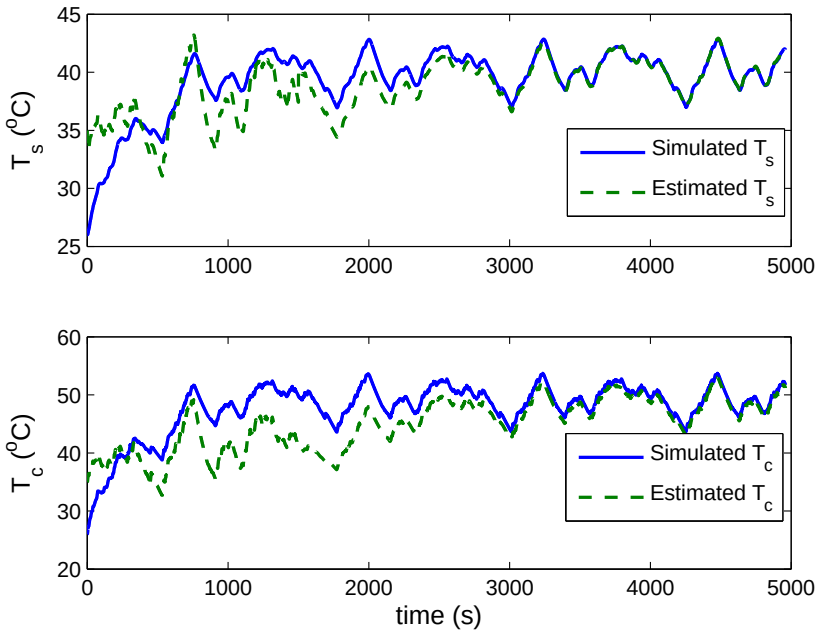

Figure 2.15: Adaptive Estimation of Battery with Temperature Dependent Internal Resistance by Forgetting Factors. (top: estimation of surface temperature T_s; bottom: estimation of core temperature T_c)

the batteries are subject to drive cycles with high C-rate. The core temperature can be estimated by a two states thermal model, and the model parameters are critical for the accuracy of the estimation. In this chapter, an online parameter identification scheme based on the least square algorithm is designed for a cylindrical lithium ion battery thermal model. The online identification scheme can automatically identify model parameters based on the commonly available onboard signals. The updated parameters are then used to predict the unmeasured core temperature using a model based observer as shown with an A123 26650 lithium iron phosphate battery.

When the internal resistance of the battery is temperature dependent, which is a more realistic situation, the least square algorithm is augmented with non-uniform forgetting factors. The algorithm with forgetting factors can not only track the time-varying internal resistance, but also guarantee unbiased identification of the remaining constant parameters. The online parameterization also shows the capability to track the long-term variation of the internal resistance due to aging or degradation/abuse. The growth in internal resistance can be used for the SOH monitoring of the batteries.

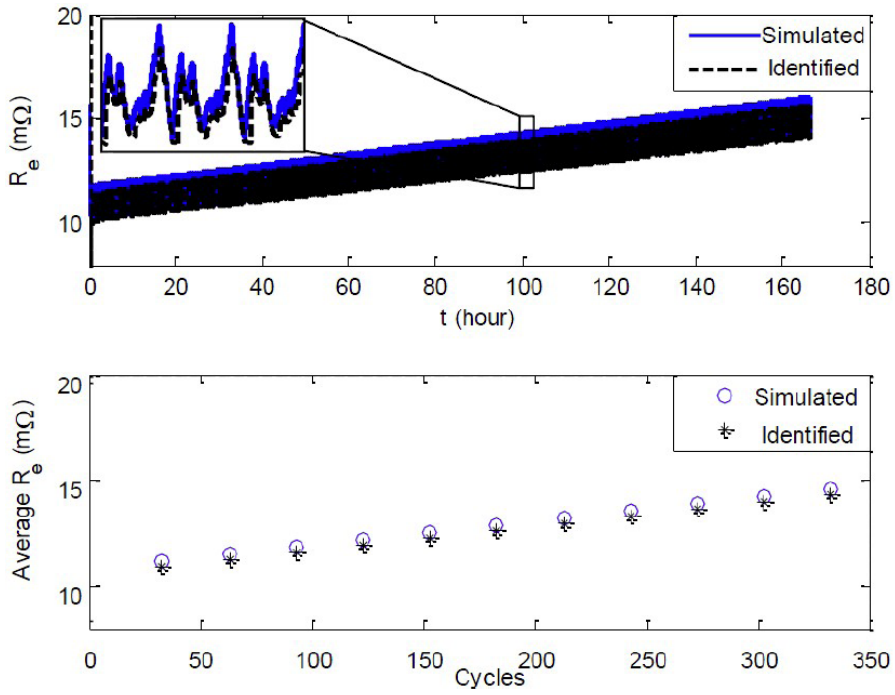

Figure 2.16: (Simulated) Identification of internal resistance subject to degradation. (top: identification of R_e with both short-term and long-term variation; bottom: simulated and identified cycle-average R_e).

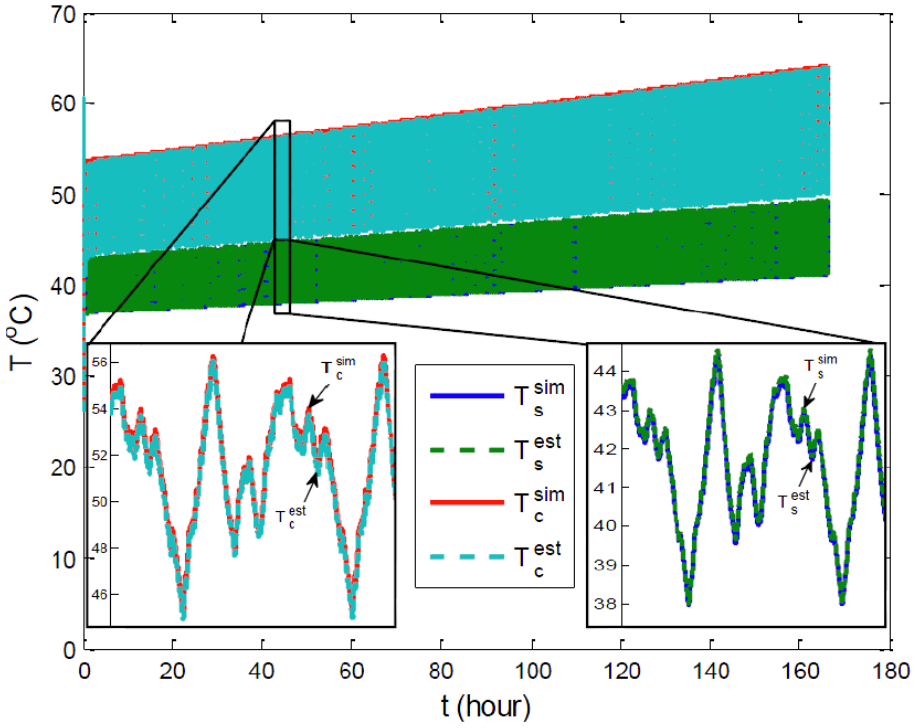

Figure 2.17: Adaptive estimation of battery temperatures subject to degradation.

CHAPTER III

Temperature Estimation of Scalable Battery Strings

3.1 Introduction

In vehicle applications, batteries are usually packed in modules to satisfy the energy and power demand. In this chapter, temperature monitoring for battery packs is investigated.

Based on the single cell model, a thermal model for one-dimensional battery strings is developed by taking into account the thermal interaction between cells. The 1-D string is modeled along the path of the coolant flow. Considered thermal interaction includes thermal conduction between adjacent cells and convective cooling between cells and the coolant flow. A 2-D pack model can be constructed by incorporating thermal interaction between multiple rows of 1-D strings.

A model-based observer is then designed to estimate the core and surface temperatures of all the cells in the string. A closed loop observer with measurement of the surface temperature of some cells can be used to mitigate the impact of model uncertainty and accelerate observer convergence from initial estimation errors. Ideally, the number of temperature sensors needs to be as small as possible. For this purpose, sensor deployment strategy is then studied to determine the minimum number of sensors that will give full observability and their optimal locations in battery strings.

It is later found that the number of implemented sensors in a commercial battery pack is much less than the number needed for full observability. To accommodate such issue, the optimal observer design and sensor deployment problem is studied under the unobservable conditions. The goal is to minimize the worst-case estimation error subject to bounded model uncertainty. Two observer design approaches are investigated, namely the robust H_∞ observer and the optimal DC observer which aims

at minimizing the worst-case DC gain of the error transfer function. The methodology is then applied to a battery string with 10 cells and 1 available temperature sensor, and the performance of the two observers is compared in various ways.

3.2 A Scalable Thermal Model for 1-D Battery Strings

The single-cell cylindrical battery thermal model in (2.1) can be scaled up to a battery string model by considering cell to cell heat conduction [79], and heat balance of the flowing coolant [37, 42], as shown in Figure 3.1.

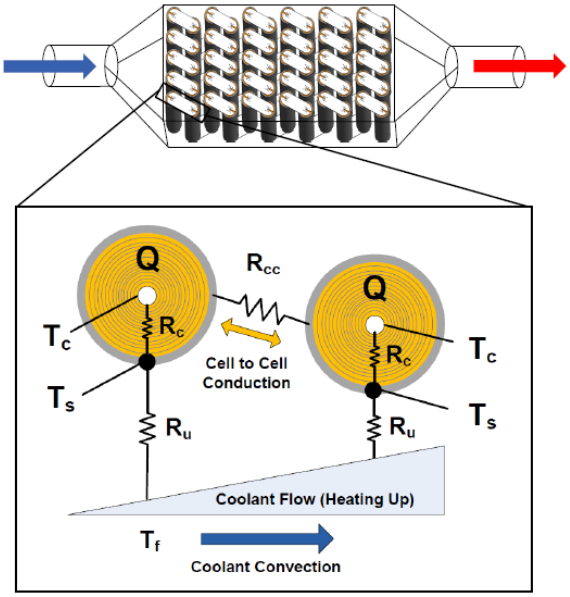

Figure 3.1: A possible battery pack configuration, with 5 strings of 12 cells along the coolant path.

As shown in Figure 3.1, the string can be considered as cells connected in series with tabs and arranged in a row configuration along the coolant flow path. The coolant flows through the space between cells from the inlet to the outlet, and absorbs the heat dissipated from the cell surface through convection.

The temperature evolution of the ith cell in the string can be modeled as

$$
\begin{aligned}
C_c \frac{dT_{c,i}}{dt} &= I^2 R_{e,i} + \frac{T_{s,i} - T_{c,i}}{R_c}, \\
C_s \frac{dT_{s,i}}{dt} &= \frac{T_{f,i} - T_{s,i}}{R_u} - \frac{T_{s,i} - T_{c,i}}{R_c} + Q_{cc,i}, \\
Q_{cc,i} &= \begin{cases} (T_{s,2} - T_{s,1})/R_{cc}, & i = 1 \\ (T_{s,i-1} + T_{s,i+1} - 2T_{s,i})/R_{cc}, & i = 2, \cdots, n-1 \\ (T_{s,n-1} - T_{s,n})/R_{cc}, & i = n \end{cases} \\
T_{f,i} &= \begin{cases} T_{f,in}, & i = 1 \\ T_{f,i-1} + \frac{T_{s,i-1} - T_{f,i-1}}{R_u C_f}, & i = 2, \cdots, n \end{cases}
\end{aligned}
\tag{3.1}
$$

where k is the index of the cell along the coolant flow direction, and n is the number of cells. In (3.1), heat conduction between adjacent cells is modeled as heat flow over a conduction resistance R_{cc}, driven by temperature difference between surfaces of the adjacent cells. It is noted here that R_{cc} is a lumped parameter, which includes the heat conduction resistance of the tab and other possible thermal connections between cells, such as spacers and air gap. Coolant temperature entering the ith cell, $T_{f,i}$, is determined based on heat balance of the flow around the previous cell. Its value is obtained by dividing the heat removed from the $i-1$th cell, $\frac{T_{s,k-1} - T_{f,k-1}}{R_u}$, by the heat capacity of the flow, C_f, plus $T_{f,i-1}$. The convection resistance R_u and the heat capacity of the flow are dependent on coolant flow rate. For simplicity, current I is considered the same for all cells as if the string is connected in series.

Simulated temperature profile for a string with 5 cells under the Urban Assault Cycle [89] is shown in Figure 3.2. Cell 1 is at the coolant inlet and cell 5 at the outlet. The inlet air temperature is fixed at 25 ^oC and the flow rate is 9.5×10^{-3} $m^3 s^{-1}$, corresponding to a flow velocity of 1.515 ms^{-1}. In Figure 3.2, as the coolant air flows from cell 1 to cell 5, its temperature T_f increases as it absorbs heat from cells sequentially. Consequently, the surface and the core temperatures of the cells also increase down the string due to the coolant temperature rise. Here, it is assumed that all the cells have the same value for R_u. As can be seen in Figure 3.2, the hottest cell is the last one since it is subject to the highest ambient temperature. For some pack geometries, flow condition might be different for cells. For example, cells at the two ends of the string may have higher heat rejection capacity due to larger space around them. Therefore, cells in the middle of the string will be hotter. For these cases, different R_u numbers need to be applied to different cells.

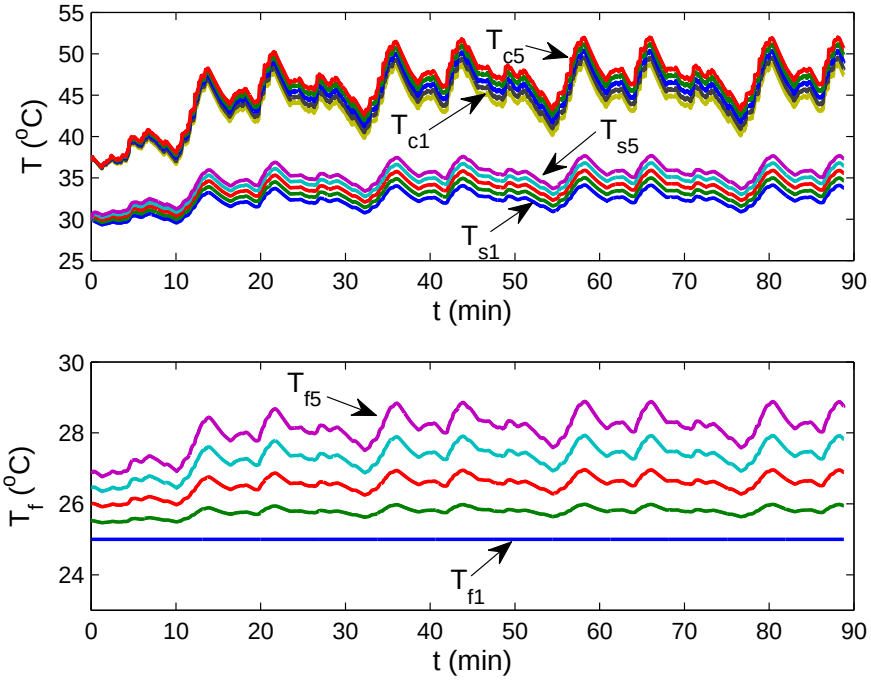

Figure 3.2: Simulated temperature profile of a 5-cell battery string under the UAC cycle. (for T_c, T_s and T_f, from cooler to hotter: cell 1, cell 2, cell 3, cell 4 and cell 5)

3.3 Model-based Estimation of the Battery String Temperatures

The string thermal model developed in Section 3.2 can be used for pack-level temperature estimation. A model-based observer can be categorized as either an open-loop observer or a closed-loop observer. Specific issues associated with open-loop and open closed-loop estimation are discussed in this section.

3.3.1 Open-Loop Estimation

An open-loop observer estimates the states solely based on the model and the measured inputs. The open-loop observer will give accurate temperature estimation if the model is perfectly known and the initial temperatures of all the batteries are known.

When the initial temperatures are unknown, the temperature estimation will still converge to the actual temperature since the thermal system is stable, but the con-

vergence will take a long time due to the slow thermal dynamics of the battery. In fact, it is quite common to have unknown initial temperature in real operation. Since only the battery surface temperature is measured in onboard BMS, the accurate core temperature is unknown at startup. If the vehicle is started from steady states, e.g. after overnight rest, the core temperature can be assumed to be the same as the surface temperature. But such an assumption may not be valid for short shutdown.

Figure 3.3 shows the simulated temperature evolution during shutdown of a battery pack with 5 cells in series. Temperature profile under the precedent drive cycle is shown in Figure 3.2. The current is cut off at the beginning of the simulation in Figure 3.3, and the cooling system is kept on during the shutdown process. It is seen in Figure 3.3 that it takes the battery pack more than 40 minutes to cool down to the ambient temperature. In real application, it may not be feasible to keep the cooling system on for 40 minutes after key-off. Consequently, the actual time for the pack to cool down will be longer. If the driver turns the vehicle back on before the pack gets to the thermal equilibrium, the initial reading of the surface temperature at startup will not be a good approximation for the initial core temperatures. The shorter the shutdown is, the larger the errors of such approximation will be. For example, if the next startup occurs at about 10 minutes after the previous shutdown, according to Figure 3.3, the difference between the surface and the core temperatures will be roughly 7 ^oC.

A simulation has been conducted to show how fast the open loop estimation of the temperatures will converge under unknown initial core temperatures. In simulation, the actual initial surface and core temperatures of all the cells are set to be 30 ^oC and 37 ^oC respectively. In the open-loop observer, the initial guess of the core temperature is taken to be the same as the known surface temperature. Estimation results are shown in Figure 3.4. For clarity in the figure, only the temperatures of cell 1 and cell 5 are plotted. It can be observed in Figure 3.4 that the convergence of the open loop estimation, $T_{s,i}^{ol}$ and $T_{c,i}^{ol}$, takes more than 30 minutes. Such a big delay is due to the slow thermal dynamics of the batteries and may lead to ineffective battery management during the startup period. Furthermore, in onboard BMS, it is not feasible to measure the surface temperature of every cell. As a result, in addition to the unknown initial core temperature considered here, uncertainty in initial surface temperatures of those unmeasured cells will further delay the convergence.

In addition, the accuracy of open-loop estimation will also be affected by model uncertainty, such as imprecise model parameters. Under current strategy, by using the method developed in Section II, thermal parameters are identified for cells with

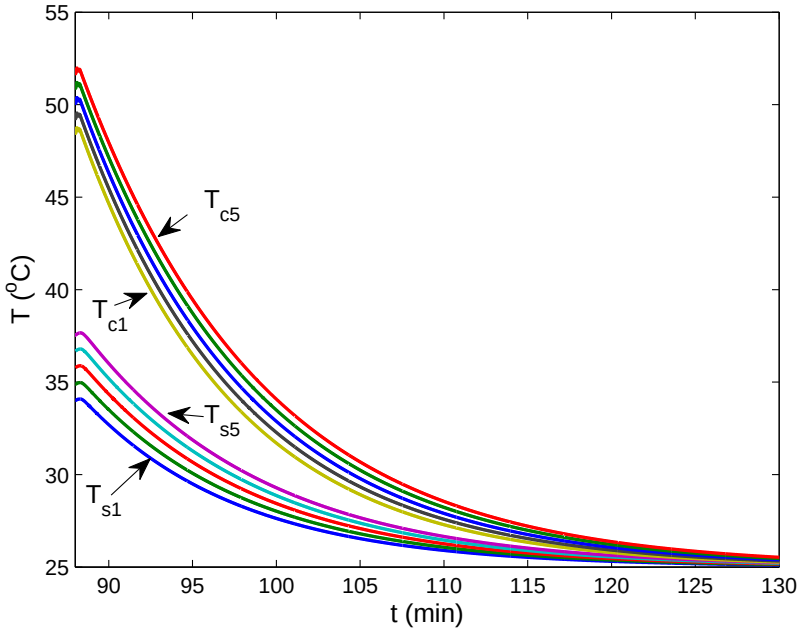

Figure 3.3: Simulated battery pack temperature profile during shutdown. (for T_c, T_s and T_f, from bottom to top: Cell1, Cell2, Cell3, Cell4, Cell5)

thermocouples installed on the surface. As for the cells without thermocouple, their model parameters are assumed to be the same as the identified ones, which might lead to model mismatch. For example, it is known that the battery internal resistance R_e often varies from cell to cell, caused by factors such as degradation and manufacturing variability [92, 93]. Simulation has been conducted to show the errors induced by nonidentical cell internal resistance in temperature estimation. In simulation, it is assumed that the surface temperatures of cell 1 and 5 are measured and thus their internal resistance is known to the observer with a value of $R_{e,0}$. The other cells, cell 2 to 4, whose surface temperatures are not accessible, are assigned with an internal resistance of 20% higher. The observer will have correct internal resistance values for cell 1 and 5 but inaccurate values for cell 2 to 4. In Figure 3.5, temperature estimation of cell 1 and 4 is plotted and compared with the simulated actual temperatures. Errors are observed in the open loop estimation (T_{si}^{ol}, T_{ci}^{ol}), especially for cell 4, whose internal resistance is not accurate in the observer. Similar errors exist in the temperature estimations of cell 2 and 3, which are not plotted. For the first cell, although the model parameters in the observer are correct, the temperature estimation is still erroneous as the errors propagate from the biased estimation of other cells through cell to cell conduction.

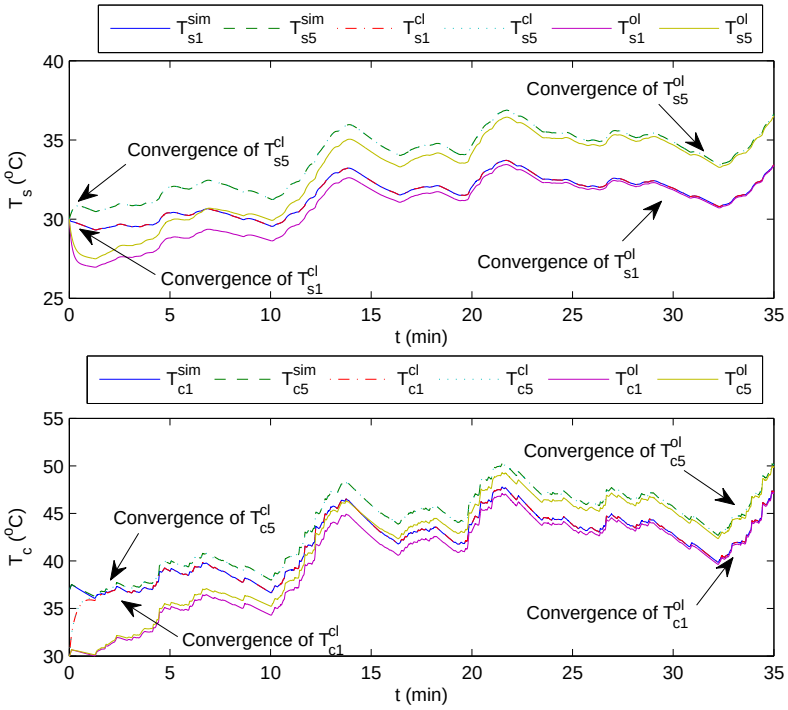

Figure 3.4: Convergence of the open loop and the closed loop observers.

3.3.2 Closed-Loop Estimation

In order to reduce the estimation error induced by model uncertainty and the delay in temperature estimation due to the unknown initial conditions, a closed-loop observer can be applied.

The thermal model of a battery string in Eq. (3.1) can be written in the general state space representation as

$$\begin{aligned} \dot{x} &= Ax + Bu, \quad x \in \mathbb{R}^{2n}, \\ y &= Cx + Du, \quad y \in \mathbb{R}^{m} \end{aligned} \tag{3.2}$$

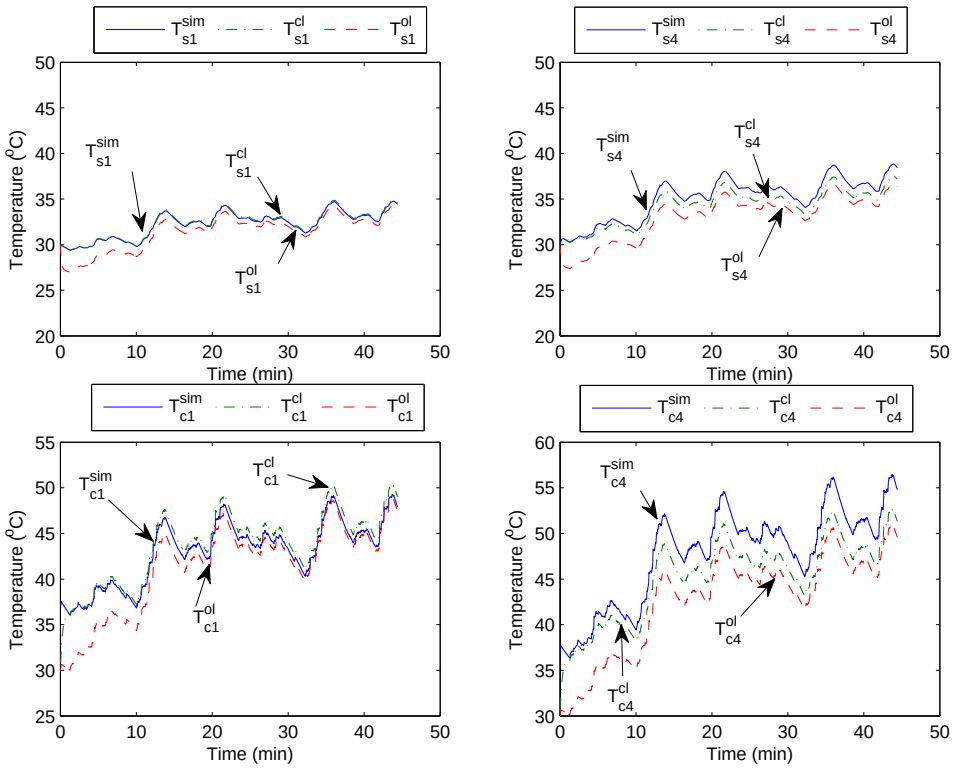

Figure 3.5: Convergence of the temperature estimation by the open loop and the closed loop observer. (Top left: T_{s1}; top right: T_{s4}; bottom left: T_{c1}; bottom right: T_{c4})

where n is the number of cells and m is the number of sensors, and

$$
\begin{aligned}
x &= \begin{bmatrix} T_{c,1} & T_{s,1} & T_{c,1} & T_{s,1} & \cdots & T_{c,n} & T_{s,n} \end{bmatrix}^T, \\
B &= \begin{bmatrix} \frac{R_{e,1}}{C_c} & 0 & \frac{R_{e,2}}{C_c} & 0 & \cdots & \frac{R_{e,n}}{C_c} & 0 \\ 0 & \frac{1}{R_u C_s} & 0 & \frac{1}{R_c C_s}\frac{R_u C_f - 1}{R_u C_f} & \cdots & 0 & \frac{1}{R_c C_s}\left(\frac{R_u C_f - 1}{R_u C_f}\right)^{n-1} \end{bmatrix}^T \\
D &= 0 \\
u &= \begin{bmatrix} I^2 & T_{f,in} \end{bmatrix}^T.
\end{aligned}
\tag{3.3}
$$

The matrix A is the state matrix that captures the heat transfer between the temperature states shown in Eq.(3.8), and y is the temperature state(s) measured by the sensor(s) whose location is specified in the C matrix. For example, if a thermocouple

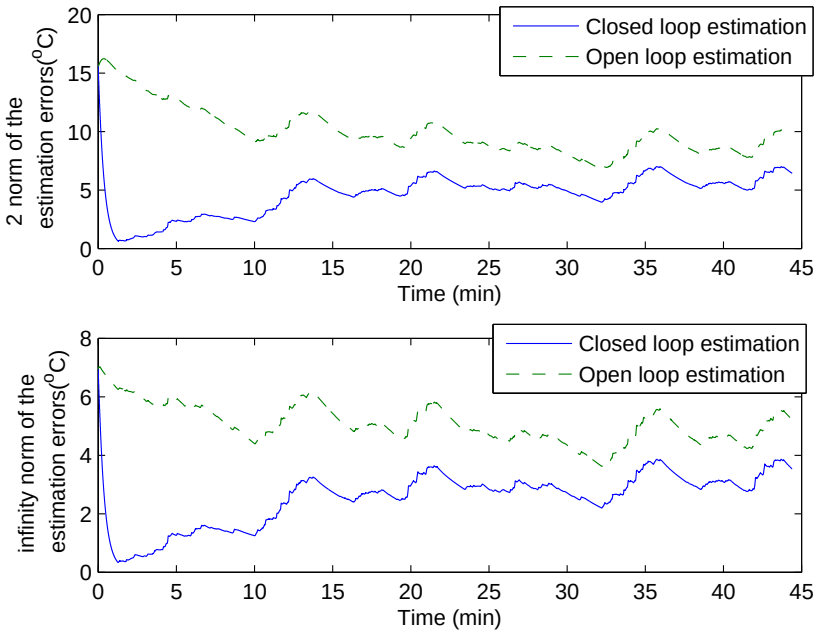

Figure 3.6: Norms of the estimation errors for the open loop and the closed loop observer.

is used to measure the surface temperature of the ith cell, we will have

$$C = \begin{bmatrix} 0 & \cdots & 0 & \underbrace{1}_{2i-1\text{th entry}} & \cdots & 0 \end{bmatrix}. \tag{3.4}$$

In a closed-loop observer, the difference between the measurement and the estimated output is fed back to correct the estimation through an observer gain L [47],

$$\begin{aligned} \dot{\hat{x}} &= A\hat{x} + Bu + L(y - \hat{y}) \\ \hat{y} &= C\hat{x}. \end{aligned} \tag{3.5}$$

When the model is completely observable, by tuning the observer gains, the dynamics of the closed-loop observer can be accelerated. Consequently, the temperature estimation will converge to the actual temperatures much more quickly than the open-loop estimation, when starting with unknown initial temperatures. Simulated performance of a closed-loop temperature observer is shown in Figure 3.4 to compare with that of the open-loop observer. It can be seen that the closed-loop estimation, $T_{s,i}^{cl}$ and $T_{c,i}^{cl}$, converge to the actual temperatures much faster than the open-loop

estimation, $T_{s,i}^{ol}$ and $T_{c,i}^{ol}$. Both temperatures estimated by the closed-loop observer converge within 5 minutes, as compared to the 30 minutes taken by the open-loop observer. The closed-loop observer can also greatly reduce the estimation error under model mismatch as shown in Figure 3.5, which demonstrates previously the estimation error of the open-loop estimation under resistance uncertainty. The 2 and infinity norms of the temperature estimation errors for all 5 cells by both the open-loop and closed-loop observers are also plotted in Figure 3.6, showing that the overall errors in temperature estimation are smaller under the closed-loop estimation.

3.4 Sensor Deployment Strategy based on Observability Analysis

An effective closed-loop observer needs measurement of the temperatures states to satisfy the observability condition. In this section, the observability conditions are analyzed to determine the minimum number of sensors needed for battery strings with various lengths and guide the sensor placement.

The observability of the thermal model can be examined by its observability matrix [47]

$$O = \begin{bmatrix} C \\ CA \\ \cdots \\ CA^{2n-1} \end{bmatrix}. \tag{3.6}$$

The model is completely observable if and only if the rank of O is equal to n.

First, a battery string with 2 cells is investigated, whose A matrix is

$$A = \begin{bmatrix} -\frac{1}{R_c C_c} & \frac{1}{R_c C_c} & 0 & 0 \\ \frac{1}{R_c C_s} & -(\frac{1}{R_c C_s} + \frac{1}{R_u C_s} + \frac{1}{R_{cc} C_s}) & 0 & \frac{1}{R_{cc} C_s} \\ 0 & 0 & -\frac{1}{R_c C_c} & \frac{1}{R_c C_c} \\ 0 & (\frac{1}{{R_u}^2 C_f C_s} + \frac{1}{R_{cc} C_s}) & \frac{1}{R_c C_s} & -(\frac{1}{R_u C_s} + \frac{1}{R_c C_s} + \frac{1}{R_{cc} C_s}) \end{bmatrix}. \tag{3.7}$$

In (3.7), the $\frac{1}{R_{cc} C_s}$ terms in the 2nd and the 4th rows of the A matrix account for the thermal conduction between the 2 cells. The $\frac{1}{{R_u}^2 C_f C_s}$ term in the 4th row represents the impact of cell 1 on cell 2 through coolant flow convection. The absence of this term in the 2nd row indicates that such impact is unidirectional, or, cell 2 cannot influence cell 1 via coolant convection. The C matrix is determined by sensor location. If the

No. of cells	Min. No. of sensors
1,2,3	1
4,5,6	2
7,8,9	3
10,11,12	4

Table 3.1: Minimum number of sensors rendering observability for battery strings with various lengths.

surface temperature of cell 1 is measured, then $C_1 = \begin{bmatrix} 0 & 1 & 0 & 0 \end{bmatrix}$, and if the surface temperature of cell 2 is measured, $C_2 = \begin{bmatrix} 0 & 0 & 0 & 1 \end{bmatrix}$. It can be checked numerically that the rank of U is 4 when either C_1 or C_2 is applied. This means that for a cell string with 2 cells, either measuring the surface temperature of cell 1 or cell 2 renders observability.

More generally, for a cell string with n cells, the A matrix is specified in (3.8). Like the case of a 2-cell string, the $\frac{1}{R_{cc}C_s}$ terms in the even rows represent the heat conduction between adjacent cells. Starting form the 4th row, the effect of coolant convection is reflected in the terms related to $\frac{1}{{R_u}^2 C_f C_s}$ in the even rows. It is found that all the upstream cells in the string will affect the downstream cells through coolant flow convection, and such effect becomes weaker as the cells are further apart. Consider the last row of the A matrix as an example for illustration. From the 2nd column to the third last column, the terms $\frac{1}{R_u^2 C_f C_s}(1-\frac{1}{R_u C_f})^{n-i-1}, \quad i = 1, 2, \cdots, n-1$, represent the impact of cell i on cell n through coolant convection. It can be seen that such impact is attenuated by a factor of $(1 - \frac{1}{R_u C_f})$ if the two cells are further apart by one cell interval. This feature of the coolant convection is different from that of the cell to cell conduction, which only exists between adjacent cells and the strength is always the same.

The observability analysis has been conducted to find the minimum number of sensors required for full observability for battery strings with different number of cells. The results are summarized in Table 3.1. It is noted that for cell strings with more than 5 cells, sensor location will also affect the observability. For example, for a string with 5 cells, although the minimum required number of sensors is 2, it does not mean that the model will be fully observable under any sensor locations. As shown in Figure 3.7, if the 2 sensors are placed at the first 2 cells, the rank of the observability matrix is less than 10 which is required for observability. But when the 2 sensors are placed at cell 1 and cell 5, the observability matrix will be of full rank. This can be explained by the definition of observability. Observability indicates the possibility of

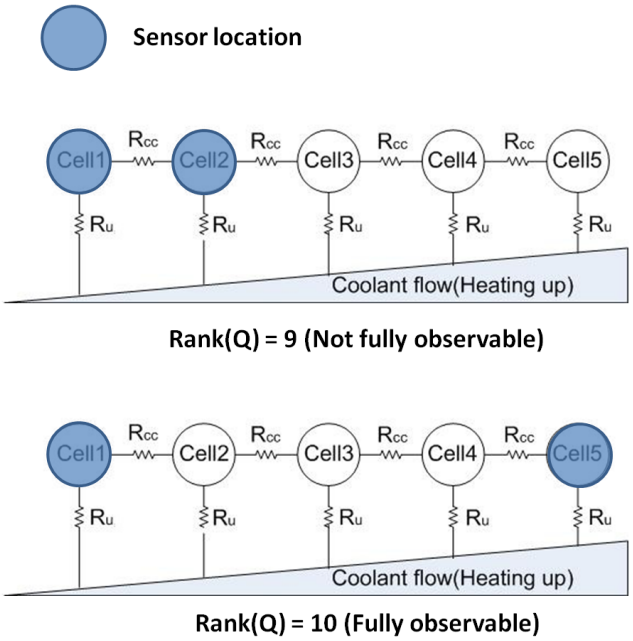

Figure 3.7: Sensor locations and observability.

determining all the states based on the model and the available measurements. The model defines the relation between different states. In order to achieve observability, the measurements should provide enough constraints to determine the states uniquely based on the model. When the sensors are placed at the first 2 cells, the constraints provided by the sensors are redundant at the beginning section of the string. While no measurement is implemented in the latter section of the string, the cell temperatures in that section cannot be constrained to unique values. Consequently, the condition of full observability is not satisfied. When the sensors are deployed at the first and the last cells, constraints are imposed evenly on the string, and all the states can be determined by the measurements and the model.

In some battery pack configuration, the thermal interaction between cells is weaker, e.g. either cell-to-cell heat conduction or forced coolant convection is missing or negligible. For example, cell-to-cell conduction can be very small in some pack designs due to the shape or the material of the tab and the spacer. When the coolant flow is not circulated through the pack, e.g. during cooling system breakdown, the cells are only cooled via natural convection and thus the upstream cells will not affect the downstream cells through convection. Under these circumstances, the observability conditions will be different. Take a cell string with 5 cells as an example. As shown in Figure 3.8, when the cells are cooled by natural convection, placing the sensors at

Conditions	No. of combinations giving full observability
Full interaction	106/495
Natural convection	52/495
No cell to cell conduction	1

Table 3.2: Number of sensor position combinations giving full observability for a string with 12 cells and 4 sensors.

the first and the last cell will still satisfy observability condition. But when the cell to cell conduction is missing, the same sensor locations cannot render observability. Such analysis can be generalized to strings with more cells. A string with 12 cells

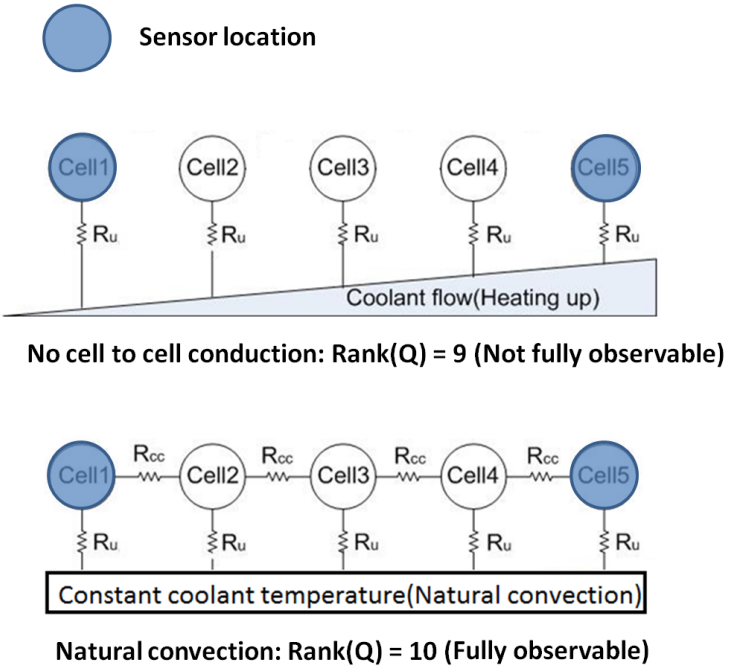

Figure 3.8: Observability of the same sensor locations under different conditions.

is analyzed and the results are summarized in Table 3.2. The minimum number of sensors that gives full observability is 4. As shown in Table 3.2, among all 495 combinations of 4 sensor locations, if there are both circulated coolant convection and cell to cell conduction (referred to as full interaction in Table 3.2), 106 combinations will give full observability. Under natural convection, only 52 combinations can satisfy full observability condition. When the cell to cell conduction is missing, only 1 combination yields full observability, where the sensors are evenly distributed at the cell 3, 6, 9 and 12.

Of the two types of modeled thermal interaction between cells, namely the cell to cell heat conduction and the forced convection, the former tends to have larger impact on the observability. This may be related to the fact that the cell-to-cell heat conduction is a two-way interaction, whereas the forced convection is single directional. Consequently, stronger cell-to-cell heat conduction is favored for model observability, which could also reduce the temperature difference between cells and help contain the temperature non-uniformity in the pack. However, on the negative side, in case of a single cell thermal failure, e.g. local overheating, the strong cell-to-cell heat conduction will facilitate the spread of the failure to other cells, which is not desirable from a safety perspective.

$$A = \begin{bmatrix}
\frac{-1}{R_cC_c} & \frac{1}{R_cC_c} & 0 & 0 & 0 & 0 & \cdots & 0 & 0 & 0 \\
\frac{1}{R_cC_s} & \frac{-1}{C_s}(\frac{1}{R_u}+\frac{1}{R_c}+\frac{1}{R_{cc}}) & 0 & \frac{1}{R_{cc}C_s} & 0 & 0 & \cdots & 0 & 0 & 0 \\
0 & 0 & \frac{-1}{R_cC_c} & \frac{1}{R_cC_c} & 0 & 0 & \cdots & 0 & 0 & 0 \\
0 & \frac{1}{C_s}(\frac{1}{{R_u}^2C_f}+\frac{1}{R_{cc}}) & \frac{1}{R_cC_s} & \frac{-1}{C_s}(\frac{1}{R_u}+\frac{1}{R_c}+\frac{2}{R_{cc}}) & 0 & \frac{1}{R_{cc}C_s} & \cdots & 0 & 0 & 0 \\
 & & & & & \ddots & & & & \\
0 & 0 & 0 & 0 & 0 & 0 & \cdots & 0 & -\frac{1}{R_cC_c} & \frac{1}{R_cC_c} \\
0 & \frac{1}{R_u^2C_fC_s}(1-\frac{1}{R_uC_f})^{n-2} & 0 & \frac{1}{R_u^2C_fC_s}(1-\frac{1}{R_uC_f})^{n-3} & 0 & 0 & \cdots & \frac{1}{{R_u}^2C_fC_s}+\frac{1}{R_{cc}C_s} & \frac{1}{R_cC_s} & \frac{-1}{C_s}(\frac{1}{R_u}+\frac{1}{R_c}+\frac{1}{R_{cc}})
\end{bmatrix} \tag{3.8}$$

3.5 Observer Design and Sensor Deployment Strategy under Frugal Sensor Allocation

The number of temperature sensors needed for full observability has been derived in the previous section. However, in current industry practice, sensors installed in a battery pack is far less than the number required for observability, e.g. only one for every 10 cells. As a result, the temperature states will not be completely observable. For example, it is found that for a string with 10 cells, at least 4 sensors are needed to give full observability. However, the available sensors in a commercial battery pack is much less than the derived number, e.g. 16 for 288 cells in Chevy Volt [94] and 42 for 288 cells in Toyota plug-in Prius [95]. It may not be realistic to increase the number of sensors considering the cost and diagnostic requirement. Therefore, an interesting research problem is to find the best performance that can be achieved with the frugal sensor assignment which leaves the temperature states not completely observable.

In this section, the observer design and sensor deployment problems for temperature estimation in battery strings are studied under unobservable conditions. The goal is to design an observer with optimal performance under bounded model uncertainty. Without loss of generality, a battery string with 10 cells and 1 temperature sensor will be considered as a design example.

3.5.1 Problem Formulation for Temperature Estimation under Model Uncertainty

The battery string model has been presented in Eq.(3.2) and (3.3). The objective here is to design a model-based observer that could achieve optimal performance in temperature estimation under bounded model uncertainty. As has been mentioned, the battery internal resistance typically varies from cell to cell due to factors such as degradation, manufacturing variability, and operating conditions [92, 93]. The observer can only use the nominal value $R_{e,0}$ for all the cells, which is either provided by the manufacturer or identified for the cell installed with thermocouple by using the method discussed in Chapter II. Consequently, there will be a mismatch in battery resistance,

$$\begin{aligned} \Delta R_e &= \begin{bmatrix} \Delta R_{e,1} & 0 & \Delta R_{e,2} & 0 & \cdots & \Delta R_{e,n} & 0 \end{bmatrix}^T \\ &= \begin{bmatrix} R_{e,1} - R_{e,0} & 0 & R_{e,2} - R_{e,0} & 0 & \cdots & R_{e,n} - R_{e,0} & 0 \end{bmatrix}^T, \end{aligned} \tag{3.9}$$

which is the considered model uncertainty. The resistance uncertainty are usually within certain bounds. It is assumed here that each $\Delta R_{e,i}$ is bounded within $\pm 10\%$ of the nominal resistance,

$$-0.1R_{e,0} \leq \Delta R_{e,i} \leq 0.1R_{e,0}, \quad \forall i = 1, 2, \cdots, n. \tag{3.10}$$

and it could take any values within the bounds. Other bound values can be considered without changing the methodology to be introduced. Sensor uncertainty, such as measurement noise, can also be included. The observer will be designed to minimize the worst-case estimation error under the bounded uncertainty. Ideally, optimal observer performance should be considered under current dynamic input, which can be treated as disturbance.

Optimal observer design is usually addressed by minimizing a cost function of the estimation error. There are various ways of characterizing estimation error in the cost function, which lead to different observer design approaches. For example, in Kalman filter, when the process and measurement noises are Gaussian, the cost function is the variance of the state estimation error [48, 96]. When designing an H_∞ $(L_2 - L_2)$ observer, the L_2 norm of the estimation error is minimized over all disturbance input with bounded L_2 norm [97, 98]. Similarly, the $L_2 - L_\infty$ observer minimizes the L_∞ norm of the estimation error over all L_2-bounded disturbance input [99, 100]. The optimal observers will achieve best performance with respect to their own definition of performance. In the following two subsections, two optimal observers will be discussed and their overall performance are compared.

3.5.2 Robust H_∞ Observer Design

When designing an H_∞ observer for a general linear system in Eq.(3.2), the input u is considered as a disturbance with bounded L_2 norm, and an optimal observer (filter) $\mathscr{F}$ is sought to minimize the L_2 norm of the estimation error e under all L_2-bounded disturbance input [99],

$$\min_{\mathscr{F}} \sup_{u(t) \in L_2} \frac{\|e(t)\|_{L_2}}{\|u(t)\|_{L_2}}. \tag{3.11}$$

The estimation error is defined as the difference between the true value and the estimate of variable z,

$$e = z - \hat{z}, \tag{3.12}$$

where z can be defined as any linear combination of state x,

$$z = Wx. \tag{3.13}$$

Since the L_2 norm is usually used to measure the energy contained in a signal, the H_∞ observer is also referred to as the energy-to-energy observer [100]. When e is a scalar, the L_2 norm is defined as

$$\|e(t)\|_{L_2} = (\int_0^\infty |e(t)|^2 dt)^{\frac{1}{2}}. \tag{3.14}$$

When e_x is a vector, strictly speaking, the L_2 norm needs to be the $L_{2,r}$ norm [101],

$$\|e(t)\|_{L_2} = (\int_0^\infty \|e(t)\|_r^2 dt)^{\frac{1}{2}}, \tag{3.15}$$

where the r-norm of e needs to be taken first before calculating the L_2 norm. In the H_∞ observer design, r is usually taken as 2, which means that the 2-norm of e will be minimized. Sometimes, however, it might be more desirable to minimize the maximum (or infinity) norm of e, which indicates the maximum estimation error among all the states. This issue will be re-visited later in this chapter. In the frequency domain, the H_∞ observer is interpreted as minimizing the H_∞ norm of the transfer function from the disturbance input to the estimation error, G_{eu}, which is denoted as $\|G_{eu}\|_{H_\infty}$. For single-input-single-output systems, the H_∞ norm is the peak value of the magnitude of the transfer function over all frequencies, and for multiple-input-multiple-output systems, the H_∞ norm is the supreme of the (induced) 2-norm of the transfer function vector (matrix) over all frequencies. So the observer will look at

$$\min_{\mathscr{F}} \sup_{\omega \in [0,+\infty)} \|G_{eu}(j\omega)\|_2. \tag{3.16}$$

The H_∞ observer takes the form,

$$\begin{aligned} \mathscr{F}: \quad \dot{\hat{x}} &= A_h \hat{x} + B_h y \\ \dot{\hat{z}} &= C_h \hat{x} + D_h y. \end{aligned} \tag{3.17}$$

According to **Theorem 3.1** in [102], a γ-suboptimal H_∞ observer $\mathscr{F}$ that could achieve $0 < \|G_{zu}\|_{H\infty} < \gamma$ is admissible if and only if there exist positive definite matrices $R > 0$, $X > 0$, and matrices M, N, Z and D_h, such that the following two

linear matrix inequalities (LMI) are satisfied,

$$\begin{bmatrix} RA+A^TR & RA+A^TX+C^TZ^T+M^T & RB & W^T-C^TD_h^T-N^T \\ * & A^TX+XA+C^TZ^T+ZC & XB+ZD & W^T-C^TD_h^T \\ * & * & -\mathbf{I} & -D^TD_h^T \\ * & * & * & -\gamma^2\mathbf{I} \end{bmatrix} < 0,$$
$$R - X < 0, \tag{3.18}$$

where $\mathbf{I}$ is the identity matrix and $*$ denotes the symmetric entry. The coefficients of the H_∞ observer can be obtained as

$$\begin{aligned} A_h &= (R-X)^{-1}M, \quad & B_h &= (R-X)^{-1}Z, \\ C_h &= N, & D_h &= D_h. \end{aligned} \tag{3.19}$$

The optimal H_∞ observer design problem can then be formulated as a convex minimization problem,

$$\begin{aligned} &\min_{R,X,M,N,D_h,\gamma^2} \gamma^2 \\ &\text{subject to Eq.(3.18)}, \end{aligned} \tag{3.20}$$

which could be addressed by using LMI solvers such as Matlab LMI toolbox, SeDuMi [103] and YALMIP [104].

In the presence of parameter uncertainty, a robust H_∞ observer needs to be designed, which minimizes the worst-case $\|G_{eu}\|_{H\infty}$ under all possible uncertainty. Specifically, if the system matrices

$$\mathbf{T} = \begin{bmatrix} A & B \\ C & D \end{bmatrix} \tag{3.21}$$

are uncertain but belong to a convex polytope consisting of $T_1, T_2, \cdots, T_q$, that is,

$$\mathbf{T} = \sum_j^q \alpha_j \mathbf{T}_j, \quad \alpha_j \geq 0, \quad \sum_j^q \alpha_j = 1, \tag{3.22}$$

the robust optimal H_∞ observer can be obtained by solving the previous minimization

problem over all the vertices of the polytope,

$$\min_{R,X,M,N,D_h,\gamma^2} \gamma^2$$

s.t.

$$\begin{bmatrix} RA_j + A_j^T R & RA_j + A_j^T X + C_j^T Z^T + M^T & RB_j & W^T - C_j^T D_h^T - N^T \\ * & A_j^T X + XA_j + C_j^T Z^T + ZC_j & XB_j + ZD_j & W^T - C_j^T D_h^T \\ * & * & -\mathbf{I} & -D_j^T D_h^T \\ * & * & * & -\gamma^2 \mathbf{I} \end{bmatrix} < 0,$$

$$j = 1, \cdots, q,$$

$$R - X < 0. \tag{3.23}$$

The worst-case $\|G_{eu}\|_{H\infty}$ will be bounded by the optimized γ^* for all $\mathbf{T}$ described by Eq.(3.22).

When applying the robust H_∞ observer to estimate the temperature states in the battery string, we will consider the following system,

$$\begin{aligned} \Delta\dot{x} &= A\Delta x + \frac{\Delta R_e}{C_c} I^2 \\ \Delta y &= C\Delta x, \end{aligned} \tag{3.24}$$

which features only the state dynamics related to the resistance uncertainty ΔR_e. The remaining state dynamics can be estimated simply based on the nominal model. The A matrix is specified in Eq.(3.8), and ΔR_e in Eq.(3.9). The C matrix depends on the sensor location. We consider the estimation error e as the whole state estimation error e_x,

$$e_x = x - \hat{x}, \quad e_x \in \mathbb{R}^{2n} \tag{3.25}$$

and hence W is the identity matrix. According to the assumed constraint on resistance uncertain in Eq.(3.10), the following convex polytope can be used to describe the uncertain system,

$$T_j = \begin{bmatrix} A & \Delta B_j \\ C & 0 \end{bmatrix}, \quad j = 1, 2, \cdots, 2^n, \tag{3.26}$$

where

$$\begin{aligned}\Delta B_j &= \frac{1}{C_c}\begin{bmatrix}\Delta R_{e,1} & 0 & \Delta R_{e,2} & 0 & \cdots & \Delta R_{e,n} & 0\end{bmatrix}^T, \\ \Delta R_{e,i} &\in \{0.1R_{e,0}, -0.1R_{e,0}\}, \quad i = 1, 2, \cdots, n\end{aligned} \tag{3.27}$$

where n is the number of cells in the string.

The robust H_∞ observer design approach has been applied to a battery string with 10 cells and one temperature sensor available. The results will be shown in Section 3.5.4 and compared with the observer to be introduced next.

3.5.3 Observer Design for Minimizing the DC gain of the Estimation Error Transfer Function

As has been mentioned, the previously introduced H_∞ observer aims at minimizing the 2-norm of the estimation error transfer function G_{eu}. It is also interesting to investigate how much the largest estimation error among all the states can be reduced, which is the infinity norm of the error vector. Therefore, the minimization problem will become

$$\min_{\mathscr{F}} \sup_{\omega\in[0,+\infty),\Delta R_e} \|G_{eu}(j\omega)\|_\infty. \tag{3.28}$$

However, since the methodology for solving Eq.(3.28) has not been established yet, in this section, we simplify the problem as how to minimize the worst-case DC gain of the error transfer function, which is the case when $\omega = 0$. This observer will be referred to as the optimal DC observer. The underlying assumption is that the worst-case DC gain is the peak gain of the worst-case error transfer function,

$$\sup_{\omega\in[0,+\infty),\Delta R_e} \|G_{eu}(j\omega)\|_\infty = \sup_{\Delta R_e} \|G_{eu}(0)\|_\infty. \tag{3.29}$$

In Section 3.5.4, this assumption is shown to be valid for the design example.

Consider an observer taking the form of a Luenberger observer,

$$\begin{aligned}\dot{\hat{x}} &= A\hat{x} + B'u + L(y - \hat{y}) \\ \hat{y} &= C\hat{x}.\end{aligned} \tag{3.30}$$

It is noted that the input matrix is denoted as B' instead of B because there is uncertainty in battery resistance. The state estimation error dynamics can be derived by subtracting the observer dynamics in Eq. (3.30) from the plant dynamics in Eq.

(3.2), as

$$\dot{e}_x = (A - LC)e_x + \frac{\Delta R_e}{C_c} I^2, \tag{3.31}$$

where ΔR_e is the model uncertainty in battery resistance specified in Eq.(3.9). The error transfer function will be

$$\begin{aligned} E_x(s) &= G_{eu}(s) I^2(s) \\ G_{eu}(s) &= W(s\mathbf{I} - A + LC)^{-1} \frac{\Delta R_e}{C_c} \end{aligned} \tag{3.32}$$

The DC gain of the error transfer function,

$$G_{eu}(0) = -(A - LC)^{-1} \frac{\Delta R_e}{C_c}, \tag{3.33}$$

is a $2n \times 1$ vector, composed by the DC gain of the error transfer function for each temperature state.

The infinity norm, $\|G_{eu}(0)\|_\infty$, under all possible resistance uncertainty will be minimized during the observer design process, which can be formulated as optimization problems at the following three different levels.

i) Performance Evaluation: the performance of an observer (given sensor location specified in C and observer gain L) is defined as the worst-case DC gain of the error transfer function under all permissible ΔR_e,

$$\begin{aligned} \max_{\Delta R_e} \quad & \|G_{eu}(0)\|_\infty = \|(A - LC)^{-1}(\frac{\Delta R_e}{C_c})\|_\infty \\ \Delta R_e = & \begin{bmatrix} \Delta R_{e,1} & 0 & \Delta R_{e,2} & 0 & \cdots & \Delta R_{e,n} & 0 \end{bmatrix}^T, \\ s.t. & -0.1R_{e,0} \le \Delta R_{e,i} \le 0.1R_{e,0}, \quad i = 1, 2, \cdots, n \end{aligned} \tag{3.34}$$

ii) Observer Design: if the sensor location C is fixed but the observer gain L remains to be designed, an optimal observer looks at minimizing the worst-case DC gain,

$$\min_L \max_{\Delta R_e} \|(A - LC)^{-1}(\frac{\Delta R_e}{C_c})\|_\infty, \tag{3.35}$$

subject to the same constraints in Eq.(3.34).

iii) Sensor Deployment: if the sensor location C could also be chosen, the

sensor deployment problem will be

$$\begin{gathered}\min_{C}\min_{L}\max_{\Delta R_e}\|(A-LC)^{-1}(\frac{\Delta R_e}{C_c})\|_\infty, \\ \text{C s.t. permissible sensor locations}\end{gathered} \tag{3.36}$$

The first step is to determine the worst-case DC gain by solving the maximization problem in Eq.(3.34) with C and L given. It is noted that $\|G_{eu}(0)\|_\infty$ can be viewed as $2n$ linear and thus convex functions of ΔR_e. The infinity norm of $\|G_{eu}(0)\|_\infty$ will still be convex with respect to ΔR_e, since the maximum of multiple convex functions is still a convex function [105]. As ΔR_e is bounded by box constraints shown in Eq.(3.34), all permissible ΔR_e's form a compact convex set. According to the the maximum principle [106], the maximum of the convex cost function in Eq.(3.34) is attained on the boundary (or vertices) of the convex compact set formed by ΔR_e. The boundary is defined by the combinations of ΔR_e, whose elements, $\Delta R_{e,i}$, take either the upper bound or the lower bound,

$$\begin{gathered}\Delta R_e = \begin{bmatrix}\Delta R_{e,1} & 0 & \Delta R_{e,2} & 0 & \cdots & \Delta R_{e,n} & 0\end{bmatrix}^T \\ where \quad \Delta R_{e,i} \in \{0.1R_{e,0}, -0.1R_{e,0}\}, \quad \forall i = 1, \cdots, n\end{gathered} \tag{3.37}$$

The maximization problem in Eq.(3.34) is hence transformed to

$$\begin{gathered}\max_{\Delta R_e}\|(A-LC)^{-1}(\Delta R_e I^2)\|_\infty \\ \Delta R_e = \begin{bmatrix}\Delta R_{e,1} & 0 & \Delta R_{e,2} & 0 & \cdots & \Delta R_{e,n} & 0\end{bmatrix}^T \\ s.t. \quad \Delta R_{e,i} \in \{0.1R_{e,0}, -0.1R_{e,0}\}.\end{gathered} \tag{3.38}$$

For the case of 1 sensor available in 10 cells, the number of $\Delta R_{e,i}$'s is 10, and thus the total number of vertices is $2^{10} = 1024$. The worst-case DC gain can be found by evaluating the cost function at these 1024 vertices and choosing the maximum.

The next step is to design the observer gain L to minimize the worst-case DC gain of the error transfer function by solving Eq.(3.35). Several optimization methods are attempted here for the optimal observer design, which include applying i) Matlab command `fmincon` to minimize Eq.(3.38), and ii) Matlab command `fminimax`. The application of i) is straightforward.For ii), the built-in Matlab command `fminimax` is designed to minimize the maximum of a set of functions, which share a common variable. Here, the function set consists of $\|G_{eu}(0)\|_\infty$ evaluated at each vertex in Eq.(3.37), and the common variable is the observer gain L. However, it needs to be

pointed out that neither of the above two methods are convex optimization, as both cost functions are non-convex. Consequently, the optimization results may fall into local minimum. In order to reduce the likelihood of encountering local minimum, the two methods have been attempted under different initial guesses during the optimization procedures, and the same optimal results have been obtained (for the example to be discussed in the next section). The obtained observer gains have also been checked to satisfy the stability condition as $A - LC$ is Hurwitz.

Finally, for the sensor deployment problem in Eq.(3.36), the optimal sensor location (C) can be determined by solving Eq.(3.35) for all permissible sensor locations and choosing the one with the minimum $\|G_{eu}(0)\|_\infty$. For a cell string with 10 cells, the total number of C is 10 when 1 sensor is available, which measures the surface temperature of each cell respectively. The optimization results will be discussed in the next section.

3.5.4 Design Example: Optimal Observer Design to Estimate Temperature in a Battery String with 10 Cells and 1 Temperature Sensor

The two introduced observer design approaches have been applied to a cell string with 10 cells, and the cases when only 1 temperature sensor is available are considered. The performance of the two observers will be discussed and compared.

Figure 3.9 shows the worse-case H_∞ norm of the estimation error transfer function, $\|G_{eu}\|_{H\infty}$, under different sensor locations. The dashed line shows the worst-case $\|G_{eu}(0)\|_{H\infty}$ norms under open loop (using the model only), and the two solid lines show those of the two designed observers, namely the robust H_∞ observer and the optimal DC observer. It can be seen that the H_∞ observer could generally achieve better performance than the optimal DC observer (although the advantage is not significant). This is not surprising since the robust H_∞ observer is designed to minimize the worst-case $\|G_{eu}\|_{H\infty}$. The optimal sensor location is at Cell 7, where both observers show the largest reduction in $\|G_{eu}\|_{H\infty}$, i.e. from 0.0263 under open loop to 0.0158 under the H_∞ observer and 0.0162 under the optimal DC observer. The physical interpretation is that the ratio between the energy (L_2 norm) contained in the input $I^2(t)$ and that in the estimation error e_x will not exceed the above values under any resistance uncertainty satisfying the assumed bound. The cases of ΔR_e^* that yield the worst-case $\|G_{eu}\|_{H\infty}$ under some sensor locations are demonstrated in Fig. 3.10, which shows that ΔR_e^* is different for different sensor locations.

The worst-case DC gain of the estimation error transfer function, $\|G_{eu}(0)\|_\infty$, of the two observers are plotted in Fig. 3.11. It is seen that the optimal DC observer

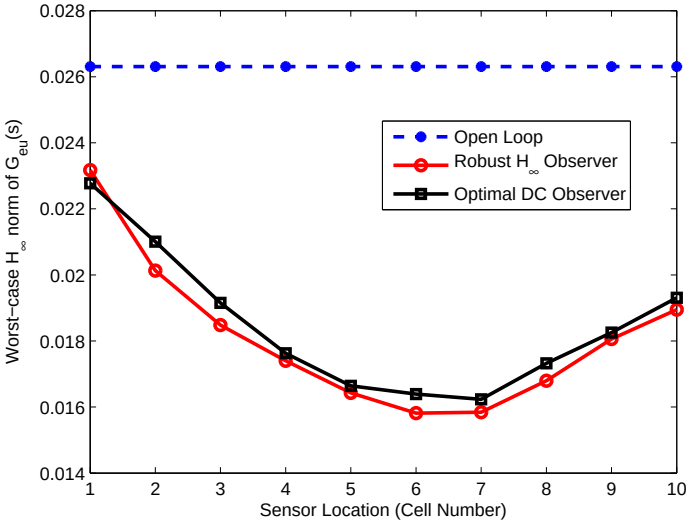

Figure 3.9: The Worst-case H_∞ Norm of the Estimation Error Transfer Function under Different Sensor Locations.

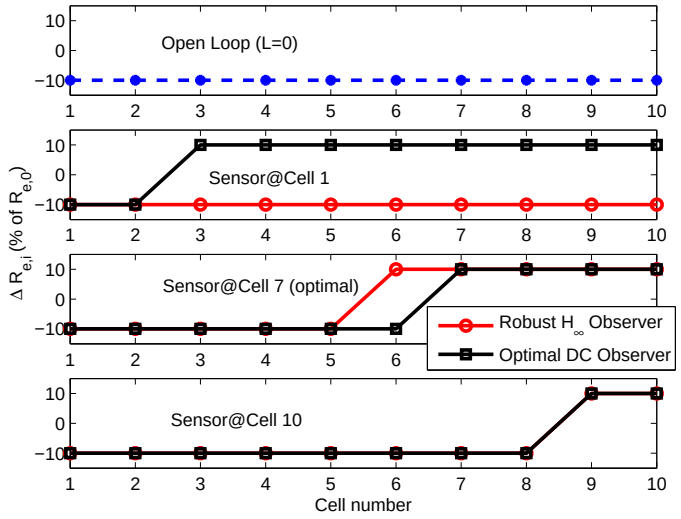

Figure 3.10: Cases of ΔR_e giving the worst-case estimation errors under different sensor locations.

outperforms the robust H_∞ observer in this aspect, since the former is designed to minimize the worst-case $\|G_{eu}(0)\|_\infty$. Like in the case of $\|G_{eu}\|_{H\infty}$, the optimal sensor location is at Cell 7, where the DC gain is reduced from 8.05e-3 under open loop to 5.48e-3 under the optimal DC observer, and 5.83e-3 under the robust H_∞ observer. These DC gains correspond to estimation errors of 4.26 ^oC, 2.86 ^oC and 3.09 ^oC under

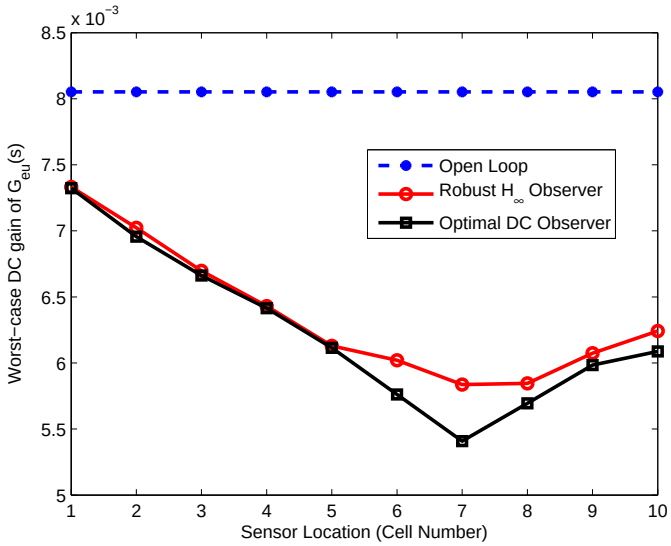

Figure 3.11: The Worst-case DC gain of the Estimation Error Transfer Function under Different Sensor Locations.

a constant current input (or symmetric charging-discharging current pulse train) of $10C$. The resistance uncertainty that gives the worst-case DC gain under some sensor locations are demonstrated in Fig. 3.12, which shows that ΔR_e^* is different for different sensor locations.

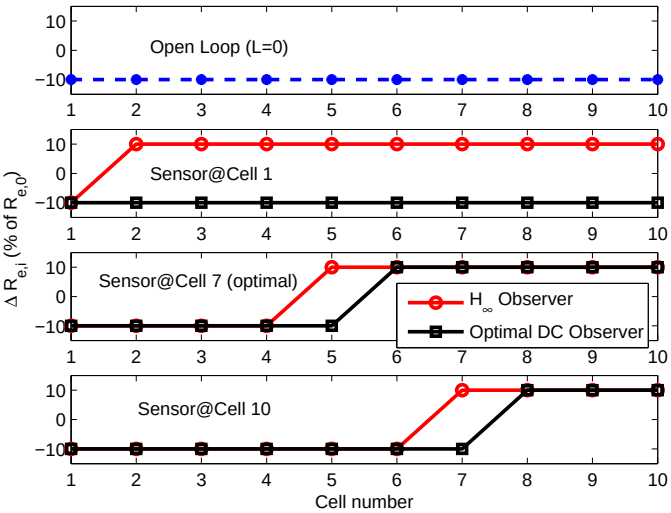

Figure 3.12: Cases of ΔR_e giving the worst-case estimation errors under different sensor locations.

In order to investigate the worst-case dynamic performance of the two observers, the worst-case magnitude of $G_{eu}(j\omega)$ under all possible resistance uncertainty over frequencies,

$$\max_{\Delta R_e} \|G_{eu}(j\omega)\|_\infty \tag{3.39}$$

is shown in Fig. 3.13. The temperature senor is placed at the optimal location, namely on the surface of Cell 7. The worst case defined in Eq.(3.39) is the maximum

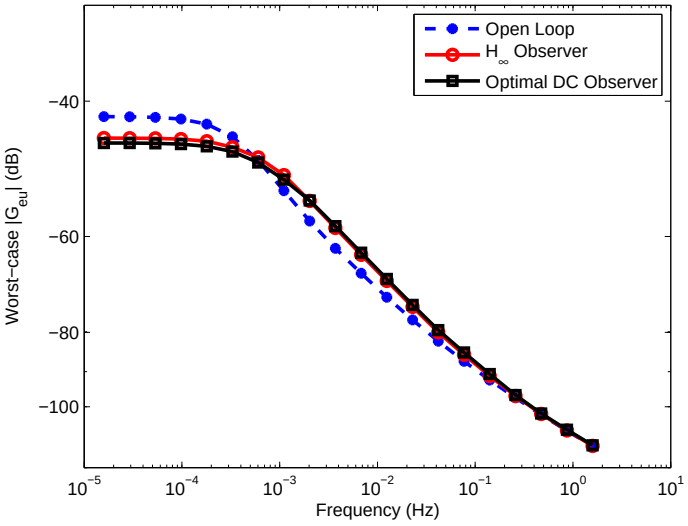

Figure 3.13: Cases of ΔR_e giving the worst-case estimation errors under different sensor locations.

in two sense. First, it is the maximum over all possible combinations of resistance uncertainty. Second, it is the maximum among all the states (20 in this case) as indicated by the infinity norm. As shown in the plot, for the optimal DC observer (as well as the robust H_∞ observer), the DC gain is actually the supreme of the worst case $\|G_{eu}(j\omega)\|_\infty$ over the frequencies, which validates the assumption in Eq.(3.29). The performance of the two observers are very similar, as both of them could achieve smaller error than open loop in low frequency range (below around $0.001Hz$), but worse in the middle frequency range ($0.001Hz - 0.1Hz$). The deteriorated performance in the middle frequency range is not critical due to the low gain in that range (less than -50 dB).

The performance of the designed observers have also been evaluated under drive-cycle simulation. As has been mention in Section 3.3.1, besides model uncertainty, temperature estimation may also be affected by errors in initial guesses. This issue is of particular interest for the following reasons. First, at every start-up, initial

temperature gradient could exist in a battery pack caused by factors such as external conditions and insufficient relaxation from previous operation [77, 107]. Due to the scarcity of the temperature sensor, the temperature gradient would turn into error in initial temperature estimation. Second, under open loop, although the initial errors would eventually die out since the thermal system is stable, the convergence would be seriously delayed by the slow battery thermal dynamics. This aspect is also considered in the drive-cycle simulation. The drive cycle is plotted in Fig. 3.14, where the top plot shows the current profile in C-rate. The evolution of the highest temperature, which is the core temperature of Cell 10, $T_{c,10}$, and the lowest temperature, namely the surface temperature of Cell 1, $T_{s,1}$, is demonstrated in the bottom plot to show the temperature gradient across the battery string. The current profile consists of three parts, a first sub-cycle, a 5 mins rest, and a second sub-cycle. Because the rest between the two sub-cycles are very short, the cells would not reach thermal equilibrium at the end of the rest, and temperature gradient exists across cells at the start of the second sub-cycle. Since only one temperature sensor is available, the reading of the sensor will be used to initialize all the temperature estimation, leading to initial errors in the states. The performance of the open-loop and the observers during the second sub-cycle is plotted in Fig. 3.15, which shows the maximum estimation error among all the states, $\|e_x\|_\infty$, at each time instant. The sensor is placed at the optimal location which is the surface of Cell 7, and the resistance uncertainty ΔR_e is the worst case under the optimal sensor location shown in Fig. 3.13, It can be seen that the two observers could not only reduce the estimation errors during "semi steady-state" operation after around t = 4000 s, but also accelerate the convergence from the initial estimation error. Specifically, the optimal DC observer could achieve (slightly) smaller estimation error during (semi-) steady-state, while the robust H_∞ observer converges faster from the initial estimation error. It is noted that the presented worst-case temperature estimation errors may not be considered as critical by some standards (even for the open loop estimation), which might justify the frugal sensor allocation that is being applied in the industry practice. It may also be due to the specific parameters and configuration of the battery string that is considered. The methodology developed here can be applied to other battery packs, whose parameters and configuration may induce more significant estimation errors in temperature estimation.

One interesting issue remains to be resolved for the robust temperature estimation problem is the relationship between the optimal performance of the observers and the observability of the battery string model. For a completely observable system, it is possible to design an observer that could (almost) eradicate the state estimation

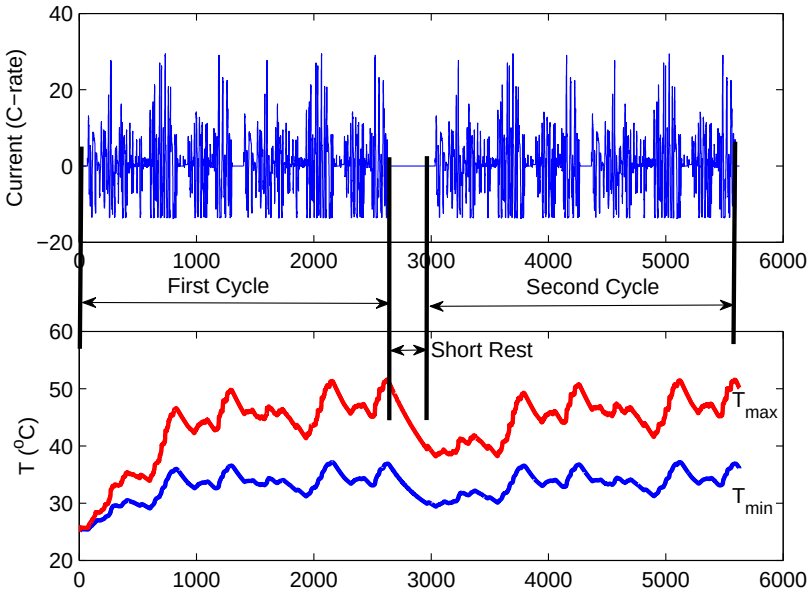

Figure 3.14: Drive-cycle Simulation (top plot: current in C-rate; bottom plot: evolution of highest temperature $T_{c,10}$ and lowest temperature $T_{s,1}$.

error under model uncertainty given clean output measurement. However, it is seen from Fig. 3.9 and Fig. 3.11 that the optimal observers designed for temperature estimation could only reduce the errors moderately. Furthermore, Fig. 3.13 shows that the observers could not even reduce the estimation error over all frequencies. It is speculated that the reason is related to the fact that the battery string model is not completely observable under the frugal sensor allocation. The detailed mechanism regarding fundamental limitation needs to be investigated in future work.

3.6 Conclusion

In this chapter, a one-dimensional battery string thermal model is constructed based on the single cell model for the purpose of temperature estimation on the pack level. Considered thermal interaction includes cell-to-cell thermal conduction and forced convection through the coolant flow. The string model can be further scaled up to multi-dimensional cell network by taking into account thermal interaction between cells in different rows. Different cooling strategies and pack configurations can be accommodated by tuning model parameters.

The observability of the string model is then investigated to enlighten the de-

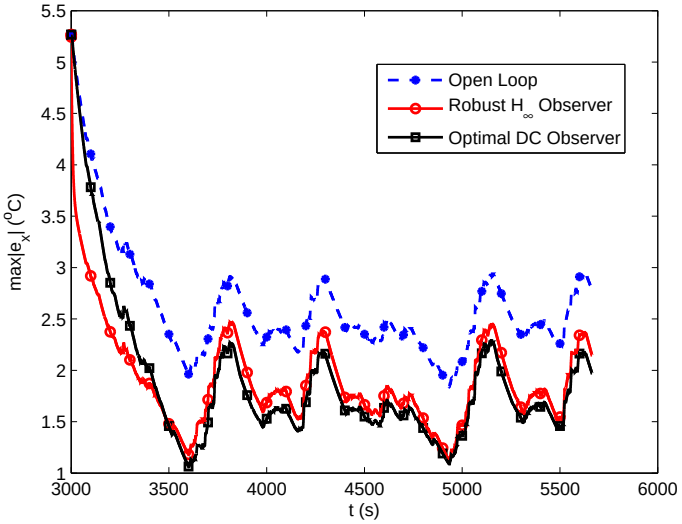

Figure 3.15: Evolution of the maximum estimation error among all states over time during the drive-cycle simulation.

ployment of temperature sensors. Minimum numbers of required sensors have been determined for strings with various lengths based on the observability condition. It is found that for strings with more than 5 cells, sensor location will also affect the observability. Viable combinations of sensor location have been studied for long strings under different conditions.

Nevertheless, the number of temperature sensors available in a commercial battery pack would not usually yield full observability to all the temperature states. Therefore, the observer needs to be designed under unobservable conditions. In this work, the objective is to minimize the worst-case estimation error under bounded uncertainty in cell resistance. Two optimal observer design approaches have been formulated and applied to a design example, where a battery string with 10 cells and 1 available temperature sensor are considered. The performance of the two observers are similar, which is somehow limited by the unobservable thermal model due to the frugal sensor allocation. With the designed observer and sensor location, it is guaranteed that the estimation errors in all the temperature states will be bounded by a specified value as long as the assumed bounds on model uncertainty hold.

CHAPTER IV

Estimating Individual Cell States of Charge under Reduced Voltage Sensing

4.1 Introduction

For lithium ion battery strings connected in series, reduced voltage sensing, where only the total voltage of the string is measured, is beneficial for cutting the cost and complexity of the battery management system. The reduced voltage sensing must retain the ability to prevent overcharge and overdischarge of all cells. Prior art for preventing or detecting overcharge and/or overdischarge in a reduced voltage sensing environment (such as those used with lead-acid or NiMH batteries) involves treating the cells in a given module as identical, perhaps combined with special, usually proprietary, tricks specific to the chemistry. One example might involve comparing voltage of one string of cells to that of the other cell strings in the pack. When all the cells are at the same SOC and voltage, the voltage of a single cell can be obtained by dividing the total voltage by the number of cells in series. When the cell SOCs and voltages are unbalanced, however, the voltage of a single cell cannot be inferred from the total voltage.

State of charge imbalance is present in all large battery packs, and it can be caused by a number of factors including manufacturing variability at manufacture, differing self-discharge rates, and varying rates of capacity change over life [82, 93, 108]. Furthermore, two cells that are at the same SOC can be at different voltages (under load) if their internal resistances are different. State of charge imbalance reduces the available energy in a pack, reducing electric range to PHEV and BEV customers. A small amount of SOC imbalance is of less concern in HEV batteries, since less of the full SOC operating range is typically used, but even in HEVs if imbalance grows too high the available charge and/or discharge power to the vehicle

is reduced.

Due to the common presence of SOC imbalance among cells, to avoid cell overcharge/overdischarge under reduced voltage sensing, the individual cell SOCs and voltages need to be estimated based on the total voltage. Such effort has been attempted in [109], where the single cell voltage is estimated based on the instantaneous change in total voltage before and after the balancing circuit is switched. The accuracy of the estimation, however, is compromised by the high ratio of the bypass resistance to the cell internal resistance. This method also requires manipulation of the balancing circuit.

In this chapter, the estimation of individual cell SOCs and voltages will be addressed solely based on the total voltage of cells connected in series [110, 111]. The basic idea is first introduced in Section 4.2, where it is shown that the cell SOCs are observable from the trajectory of the total voltage over time given nonlinear voltage versus SOC relationship. The estimation problem is then formulated mathematically based on defined assumptions and conditions. In Section 4.3, observability analysis is conducted to derive the necessary conditions for solving the estimation problem. In Section 4.4, five nonlinear observers are investigated, and the Newton observer is chosen as the most suitable candidate based on the comparison of advantages and disadvantages. Finally, the experimental validation of the Newton observer is provided in Section 4.5.

4.2 Basic Idea and Model Assumptions

In this section, it will be shown intuitively that the individual cell SOCs are observable from the trajectory of the total voltage over time if the battery voltage versus SOC relationship is nonlinear.

As an example for illustration, the voltage versus SOC relationship of a lithium iron phosphate ($LiFePO_4$) battery under a constant charging current is shown in Fig. 4.1. Assume at time t=0 second a total voltage of 6.88 V is measured across a two-cell string, there would be infinite combinations of individual cell SOCs giving this total voltage. Three of such combinations are given in Table 4.1, and shown in the inset of Fig. 4.1. It is not possible to distinguish these combinations based on the total voltage measurement at a single time instant. The SOC combinations are, however, distinguishable based on the trajectory of the total voltage over time. Under the constant charging current, trajectories of the total voltage over time in the three cases are shown in Fig. 4.2. It can be seen that due to the nonlinearity of the voltage

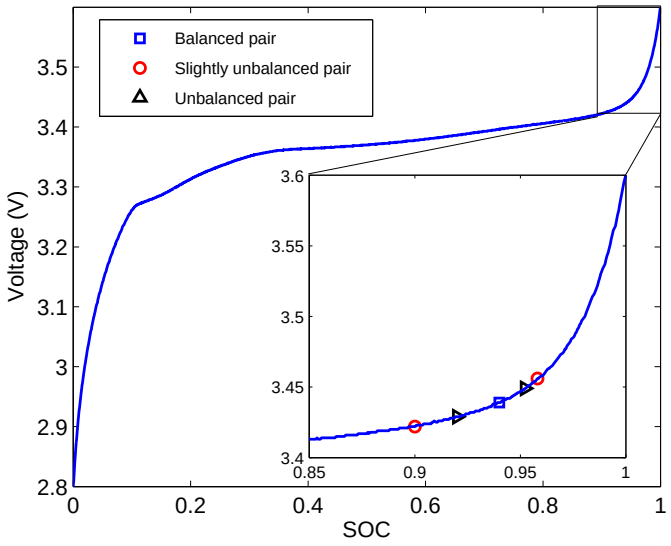

Figure 4.1: Voltage versus SOC relationship of a $LiFePO_4$ battery under a constant charging current. Inset: three SOC combinations giving the same total voltage as listed in Table 4.1.

Table 4.1: State of Charge Combinations Giving the Same Total Voltage Instantaneously.

	SOC_1	SOC_2	Total Voltage (V)
Balanced Pair	0.94	0.94	6.88
Slightly Unbalanced Pair	0.95	0.92	6.88
Unbalanced Pair	0.96	0.90	6.88

versus SOC relationship, the three trajectories are different. The main idea of this chapter is to estimate the single cell SOCs and voltages based on the trajectory of the total voltage over time.

In this section, the SOC estimation problem under reduced voltage sensing is analyzed under the following assumptions and conditions:

- Most of the analysis is conducted for reduced voltage sensing which measures two cell intervals, targeting 50% reduction in voltage sensing in a battery pack. The methodology can be extended to longer intervals but is subject to practical limitation to be discussed.

- The method is designed to estimate SOCs under the assumption that capacity and resistance are known and equal among cells. Possible cause of SOC imbalance under such circumstance is the difference among cells in self-discharge rate.

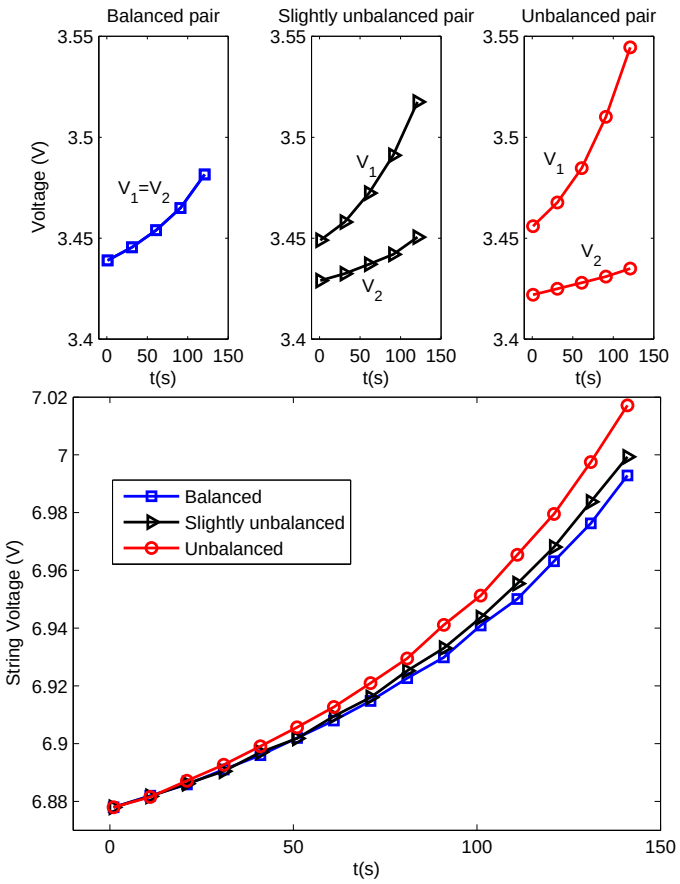

Figure 4.2: Voltage trajectory over time under a constant charging current of the three SOC combinations in Table 4.1 (three subplots on the top: trajectory of the individual cell voltages of each combination; bottom subplot: trajectories of the three total voltages).

- The operating condition is constant current charging, where a coulomb counting model is sufficient to capture the voltage dynamics. It is possible to apply the designed algorithm to real-world driving conditions with more complicated and accurate dynamic battery models.

The coulomb counting model used takes the form

$$\begin{aligned} x_{k+1} &= x_k + \frac{I\Delta t}{Q} \\ V_k &= g(x_k) + IR, \end{aligned} \tag{4.1}$$

where Δt is the sampling period, I is the current (positive for charging), Q is the battery capacity, and R is the ohmic resistance. The term $g(x)$ is a nonlinear relationship between battery voltage and SOC under the constant charging current, which may

include the open circuit voltage (OCV), hysteresis voltage, polarization over-potential among others. Consider a battery string with 2 cells connected in series, the string model can be written as,

$$\begin{aligned} x_{str,k} &= \begin{bmatrix} x_{1,k} & x_{2,k} \end{bmatrix}^T \\ x_{str,k+1} &= \begin{bmatrix} x_{1,k+1} \\ x_{2,k+1} \end{bmatrix} = \begin{bmatrix} x_{1,k} + \frac{I\Delta t}{Q} \\ x_{2,k} + \frac{I\Delta t}{Q} \end{bmatrix} \\ V_{str,k} &= V_{1,k} + V_{2,k} = g(x_{1,k}) + g(x_{2,k}) + 2IR, \end{aligned} \tag{4.2}$$

where subscripts 1 and 2 are used to denote the variables associated with cell 1 and 2. The goal of estimation is to determine $x_{1,k}$ and $x_{2,k}$ when I is known and V_{str} is measured over a period of time.

4.3 Observability Analysis

In order to solve the estimation problem, the observability of the individual cell SOCs under reduced voltage sensing needs to be investigated first. The derived observability condition is shown to be dependent on the nonlinearity of the voltage-SOC relationship. Extension to general cases (n cell intervals) is also discussed.

Starting from time step k, the trajectory of the total voltage V_{str} over $N+1$ consecutive time steps $k, k+1, ..., k+N$, $V_{str,[k,k+N]}$, can be denoted as

$$V_{str,[k,k+N]} = \begin{bmatrix} V_{str,k} \\ V_{str,k+1} \\ ... \\ V_{str,k+N} \end{bmatrix} = \begin{bmatrix} g(x_{1,k}) + g(x_{2,k}) \\ g\big(x_{1,k+1}\big) + g\big(x_{2,k+1}\big) \\ ... \\ g\big(x_{1,k+N}\big) + g\big(x_{2,k+N}\big) \end{bmatrix} + 2IR. \tag{4.3}$$

Based on the battery string model under constant current charging in Eq. (4.2), $V_{str,[k,k+N]}$ can be further written as a function of the initial states, $x_{str,k}$, as

$$V_{str,[k,k+N]} = H(x_{str,k}) = \begin{bmatrix} g(x_{1,k}) + g(x_{2,k}) \\ g\big(x_{1,k} + \frac{I\Delta t}{Q}\big) + g\big(x_{2,k} + \frac{I\Delta t}{Q}\big) \\ ... \\ g\big(x_{1,k} + \frac{NI\Delta t}{Q}\big) + g\big(x_{2,k} + \frac{NI\Delta t}{Q}\big) \end{bmatrix} + 2IR. \tag{4.4}$$

By taking the partial derivative of H to $x_{str,k}$, deviation of the trajectory caused by

variation in the initial states can be obtained as,

$$\begin{aligned}\delta V_{str,[k,k+N]} &= \frac{\partial H}{\partial x_{str,k}}\delta x_{str,k} \\ \frac{\partial H}{\partial x_{str,k}} &= \begin{bmatrix} g'(x_{1,k}) & g'(x_{2,k}) \\ g'\big(x_{1,k}+\frac{I\Delta t}{Q}\big) & g'\big(x_{2,k}+\frac{I\Delta t}{Q}\big) \\ ... & ... \\ g'\big(x_{1,k}+\frac{NI\Delta t}{Q}\big) & g'\big(x_{2,k}+\frac{NI\Delta t}{Q}\big) \end{bmatrix},\end{aligned} \tag{4.5}$$

where $g'(x)$ denotes the gradient of $g(x)$ to x. In Eq. (4.5), $\delta x_{str,k}$ represents the deviation of initial SOCs from the nominal point, $x^0_{str,k}$, that is, $\delta x_{str,k} = x_{str,k} - x^0_{str,k}$. For example, for the three cases in Table 4.1, if the nominal guess is defined at the balanced combination, $x^0_{str,k} = [0.94, 0.94]^T$, $\delta x_{str,k}$ of the three cases would be

$$\begin{aligned} &\delta x_{1,k} = \delta x_{2,k} = 0, \quad \text{for the balanced pair,} \\ &\delta x_{1,k} = -0.02, \quad \delta x_{2,k} = 0.01 \quad \text{for the slightly unbalanced pair,} \\ &\delta x_{1,k} = -0.04, \quad \delta x_{2,k} = 0.02 \quad \text{for the unbalanced pair.} \end{aligned} \tag{4.6}$$

Estimating $x_{str,k}$ is equivalent to estimating $\delta x_{str,k}$. In order for $\delta x_{str,k}$ to be observable from $\delta V_{str,[k,k+N]}$, $\frac{\partial H}{\partial x_{str,k}}$ needs to be a one-to-one mapping and hence of full rank (rank = 2). In fact, $\frac{\partial H}{\partial x_{str,k}}$ is by definition the observability matrix of the nonlinear discrete-time system in Eq. (4.2) [112],

$$O_D(x_{str,k}) = \frac{\partial H}{\partial x_{str,k}}(x_{str,k}). \tag{4.7}$$

The reason that $x_{str,k}$ cannot be observed from the measurement of $V_{str,k}$ at a single time instant can be found in the observability matrix. With only $V_{str,k}$, Eq. (4.5) is reduced to

$$\delta V_{str,k} = O_D(x_{str,k})\delta x_{str,k} = \begin{bmatrix} g'(x_{1,k}) & g'(x_{2,k}) \end{bmatrix} \delta x_{str,k}. \tag{4.8}$$

The observability matrix only has one row, and thus its rank is one. Rank deficiency indicates that there are infinite numbers of $\delta x_{str,k}$ that could match the single $\delta V_{str,k}$. Only when multiple V_{str} data are processed at the same time, would the $O_D(x_{str,0})$ matrix have more than one rows and hence be possible to have full rank. Still, more rows do not necessarily guarantee observability. For example, when $g(x)$ is linear and $g'(x)$ is constant, additional rows do not make O_D full rank, since the two columns

of O_D are identical. Necessary conditions on $g(x)$ for observability will be discussed next.

The discrete-time observability matrix in Eq. (4.5) can be transformed to the continuous-time observability matrix, as

$$O_C(x_{str,k}) = \begin{bmatrix} g'(x_{1,k}) & g'(x_{2,k}) \\ g''(x_{1,k})\frac{I}{Q} & g''(x_{2,k})\frac{I}{Q} \end{bmatrix}, \tag{4.9}$$

where $g''(x)$ denotes the second order gradient of $g(x)$ to x. This O_C matrix can also be obtained based on the Lie derivatives of the continuous battery string model [63, 110]. The first order gradient of $g(x)$, $g'(x)$, is usually positive, since the battery voltage normally increases monotonically with SOC. Therefore, for $O_C(x_{str})$ to be of full rank, it is necessary that either $g''(x_{1,k})$ or $g''(x_{2,k})$ needs to be non-zero, which means that $g(x)$ should be nonlinear. Two lithium-ion battery chemistries are taken as examples for illustration.

The $g(x)$ function of a $LiFePO_4$ battery under 1C constant charging current is plotted in Fig. 4.3, along with its first and second order gradients. It can be seen that in the middle SOC range, 15%-90%, $g(x)$ is almost linear, with small first and second order gradients. As a result, the observability matrix O_C will be practically rank deficient. At the high and low SOC ends, namely 0%-15% and 90%-100%, $g(x)$ is highly nonlinear with significant $g'(x)$ and $g''(x)$. These regions are where the precaution against overcharge and overdischarge is critically needed. Fortunately, the highly nonlinear $g(x)$ in these ranges renders significant observability to the individual cell SOCs and voltages. It is noted that for the $LiFePO_4$ chemistry, SOC is barely observable in the middle SOC range even under full voltage sensing, due to the flatness of $g(x)$.

As another example, $g(x)$ of a LiNiMnCo (LiNMC) battery and its first and second order gradients are shown in Fig. 4.4. For this battery chemistry, the strongly observable SOC range is below 10%, where both $g'(x)$ and $g''(x)$ are large enough. When the SOC is above 10%, linear $g(x)$ (nearly zero $g''(x)$) inhibits the observability under reduced voltage sensing. Slight nonlinearity is noted around 80% SOC, rendering that range weakly observable.

When the total voltage is measured for every n cells, $n > 2$, observability analysis can be conducted in a similar way. By using the Lie-derivative analysis, the continuous-time observability matrix is obtained as Eq. (4.10), where the superscript (i) denotes the ith order gradient of $g(x)$ to x. More details on the derivation can be found in [110].

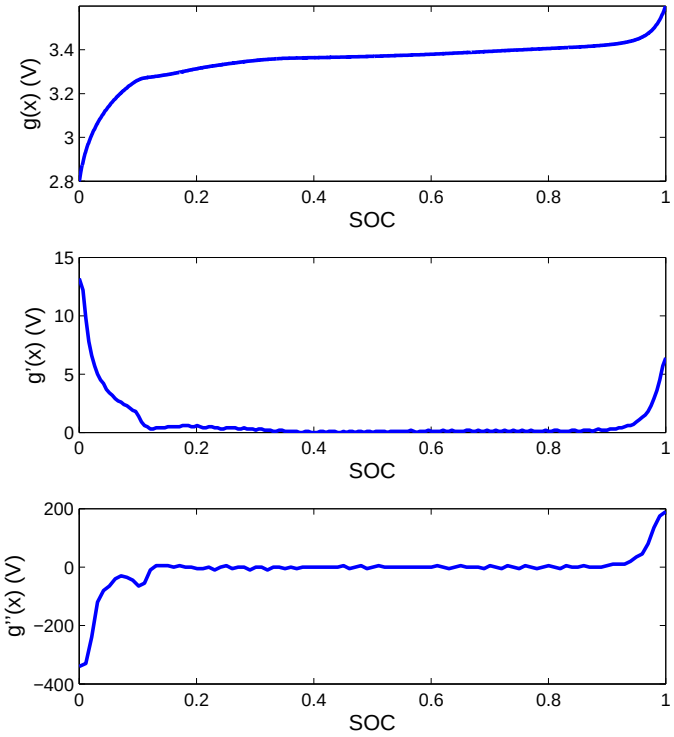

Figure 4.3: Voltage function $g(x)$ of a LiFePO4 battery under a constant charging current and its gradients (upper: g(x); middle: first order gradient $g'(x)$; bottom: second order gradient $g''(x)$).

As seen from Eq. (4.10), when only the total voltage of every n cells is measured, up to nth order gradients of $g(x)$ need to be checked. In order for the observability matrix to be of full rank (rank=n), at least one of each $g^{(i)}(x)$ should be nonzero. Ultimately, the eigenvalues of $O_C(x_{str,k})$ need to be calculated, and full rank requires all the eigenvalues to be nonzero. This part of work is to be addressed in detail in future, and it is foreseeable that reducing voltage sensors further requires stronger nonlinearity on $g(x)$, which could be challenging in practice.

4.4 Candidate Nonlinear Observers

It has been established by the observability analysis that under reduced voltage sensing, individual cell SOCs are observable, and hence can be estimated, given nonlinear voltage versus SOC relationship. In order to find the most suitable algorithm for SOC estimation, various nonlinear observers will be explored, which includes the

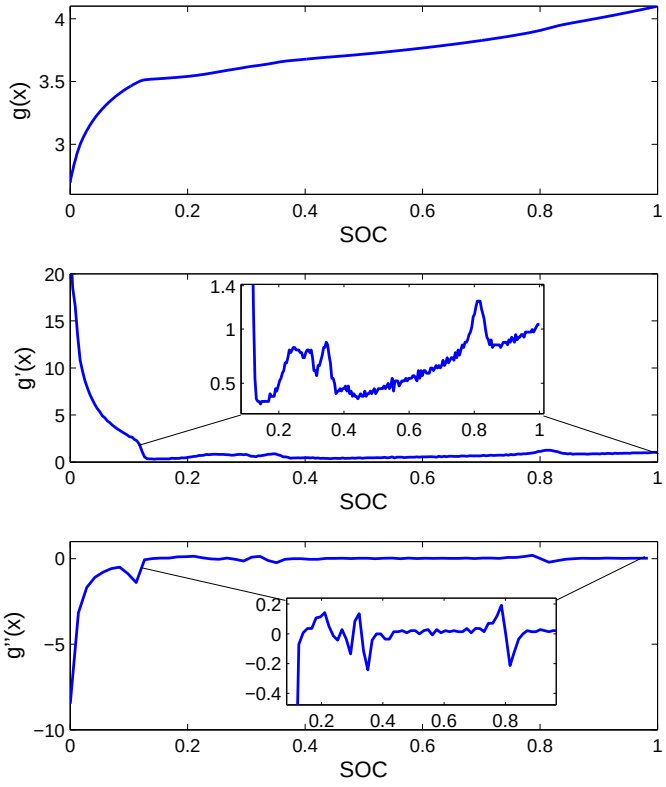

Figure 4.4: Voltage function $g(x)$ of a LiNMC battery under a constant charging current and its gradients (upper: g(x); middle: first order gradient $g'(x)$; bottom: second order gradient $g''(x)$).

extended Kalman filter (EKF) [59, 60], canonical form observer [66, 68, 72, 73], extended Luenberger observer [69], sliding mode observer [70, 71] and Newton observer [64, 65]. After analyzing the applicability, advantages and disadvantages of each observer in the context of reduced voltage sensing, the Newton observer is considered as the most suitable candidate. To illustrate the principles of different algorithms, a generic nonlinear model either in continuous time,

$$\begin{aligned} \dot{x} &= f(x), \quad x \in \mathbf{R}^n, \\ y &= h(x), \quad y \in \mathbf{R} \end{aligned} \tag{4.11}$$

or in discrete time,

$$\begin{aligned} x_{k+1} &= f_d(x_k) \\ y_k &= h(x_k), \end{aligned} \tag{4.12}$$

$$O_C(x_{str,k}) = \begin{bmatrix} g'(x_{1,k}) & g'(x_{2,k}) & ... & g'(x_{n,k}) \\ g''(x_{1,k})\frac{I}{Q} & g''(x_{2,k})\frac{I}{Q} & ... & g''(x_{n,k})\frac{I}{Q} \\ & \cdots & & \\ g^{(i)}(x_{1,k})\left(\frac{I}{Q}\right)^{i-1} & g^{(i)}(x_{2,k})\left(\frac{I}{Q}\right)^{i-1} & ... & g^{(i)}(x_{n,k})\left(\frac{I}{Q}\right)^{i-1} \\ & \cdots & & \\ g^{(n)}(x_{1,k})\left(\frac{I}{Q}\right)^{n-1} & g^{(n)}(x_{2,k})\left(\frac{I}{Q}\right)^{n-1} & ... & g^{(n)}(x_{n,k})\left(\frac{I}{Q}\right)^{n-1} \end{bmatrix} \tag{4.10}$$

will be used, where the subscript k denotes the time step, x and y are the state and output of the model, f and f_d are the equivalent nonlinear state functions in continuous time and discrete time, and h is the output function. It is noted that in Eq.(4.11) and Eq.(4.12), f, f_d, and h are written as functions of the state x only, but not of any input u. This is because, as has been mentioned, the considered operating condition for SOC estimation under reduced voltage sensing is constant current charging, and thus the input current can be included in the state and output functions as a constant.

4.4.1 Extended Kalman Filter

The extended Kalman filter is one of the most commonly used methods for online estimation of battery SOC when full voltage sensing is available [53, 60, 61]. It will be shown that under reduced voltage sensing, however, the SOC estimation of EKF will not converge due to lack of observability of the linearized battery string model.

When EKF is applied, at each step, the state is first calculated based on the model as the predicted state estimate $\hat{x}_k^-$, and then updated based on the output measurement to obtain the final estimate x_k^+. For the discrete nonlinear system in Eq. (4.12), the predicted state estimate is

$$\hat{x}_k^- = f_d(\hat{x}_{k-1}^+), \tag{4.13}$$

where $\hat{x}_{k-1}^+$ is the final (updated) state estimate at the previous step. The state covariance matrix P_k is also predicted as

$$P_k^- = \frac{\partial f_d}{\partial x}(\hat{x}_{k-1}^+)P_{k-1}^+\frac{\partial^T f_d}{\partial x}(\hat{x}_{k-1}^+) + \Sigma_p, \tag{4.14}$$

where Σ_p is the covariance of the process noise. The Kalman observer gain is then

calculated as

$$K_k = P_k^- \frac{\partial^T h}{\partial x}(\hat{x}_k^-)\big[\frac{\partial h}{\partial x}(\hat{x}_k^-)P_k^- \frac{\partial^T h}{\partial x}(\hat{x}_k^-) + \Sigma_m\big]^{-1}, \tag{4.15}$$

where Σ_m is the covariance of the measurement noise. Finally, the observer gain K_k is used to update the estimates of the x_k and P_k based on the output estimation error,

$$\begin{aligned} \hat{x}_k^+ &= \hat{x}_k^- + K_k[y_k - h(\hat{x}_k^-)] \\ P_k^+ &= (\mathbf{I} - K_k)P_k^- \frac{\partial^T h}{\partial x}(\hat{x}_k^-), \end{aligned} \tag{4.16}$$

where $\mathbf{I}$ is the identify matrix.

As can be seen from Eq.(4.14) and Eq.(4.15), EKF is based on linearization of the nonlinear system, as the observer gain is calculated by using the Jacobian $\frac{\partial f_d}{\partial x}(\hat{x}_{k-1}^+, u_{k-1})$ and $\frac{\partial h}{\partial x}(\hat{x}_k^-, u_{k-1})$. In fact, the convergence of the estimate by EKF is guaranteed only if the system retains observability after linearization [59]. Unfortunately, this condition cannot be satisfied under reduced voltage sensing. After linearization, the battery string model in Eq.(4.2) is transformed to

$$\begin{aligned} x_{str,k+1} &= Ax_{str,k} + BI \\ V_{str,k} &= Cx_{str,k} + DI, \end{aligned} \tag{4.17}$$

where

$$A = \begin{bmatrix} 1 & 0 \\ 0 & 1 \end{bmatrix}, \quad B = \begin{bmatrix} \frac{\Delta t}{Q} \\ \frac{\Delta t}{Q} \end{bmatrix}, \quad C = \begin{bmatrix} g'(x_{1,k}) & g'(x_{2,k}) \end{bmatrix}, \quad D = 2R. \tag{4.18}$$

In order for the linearized model to be observable, the observability matrix

$$O_{lin} = \begin{bmatrix} C \\ CA \end{bmatrix} = \begin{bmatrix} g'(x_{1,k}) & g'(x_{2,k}) \\ g'(x_{1,k}) & g'(x_{2,k}) \end{bmatrix} \tag{4.19}$$

needs to be of full rank, which is clearly not satisfied considering identical rows (and columns) of O_{lin}.

Simulation has been conducted to show that EKF is inadequate for SOC estimation under reduced voltage sensing. The model of a two-cell $LiFePO_4$ string is used to emulate the total voltage measurement. The SOCs of the two cells are initialized to 90% and 85% respectively, and the initial guess of SOC in EKF is set to around 80% for both cells. The SOC estimation of EKF is shown in Fig. 4.5. It can be

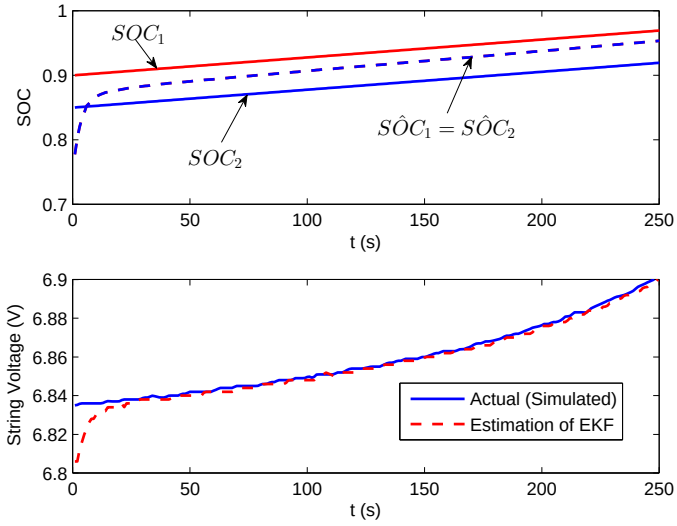

Figure 4.5: State of Charge Estimation of EKF under Reduced Voltage Sensing.

seen that EKF could only track the average SOC of the two-cell string by matching the total voltage, but not the SOCs of the individual cells. As a result, the cell with higher SOC (cell 1) is under the risk of being overcharged, and EKF is hence not suitable for SOC estimation under reduced voltage sensing.

4.4.2 Canonical Form Observer

The canonical form observer [72, 73, 66, 68], as the name implies, seeks to transform the nonlinear system model into a canonical form, similar to that of a linear system, based on which an observer can be designed easily. Such observer may take the form of a high-gain observer [72, 73] or be designed based on observer error linearization [66, 68].

To obtain the canonical form of the generic continuous nonlinear model in Eq.(4.11), the commonly used coordinate transformation, $x \rightarrow z$, is defined by using the Lie derivatives of the output function h (or the time derivative of the output y),

$$\begin{aligned} z_1 &= y = h(x) = L_f^0 h(x) \\ z_2 &= \dot{y} = \frac{\partial h}{\partial x} f(x) = L_f h(x), \\ &\cdots \\ z_i &= y^{(i-1)} = L_f^{i-1} h(x) = L_f (L_f h)(x), \quad i = 3, ...n, \end{aligned} \tag{4.20}$$

where the superscript (i) denotes the ith time derivative, and $L_f^i h$ is the symbol for the ith Lie derivative. If the time derivative of the last transformed state, $\dot{z}_n$, can be expressed as a function of the states $z_1, \cdots, z_n$,

$$z_n = \phi(z_1, \cdots, z_n), \tag{4.21}$$

an observer canonical form is obtained as

$$\begin{aligned} \dot{z} = \begin{bmatrix} \dot{z}_1 \\ \dot{z}_2 \\ \cdots \\ \dot{z}_{n-1} \\ \dot{z}_n \end{bmatrix} = \begin{bmatrix} z_2 \\ z_3 \\ \cdots \\ z_n \\ \phi(z) \end{bmatrix} = \begin{bmatrix} 0 & 1 & 0 & \cdots & 0 \\ 0 & 0 & 1 & \cdots & 0 \\ & & & \ddots & \\ 0 & & \cdots & & 1 \\ 0 & & \cdots & & 0 \end{bmatrix} z + \begin{bmatrix} 0 \\ 0 \\ \vdots \\ \phi(z) \end{bmatrix} = f_{can}(z) \\ y = z_1 = \begin{bmatrix} 1 & 0 & \cdots & 0 \end{bmatrix} z = C_{can} z. \end{aligned} \tag{4.22}$$

Based on the canonical form, the observer can then be designed as a high gain observer or based on observer error linearization. The high gain observer takes the form [72, 73]

$$\begin{aligned} \dot{\hat{z}} &= f_{can}(\hat{z}) - L_\infty^{-1} C_{can}^T (y - \hat{y}), \\ \hat{y} &= \hat{z}_1, \end{aligned} \tag{4.23}$$

where the observer gain L_∞ is determined by solving

$$\begin{aligned} &-\eta L_\infty - A_S^T L_\infty - L_\infty A_S + C_{can}^T C_{can} = 0, \\ &A_S = \begin{bmatrix} 0 & 1 & 0 & \cdots & 0 \\ 0 & 0 & 1 & \cdots & 0 \\ & & & \ddots & \\ 0 & & \cdots & & 1 \\ 0 & & \cdots & & 0 \end{bmatrix}, \end{aligned} \tag{4.24}$$

with η large enough. Exponential convergence of $\hat{z}$ is guaranteed and the original states can be determined based on the inverse coordinate transformation $z \to x$. When the observer is designed based on observer error linearization [66, 68], the function $\phi(z)$ in Eq.(4.21) is further assumed to be

$$\dot{z}_n = a_1 z_1 + a_2 z_2 + \cdots + a_n z_n, \tag{4.25}$$

where a_i's are constant coefficients. In this way, the canonical form in Eq.(4.22) is further written as

$$\begin{aligned} \dot{z} = A_{can} z &= \begin{bmatrix} 0 & 1 & 0 & \cdots & 0 \\ 0 & 0 & 1 & \cdots & 0 \\ & & & \ddots & \\ 0 & & \cdots & & 1 \\ a_1 & a_2 & \cdots & & a_n \end{bmatrix} z \\ y &= C_{can} z. \end{aligned} \tag{4.26}$$

A Luenberger observer,

$$\begin{aligned} \dot{\hat{z}} &= A_{can}\hat{z} + L(y - \hat{y}) \\ \hat{y} &= C_{can}\hat{z}, \end{aligned} \tag{4.27}$$

can then be designed to converge the estimate of z, with the observer gain L designed to stabilize the error dynamics,

$$\begin{aligned} e &= z - \hat{z}, \\ \dot{e} &= (A_{can} - LC_{can})e. \end{aligned} \tag{4.28}$$

It is noted that for the observer error linearization method, the transformed model may also include a nonlinear output injection term [66, 68].

Although the design process is straightforward, the greatest challenge lies in the coordinate transformation. In many cases, it is extremely difficult, if ever possible, to find a function $\phi(z)$ that could satisfy Eq.(4.21) or Eq.(4.25). This is especially true for the battery string model, where the voltage output function $g(x)$ is usually measured and stored as a look-up table and thus does not have an analytical form. Though hardly applicable in the SOC estimation problem under reduced voltage sensing, the idea of the canonical form observer, gives rise to the interests in the following two observers, the sliding mode observer and the extended Luenberger observer.

4.4.3 Sliding Mode Observer

The sliding mode observer [70, 71], which is based on the equivalent control method [113], is another type of algorithm that can be used for nonlinear state estimation problems. For nonlinear sliding mode estimation, the first step is to find certain sliding surfaces, which need to be in one-to-one correspondence with the states. The

observer is then designed to confine the estimated system dynamics around the sliding surfaces. The state estimates will hence stay around the actual states due to the one-to-one correspondence. The sliding mode observer considered here is in the form introduced in [71], where the Lie derivatives shown in Eq.(4.20) are defined as the sliding surfaces. Compared with the canonical form observer, however, the sliding mode estimation does not require transforming the model into the coordinate in Lie derivatives.

For the generic continuous nonlinear system in Eq.(4.11), sliding surfaces are defined as the Lie derivatives of the output function h, which are the $z_1, z_2, \cdots, z_n$ in Eq.(4.20). The mapping between the states x and the sliding surfaces z is a one-to-one correspondence if the nonlinear system is observable. The sliding mode observer is then designed as

$$\dot{\hat{x}} = \big(\frac{\partial z}{\partial x}(\hat{x})\big)^{-1} M(\hat{x}) sgn\big(\xi - z(\hat{x})\big), \tag{4.29}$$

where sgn is the sign function, and $M(\hat{x})$ is a diagonal gain matrix with entries $m_1(\hat{x}), m_2(\hat{x}), ..., m_n(\hat{x})$, whose values are to be designed. The column vector ξ consists of n elements,

$$\begin{aligned} &\xi_1 = y \\ &\xi_i = m_i(\hat{x}) sgn\big(\xi_{i-1} - z_{i-1}(\hat{x})\big), \quad i = 2, \cdots, n. \end{aligned} \tag{4.30}$$

As has been proven in [71], if $m_i(\hat{x})$ is chosen as

$$m_i(\hat{x}) \geq |z_{i+1}(x)|, \tag{4.31}$$

the term $M(\hat{x}) sgn\big(\xi - z(\hat{x})\big)$ guarantees the sliding mode of $\hat{z}$ around z, and $\big(\frac{\partial z}{\partial x}\big)^{-1}$, as the mapping between the sliding mode of z and the sliding mode of x, ensures that $\hat{x}$ will slide along x. It is noted that $\frac{\partial z}{\partial x}$ is also the observability matrix of the continuous nonlinear model. Inversion of $\frac{\partial z}{\partial x}$ requires it to be of full rank, which implies that the model needs to be observable.

When applied to the SOC estimation problem under reduced voltage sensing, the

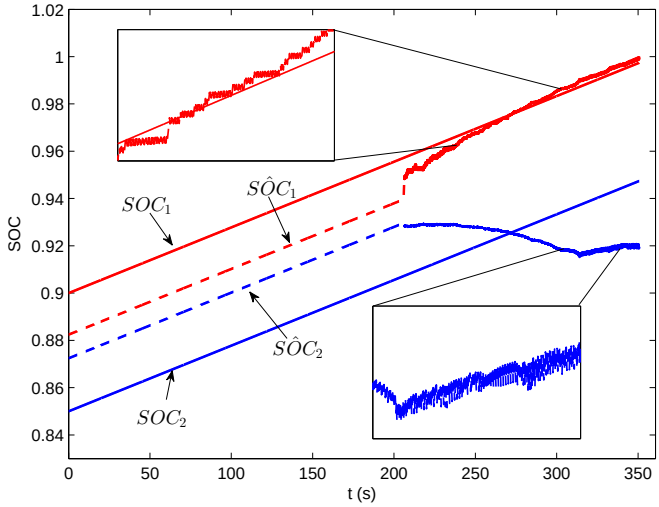

Figure 4.6: State of Charge Estimation of the Sliding Mode Observer under Reduced Voltage Sensing.

corresponding terms in Eq.(4.29) can be obtained as

$$
\begin{aligned}
z &= \begin{bmatrix} z_1 \\ z_2 \end{bmatrix} = \begin{bmatrix} g(x_1) + g(x_2) \\ \big(g'(x_1) + g'(x_2)\big)\frac{I}{Q} \end{bmatrix} \\
\frac{\partial z}{\partial x}(\hat{x}) &= \begin{bmatrix} g'(\hat{x}_1) & g'(\hat{x}_2) \\ g''(\hat{x}_1)\frac{I}{Q} & g''(\hat{x}_1)\frac{I}{Q} \end{bmatrix} \\
\xi &= \begin{bmatrix} V_{str} \\ m_1 sgn\big(V_{str} - g'(\hat{x}_1) - g'(\hat{x}_2)\big) \end{bmatrix},
\end{aligned}
\tag{4.32}
$$

with

$$
\begin{aligned}
m_1 &\geq \Big|\big(g'(x_1) + g'(x_2)\big)\frac{I}{Q}\Big| = |\dot{V}_{str}|, \\
m_2 &\geq \Big|\big(g''(x_1) + g''(x_2)\big)\big(\frac{I}{Q}\big)^2\Big| = |\ddot{V}_{str}|.
\end{aligned}
\tag{4.33}
$$

Simulation has been conducted to show the performance of the sliding mode observer, where the model of a two-cell $LiFePO_4$ string with 5% SOC imbalance is again used to emulate the total voltage measurement. The SOC estimation of the sliding mode observer is plotted in Fig. 4.6, and the sliding mode of $\hat{z}$ around the sliding surface z is shown in Fig. 4.7. During the simulation, the sliding mode observer is enabled after the SOCs reach the strongly observable range ($> 90\%$), when the $\frac{\partial z}{\partial x}$ matrix could be

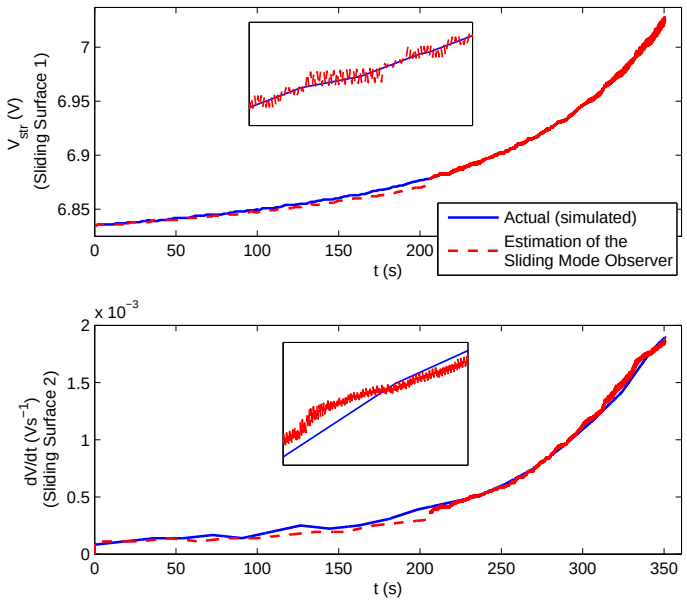

Figure 4.7: State of Charge Estimation of the Sliding Mode Observer under Reduced Voltage Sensing.

robustly inverted. As seen in the simulation, the SOC estimates then start to evolve toward the actual SOCs in chattering motion. At the end, however, although both $\hat{z}_1$ and $\hat{z}_2$ slide closely around the actual sliding surface, the SOC estimates do not chatter around the actual SOCs closely as expected, and significant estimation errors are observed for SOC_2. The reason is attributed to the modeling errors in $\frac{\partial z}{\partial x}$. As seen in Eq.(4.32), $\frac{\partial z}{\partial x}$ includes the second order gradient of the voltage-SOC relationship $g''(x)$, which is very difficult to model accurately. The voltage output function $g(x)$ is measured based on experiment, and $g''(x)$, which is obtained by performing the spline-fitting-differentiation process twice, could be easily corrupted by measurement noises. The errors in $g''(x)$ will affect the accuracy of the sliding mode mapping $\frac{\partial z}{\partial x}$, leading to biased SOC estimation despite good sliding mode on z.

4.4.4 Extended Luenberger Observer

The extended Luenberger Observer [69] is a nonlinear state estimation algorithm taking the similar form as a Luenberger Observer for linear systems. Unlike the canonical form observer, the extended Luenberger observer performs the estimation directly in the original coordinate, avoiding the coordinate transform by using extended linearization.

For the generic continuous nonlinear system in Eq.(4.11), the extended Luenberger observer takes the form

$$\begin{aligned}\dot{\hat{x}} &= f(\hat{x}) + L(\hat{x})(y - \hat{y}) \\ \hat{y} &= h(\hat{x}).\end{aligned} \tag{4.34}$$

The observer gain L is designed as dependent on the state estimate $\hat{x}$,

$$\begin{aligned}L(\hat{x}) =& [p_0 \cdot ad_f^0 + p_1 \cdot ad_f^1 + ... + p_{n-1} \cdot ad_f^{n-1} + ad_f^n] \circ S(\hat{x}) \\ S(\hat{x}) =& \begin{bmatrix} \frac{\partial L_f^0 h(x)}{\partial x} \\ \frac{\partial L_f h(x)}{\partial x} \\ \vdots \\ \frac{\partial L_f^{n-1} h(x)}{\partial x} \end{bmatrix}^{-1} \begin{bmatrix} 0 & 0 & \cdots & 1 \end{bmatrix}^T,\end{aligned} \tag{4.35}$$

where p_i's are the designed observer parameters, and $ad_f^i \circ S$ represents the Lie bracket operation,

$$\begin{aligned}&ad_f^0 \circ S = S, \\ &ad_f \circ S = \frac{\partial f}{\partial x} S - \frac{\partial S}{\partial x} f, \\ &ad_f^i \circ S = ad_f \circ (ad_f^{i-1} \circ S), \quad i = 2, \cdots, n.\end{aligned} \tag{4.36}$$

When applied to estimate battery SOCs under reduced voltage sensing, the extended Luenberger observer is formulated as

$$\begin{aligned}\begin{bmatrix} \dot{\hat{x}}_1 \\ \dot{\hat{x}}_2 \end{bmatrix} &= \begin{bmatrix} \frac{I}{Q} \\ \frac{I}{Q} \end{bmatrix} + L(\hat{x})(V_{str} - \hat{V}_{str}) \\ \hat{V}_{str} &= g(\hat{x}_1) + g(\hat{x}_2) + 2IR,\end{aligned} \tag{4.37}$$

with the observer gain L

$$\begin{aligned}L(\hat{x}_{str}) &= \frac{1}{\Delta} \left(p_0 \begin{bmatrix} -g'(\hat{x}_2) \\ g'(\hat{x}_1) \end{bmatrix} + \frac{p_1 I}{Q} \begin{bmatrix} g''(\hat{x}_2) \\ -g''(\hat{x}_1) \end{bmatrix} + (\frac{I}{Q})^2 \begin{bmatrix} -g'''(\hat{x}_2) \\ g'''(\hat{x}_1) \end{bmatrix} \right) \\ \Delta &= \big(g'(\hat{x}_1) g''(\hat{x}_2) - g'(\hat{x}_2) g''(\hat{x}_1) \big) \frac{I}{Q}.\end{aligned} \tag{4.38}$$

According to Eq.(4.38), the extended Luenberger observer needs to use the second and third order gradients of the voltage-SOC relationship, $g''(x)$ and $g'''(x)$. As has been mentioned for the sliding mode observer, the second order gradients of $g(x)$ are

difficult to model accurately, and will lead to significant SOC estimation errors. In the case of the extended Luenberger observer, modeling of $g'''(x)$ would be even more difficult and inaccurate, leaving the applicability of the algorithm questionable.

4.4.5 Newton Observer

The Newton observer [64, 65], which is based on the Newton-Raphson algorithm, estimates the states by simultaneously solving multiple nonlinear equations along the model output trajectory over time. Compared with the method which performs estimation based on a single data point each time, the Newton observer processes the data points collected over a certain time span simultaneously, which contains more information on the system nonlinearity.

At each estimation step, the Newton observer uses the output data over a series of consecutive time instants, $k, k+1, ...k+N$. Based on the generic discrete nonlinear system in Eq.(4.12), the output trajectory over these time instants can be derived as a function of the state at k,

$$Y_{[k,k+N]} = \begin{bmatrix} y_k \\ y_{k+1} \\ \vdots \\ y_{k+N} \end{bmatrix} = \begin{bmatrix} h(x_k) \\ h \circ f_d(x_k) \\ \vdots \\ (h \circ f_d)^N(x_k) \end{bmatrix} = H(x_k), \tag{4.39}$$

where $\circ$ represents function composition,

$$\begin{aligned} h \circ f_d(x) &= h\big(f_d(x)\big) \\ (h \circ f_d)^i(x) &= (h \circ f_d)\big((h \circ f_d)^{i-1}(x)\big), \quad i = 2, \cdots, N. \end{aligned} \tag{4.40}$$

The estimation problem is then reduced to solving Eq.(4.39) for x_k given measured output trajectory $Y_{[k,k+N]}$. The states at time instants $k+1, \cdots, k+N$ can be determined based on x_k and the model. In the Newton observer, Eq.(4.39) is solved by using the Newton-Raphson algorithm over iterations,

$$\hat{x}_k^{j+1} = \hat{x}_k^j + \left[\frac{\partial H}{\partial x_k}(\hat{x}_k^j)\right]^{-1} \big(Y_{[k,k+N]} - H(\hat{x}_k^j)\big), \tag{4.41}$$

where the superscript j denotes the jth iteration. Essentially, optimal $\hat{x}_k$ is searched here to minimize the least square error in $Y_{[k,k+N]}$. The convergence of the Newton Observer is guaranteed under observability conditions [64]. At the next estimation step, the measured voltage trajectory is updated with newly acquired data, and be-

comes $Y_{[k+W,k+W+N]}$, where W is the interval between estimation steps. The initial state at the new estimation step, x_{k+W}, will be estimated based on $Y_{[k+W,k+W+N]}$, and its initial guess is determined based on the final estimate of x_k.

For the SOC estimation problem under reduced voltage sensing, Newton observer can be formulated with the total voltage trajectory $V_{str,[k,k+N]} = H(x_{str,k})$ defined in Eq.(4.4), and $\frac{\partial H}{\partial x_{str,k}}$ in Eq.(4.5) [110]. The dimension of $\frac{\partial H}{\partial x_{str,k}}$ is $N \times 2$, where N is the number of data points along the voltage trajectory. When $N > 2$, $\frac{\partial H}{\partial x_{str,k}}$ has more rows than columns, and thus its left pseudo-inverse should be used instead,

$$(\frac{\partial H}{\partial x_{str,k}})^{-1} = \left[(\frac{\partial H}{\partial x_{str,k}})^T(\frac{\partial H}{\partial x_{str,k}})\right]^{-1}(\frac{\partial H}{\partial x_{str,k}})^T. \tag{4.42}$$

It is noted that the Newton observer can only be applied when $x_{str,k}$ is observable. The matrix $\frac{\partial H}{\partial x_{str,k}}$ is the discrete-time observability matrix, and its (pseudo)inverse exists if and only if the observability matrix is of full rank as discussed in Eq. (4.7).

The advantage of the Newton-Raphson algorithm is fast convergence, but the drawback is lack of robustness under certain circumstances. For example, when the SOCs are at the edge of the observable region, $\frac{\partial H}{\partial x_{str,k}}$ is close to rank deficient with a large condition number, posing difficulty to the inversion of $\frac{\partial H}{\partial x_{str,k}}$. To improve the robustness, the Levenberg-Marquardt iteration is used instead [114, 115],

$$\hat{x}^{j+1}_{str,k} = \hat{x}^{j}_{str,k} + \left[\frac{\partial H}{\partial x_{str,k}}(\hat{x}^{j}_{str,k}) + b\mathbf{I}\right]^{-1}\left(V_{str,[k,k+N]} - H(\hat{x}^{j}_{str,k})\right), \tag{4.43}$$

where b is a scalar, and $\mathbf{I}$ is a 2×2 identity matrix. The factor $b\mathbf{I}$ is used to lower the condition number and hence stabilize the matrix inversion.

4.4.6 Comparison of the Candidate Algorithms

Based on the previous analysis, the advantages and disadvantages of the five nonlinear observers are summarized and listed in Table 4.2. The applicable algorithms include the sliding mode observer, extended Luenberger observer and Newton observer. As for the sliding mode observer and the extended Luenberger observer, the need to use accurate high order gradients of the voltage-SOC relationship $g(x)$ poses a major obstacle for practical application. On the contrary, the Newton observer, which only uses the first gradient, will be much less affected by the modeling errors. The disadvantages of the Newton observer in data storage and computation, though, are considered as inconsequential. Experimental validation of the Newton observer

Table 4.2: Comparison of Candidate Nonlinear Observers.

Algorithms	Advantages	Disadvantages
Extended Kalman filter	-	not applicable: unobservable model after linearization
Canonical form observer	-	not applicable: complicated coordinate transformation
Sliding mode observer	data storage: single data, computation: recursive	accuracy: affected by modeling errors in $g''(x)$
Extended Luenberger observer	data storage: single data, computation: recursive	accuracy: affected by errors in $g''(x)$ and $g'''(x)$
Newton observer	accuracy: not using inaccurate high gradients	data storage: voltage trajectory, computation: iterative

will be shown in Section 4.5, where the used voltage trajectory contains 15 data points and the iteration of the Newton-Raphson algorithm is limited to 5. Such data storage scale and computation load are unlikely to be problematic for the onboard microprocessors. The Newton observer is hence chosen as the most suitable algorithm for the SOC estimation problem under reduced voltage sensing.

4.5 Experimental Validation of the Newton Observer

The validation of the Newton observer is to be shown based on experiments conducted with two 2.3 Ah $LiFePO_4$ batteries connected in series.

The coulomb counting model in Eq. (4.1) is first parameterized based on experimental data under 2 Amp constant current (CC) charging/discharging. During the validation experiment, the two cells are first initialized with SOCs around $x_{1,0} = 5\%$ and $x_{2,0} = 0\%$. They are then connected in series and charged with a single current source under 2A CC. Single cell voltages are measured to prevent overcharge and for validation. Actual cell SOCs are calculated based on current integration to validate the SOC estimation. Current is cut off when the voltage of any cell reaches the threshold of 3.6V. Measured SOCs and voltages are shown in Fig. 4.8.

The collected voltage and current data are then used for estimation and validation. The initial guess of SOCs for both cells is determined by inverting the average measured voltage. At each estimation step, $V_{str,[k,k+N]}$ contains 15 data points, which are sampled 10 seconds apart (10 s from k to $k+1$). The time interval W between each estimation step is chosen as 20 seconds. In this way, SOC estimation is updated every 20 seconds, corresponding to an SOC increment of 0.5%. This rate is sufficient for preventing overcharge in real time.

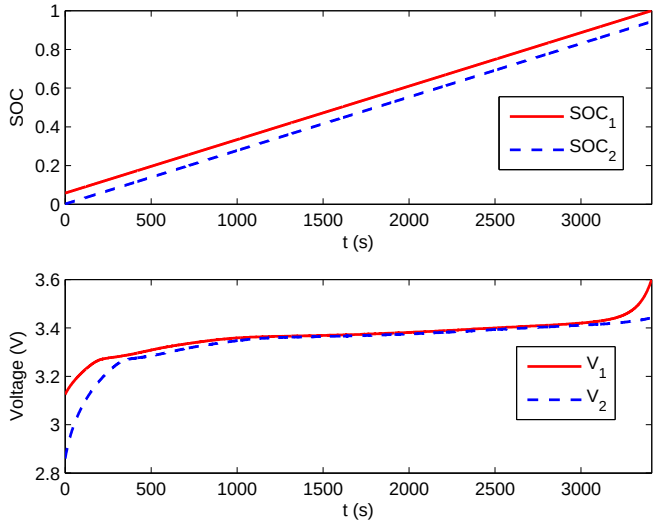

Figure 4.8: Measured SOCs and Voltages of Individual Cells under 5% SOC Imbalance.

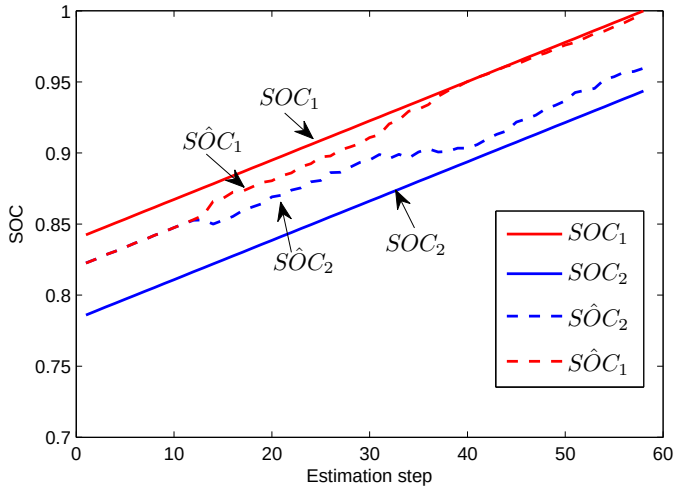

Figure 4.9: Comparison of SOC Estimation with Experiment Measurement under 5% SOC Imbalance.

The estimates of the Newton observer are shown and compared with the measurements in Fig. 4.9 and Fig. 4.10. The plotted values correspond to the last point at each estimation step. The final estimates are listed in Table 4.3. In Fig. 4.9, it can be seen that the single cell SOCs are not distinguishable when both SOCs are below 85%. This observation is in accordance with the observability analysis in Section 4.3, which predicts that the SOCs are not observable in the middle SOC range due to the nearly linear voltage vs. SOC relationship $g(x)$. As the SOCs evolve to the observable

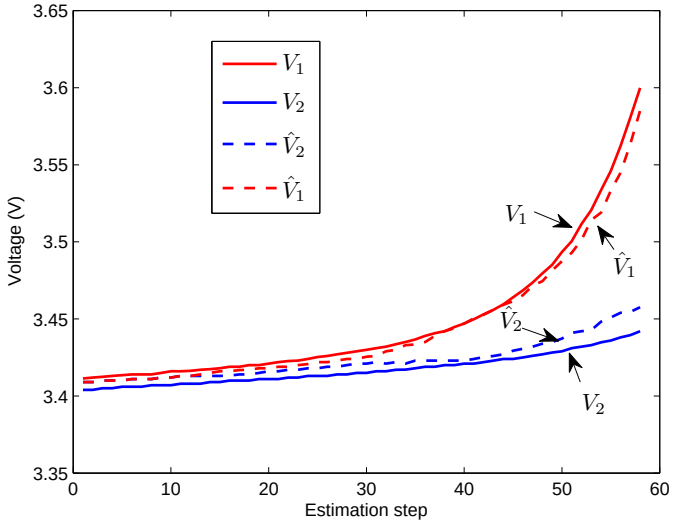

Figure 4.10: Comparison of Voltage Estimation with Experiment Measurement under 5% SOC Imbalance.

Table 4.3: Final Estimates under 5% SOC Imbalance.

	Estimates	Measurement	error (%)
SOC_1 (%)	99.81	100	0.19
SOC_2 (%)	95.99	94.36	1.73
V_1 (V)	3.59	3.60	0.28
V_2 (V)	3.46	3.44	0.58

range above 90%, the estimates of the Newton Observer converge to the measurement gradually. Furthermore, it is noted that the estimate of SOC_1 is more accurate than that of SOC_2. This feature is advantageous for preventing overcharge because cell 1 is closer to being fully charged and hence the precaution is more critical. The reason for the better accuracy of SOC_1 estimation is due to the higher sensitivity of V_{str} to SOC_1, caused by the larger $g'(x)$ at x_1.

4.6 Conclusions

This chapter is devoted to investigating the possibility of correctly estimating individual cell SOCs with only the total voltage measurement for cells in series connection. It is pointed out that the existence of the solution relies on the observability of the nonlinear battery string model. For battery chemistries with linear polarization curves, the individual cell SOCs are not observable when only the total string voltage is measured. However, for $LiFePO_4$/graphite batteries, the observability condition

can be satisfied in high and low SOC ranges, where the polarization curve is featured by monotonically increasing derivatives.

A nonlinear observer based on the Levenberg-Marquardt algorithm is then designed to estimate the individual cell SOCs and voltages. The algorithm has been implemented to a $LiFePO_4$/graphite battery string with 2 cells. As indicated by the observability analysis, the estimated SOC converge faster and are much more accurate at high and low SOC ends (than in the middle range), where the SOC estimation is more critical. In principle, the methodology can be extended to cell strings with more cells and cells of other chemistries given proper polarization curves.

CHAPTER V

Estimating Individual Cell Capacities under Reduced Voltage Sensing

5.1 Introduction

For cells in a battery pack, besides SOC imbalance, difference in capacity may also exist among cells [108, 116], which will in turn lead to SOC imbalance. The causes for capacity imbalance may include manufacturing variability, which results in different contents of active material [93], and varying capacity fading rates due to operating conditions [82]. In Chapter IV, the SOCs of the two-cell string are estimated by assuming that the capacity of the two cells are equal and known. In this chapter, the estimation problem will be studied under unknown and imbalanced capacities.

First, the robustness of the SOC estimation algorithm developed in Chapter IV is investigated under (unknown) capacity imbalance. The SOC estimation error is first derived under uncertainty in capacity and resistance, where the sensitivity matrix of SOC estimation is introduced. The singular values of the sensitivity matrix are calculated for different combinations of SOC and capacity imbalance. It will be shown that certain combinations lead to small singular values, indicating poor robustness of the estimation under uncertainty in battery capacity. The imbalance and uncertainty in resistance is also considered, which does not affect the sensitivity matrix though.

Second, an algorithm is designed to estimate the capacity imbalance in the battery string. Since the capacity and SOC cannot be determined independently, both of them need to be estimated in the proposed method. In literature, estimation of battery capacity and SOC has been studied extensively under full voltage sensing (when single-cell voltage is measured). The most commonly used method is the extended Kalman filtering. For example, dual extended Kalman filtering (DEKF) [117] has been used to estimate the battery SOC and capacity in a sequential way, which

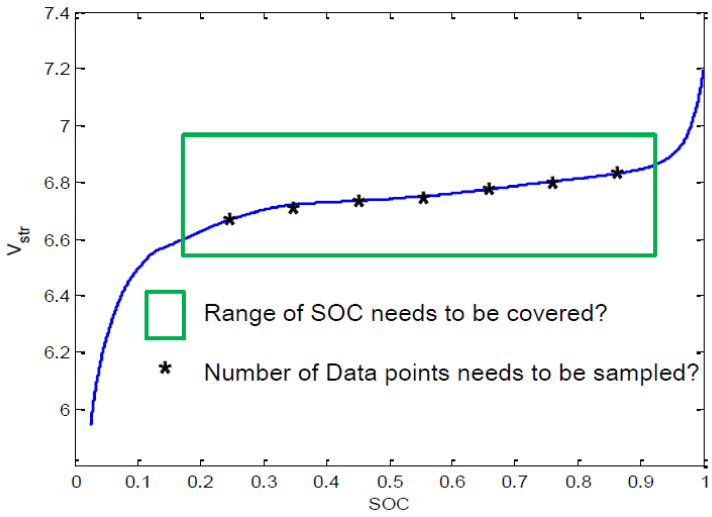

Figure 5.1: Data Collection Strategy for SOC and Capacity Joint Estimation.

includes the synchronized (standard) DEKF [60, 118, 119] and the multi-scale DEFK where the SOC and capacity are updated at different rates [120, 121]. Joint extended Kalman filter (JEKF) has also been applied, which updates the SOC and capacity estimation simultaneously [122, 123]. When the SOC is directly available, linear least squares algorithm can also be used for capacity estimation [124]. Other methods include the dual/joint sigma-point Kalman filtering [125] and particle filtering [87]. In this chapter, estimation of SOCs and capacities of the two cells is studied under reduced voltage sensing. As has been mentioned, because the linearized battery model is not observable, the linearization-based method, such as the extended Kalman filter, can not be used for estimation. Therefore, the nonlinear estimation algorithm that has been used for SOC estimation in Chapter IV, the Newton-Raphson method, is augmented for joint estimation of SOC and capacity.

Furthermore, the data collection strategy is also studied in order to achieve certain estimation accuracy under measurement noises. The data collection strategy includes i) what is the SOC variation and ii) how many number of data points that need to be covered in the voltage trajectory, as shown in Fig. 5.1. The quantitative relationship between the variance of parameter estimation and measurement noises under different SOC variation and number of data points is established based on Cramer-Rao bound analysis to guide the selection of data collection strategy. To sum up the discussion in Chapter IV and Chapter V, the overall estimation scheme, consisting of the real-time SOC estimation and off-line capacity adaptation, will be discussed in the end.

5.2 Robustness of SOC Estimation under Imbalance and Uncertainty in Capacity and Resistance

In Chapter IV, the SOC estimation is conducted by assuming known and equal capacity and resistance between cells, and the nominal capacity and resistance are used in the Newton observer for estimation. When the (unknown) imbalance in capacity and resistance exists, uncertainty is introduced to the modeled capacity and resistance. The impact of the model uncertainty in capacity and resistance on the accuracy of SOC estimation will be analyzed in this section.

5.2.1 State of Charge Estimation Error under Model Uncertainty in Capacity and Resistance

In this subsection, the SOC estimation error under uncertainty in capacity and resistance will be derived. The sensitivity matrix of SOC estimation is obtained during the procedures. The results will be used for robustness analysis in the following subsection.

When the capacity and resistance are not equal between the two cells, the true voltage trajectory $V^*_{str,[k,k+N]}$ can be derived as

$$V^*_{str,[k,k+N]} = H(x^*_{str,k}, Q^*, R^*) = \begin{bmatrix} g(x^*_{1,k}) + g(x^*_{2,k}) \\ g\big(x^*_{1,k} + \frac{I\Delta t}{Q^*_1}\big) + g\big(x^*_{2,k} + \frac{I\Delta t}{Q^*_2}\big) \\ \cdots \\ g\big(x^*_{1,k} + \frac{NI\Delta t}{Q^*_1}\big) + g\big(x^*_{2,k} + \frac{NI\Delta t}{Q^*_2}\big) \end{bmatrix} + I(R^*_1 + R^*_2),$$
$$Q^* = \begin{bmatrix} Q^*_1 \\ Q^*_2 \end{bmatrix}, \quad R^* = \begin{bmatrix} R^*_1 \\ R^*_2 \end{bmatrix}, \tag{5.1}$$

where the superscript * denotes the true value of the variable, $x_{str,k} = \begin{bmatrix} x_{1,k} & x_{2,k} \end{bmatrix}^T$ are the SOCs of the two cells, and Q and R are capacity and resistance.

In the Newton observer designed in Chapter IV, the capacity and resistance of both cells are assumed to be the rated values Q_0 and R_0. Modeling errors, δQ and δR, and estimation error in SOC, $e_{x,k}$, are defined as the difference between the true

values and the assumed/estimated values,

$$\begin{aligned}
\delta Q &= \begin{bmatrix} \delta Q_1 \\ \delta Q_2 \end{bmatrix} = \begin{bmatrix} Q_1^* - Q_0 \\ Q_2^* - Q_0 \end{bmatrix} \\
\delta R &= \begin{bmatrix} \delta R_1 \\ \delta R_2 \end{bmatrix} = \begin{bmatrix} R_1^* - R_0 \\ R_2^* - R_0 \end{bmatrix} \\
e_{x,k} &= x_{str,k}^* - \hat{x}_{str,k} = \begin{bmatrix} x_{1,k}^* - \hat{x}_{1,k} \\ x_{2,k}^* - \hat{x}_{2,k} \end{bmatrix}.
\end{aligned} \tag{5.2}$$

Based on Eq.(5.1), variation of $V_{str,[k,k+N]}$ under (small) deviation of $x_{str,k}$, Q and R can be obtained as,

$$\delta V_{str,[k,k+N]} = \frac{\partial H}{\partial x_{str,k}} \delta x_{str,k} + \frac{\partial H}{\partial Q} \delta Q + \frac{\partial H}{\partial R} \delta R, \tag{5.3}$$

where $\frac{\partial H}{\partial x_{str,k}}$ is the sensitivity matrix for SOC estimation,

$$S_x(x_{str,k}^*) = \frac{\partial H}{\partial x_{str,k}}(x_{str,k}^*, Q^*) = \begin{bmatrix} g'(x_{1,k}^*) & g'(x_{2,k}^*) \\ g'\big(x_{1,k}^* + \frac{I\Delta t}{Q_1^*}\big) & g'\big(x_{2,k}^* + \frac{I\Delta t}{Q_2^*}\big) \\ \cdots & \cdots \\ g'\big(x_{1,k}^* + \frac{NI\Delta t}{Q_1^*}\big) & g'\big(x_{2,k}^* + \frac{NI\Delta t}{Q_2^*}\big) \end{bmatrix} \tag{5.4}$$

and

$$\begin{aligned}
\frac{\partial H}{\partial Q} &= \begin{bmatrix} 0 & 0 \\ -g'\big(x_{1,k}^* + \frac{I\Delta t}{Q_1^*}\big)\frac{I\Delta t}{(Q_1^*)^2} & -g'\big(x_{2,k}^* + \frac{I\Delta t}{Q_2^*}\big)\frac{I\Delta t}{(Q_2^*)^2} \\ \cdots & \cdots \\ -g'\big(x_{1,k}^* + \frac{NI\Delta t}{Q_1^*}\big)\frac{NI\Delta t}{(Q_1^*)^2} & -g'\big(x_{2,k}^* + \frac{NI\Delta t}{Q_2^*}\big)\frac{NI\Delta t}{(Q_2^*)^2} \end{bmatrix}, \\
\frac{\partial H}{\partial R} &= \begin{bmatrix} I & I \\ I & I \\ \cdots & \cdots \\ I & I \end{bmatrix}.
\end{aligned} \tag{5.5}$$

By taking δQ and δR as the modeling uncertainty, $\delta x_{str,k}$ represents the resulting SOC estimation error $e_{x,k}$, and $\delta V_{str,[k,k+N]}$is the mismatch between the measured and the estimated voltage trajectory. Since the Newton observer estimates $\hat{x}_{str,k}$ by minimizing the least square error in voltage, $\delta V_{str,[k,k+N]}$ is usually small. Based on

Eq.(5.3), with $e_{x,k} = \delta x_{str,k}$, the SOC estimation error $e_{x,k}$ can be quantified as

$$e_{x,k} = \big(S_x(x^*_{str,k}, Q^*)\big)^{-1}\big[\delta V_{str,[k,k+N]} - \frac{\partial H}{\partial Q}(x^*_{str,k}, Q^*)\delta Q - \frac{\partial H}{\partial R}\delta R\big]. \tag{5.6}$$

For the convenience of comparison, Eq. (5.6) needs to be normalized to the form of percentage error, as

$$e_{x,k,\%} = \big(\overline{S}_x(x^*_{str,k}, Q^*)\big)^{-1}\big(\delta V_{str,[k,k+N],\%} - \frac{\overline{\partial H}}{\partial Q}\delta Q_\% - \frac{\overline{\partial H}}{\partial R}\delta R_\%\big), \tag{5.7}$$

where

$$\begin{aligned} e_{x,k,\%} &= \begin{bmatrix} \frac{x^*_{1,k} - \hat{x}_{1,k}}{x^*_{1,k}} \\ \frac{x^*_{2,k} - \hat{x}_{2,k}}{x^*_{2,k}} \end{bmatrix}, \\ \delta Q_\% = \begin{bmatrix} \frac{Q^*_1 - Q_0}{Q^*_1} \\ \frac{Q^*_2 - Q_0}{Q^*_2} \end{bmatrix}, &\quad \delta R_\% = \begin{bmatrix} \frac{R^*_1 - R_0}{R^*_1} \\ \frac{R^*_2 - R_0}{R^*_2} \end{bmatrix}. \end{aligned} \tag{5.8}$$

The matrices $\overline{S}_x$, $\frac{\overline{\partial H}}{\partial Q}$ $\frac{\overline{\partial H}}{\partial R}$, and $\delta V_{str,[k,k+N],\%}$ are normalized as

$$\begin{aligned} \big[\overline{S_x}\big]_{j,l} &= \big[\frac{\partial H}{\partial x_{str,k}}\big]_{j,l}\frac{x^*_{l,k}}{V^*_{str,k+j-1}}, \\ \big[\frac{\overline{\partial H}}{\partial Q}\big]_{j,l} &= \big[\frac{\partial H}{\partial Q}\big]_{j,l}\frac{Q^*_l}{V^*_{str,k+j-1}}, \\ \big[\frac{\overline{\partial H}}{\partial R}\big]_{j,l} &= \big[\frac{\partial H}{\partial R}\big]_{j,l}\frac{R^*_l}{V^*_{str,k+j-1}}, \\ \big[\delta V_{str,[k,k+N],\%}\big]_j &= \frac{\delta V_{str,k+j-1}}{V^*_{str,k+j-1}}, \end{aligned} \tag{5.9}$$

where $[\cdot]_{j,l}$ denotes the matrix entry, (j for row index and l for column index).

5.2.2 Robustness of SOC Estimation under Different Combinations of SOC and Capacity Imbalance

The normalized sensitivity matrix $\overline{S}_x$ and the derived SOC estimation error under capacity and resistance uncertainty in Eq.(5.8) are used to analyzed the robustness of SOC estimation in this subsection. It will be shown that the robustness is poor under certain combinations of SOC and capacity imbalance.

The sensitivity matrix S_x is studied first, whose singular values indicate the ro-

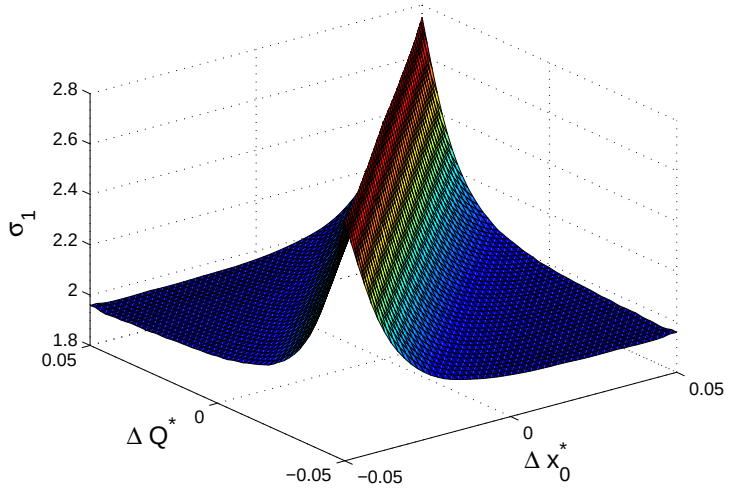

Figure 5.2: Singular Value σ_1 of the sensitivity matrix S at the End of Charging.

bustness of the estimation problem [85, 126]. In the presence of model uncertainty, according to Eq.(5.8) where S_x is inverted, the larger the singular values are, the smaller the estimation error $e_{x,k}$ would be. According to Eq.(5.4), S_x is dependent on SOC $x^*_{str,k}$ and capacity Q^*, but not on resistance R^*. Since SOC estimation is a non-linear estimation problem, sensitivity needs to be discussed for different combinations of $x^*_{str,k}$ and Q^*. The capacities Q^*_1 and Q^*_2 are considered as varying between 100% and 95% of the rated capacity Q_0. Under capacity imbalance, the SOC imbalance will not be constant during battery operation. Therefore, reference SOCs, $x^*_{1,0}$ and $x^*_{2,0}$, are defined around 0%, which vary from 0%-5% respectively. The resulting imbalance in reference SOC and capacity,

$$\Delta x^*_0 = x^*_{1,0} - x^*_{2,0}, \quad \Delta Q^*_{\%} = \frac{Q^*_1 - Q^*_2}{Q_0}, \tag{5.10}$$

will both vary between -5% and $+5\%$. The singular values of $\overline{S}_x$, σ_1 and σ_2, are calculated at the last estimation step (the end of charging) for all the combinations, as shown in Fig. 5.2 and Fig. 5.3.

The smaller singular value σ_2 is the critical one that determines the robustness of estimation. As seen in Fig. 5.3, the values of σ_2 for most combinations are above 0.03, except those on the diagonal of the $\Delta x^*_0 - \Delta Q^*$ plane. These combinations lead to unrobust estimation of SOCs, with condition numbers of S_x $\kappa \geq 99$ as compared to $\kappa < 50$ elsewhere. The existence of these combinations can be deduced from the structure of S_x in Eq.(5.4). If the SOCs of the two cells, at the end of charging, are

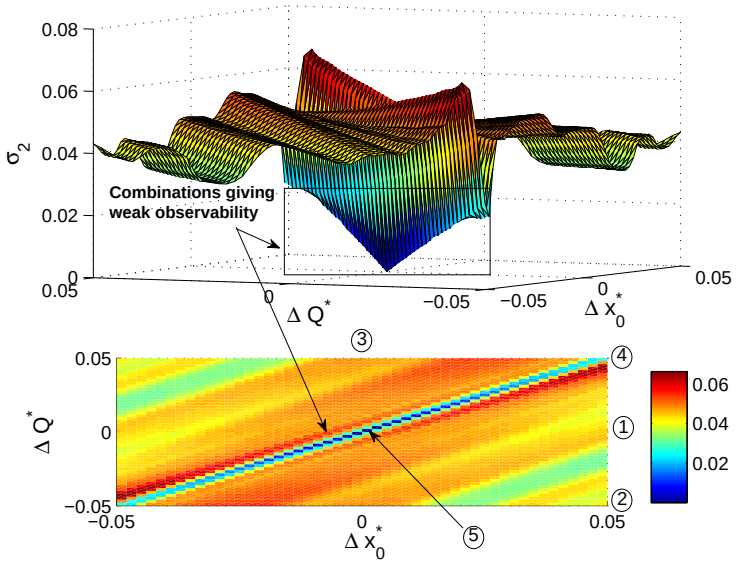

Figure 5.3: Singular Value σ_2 of the sensitivity matrix S at the End of Charging (upper plot: values of σ_2 for all combinations; bottom plot: projection of σ_2 onto the $\Delta x_0^* - \Delta Q^*$ plane).

close to each other, the two columns of S_x will be nearly identical, leading to large condition number of S_x. Such cases can be represented as

$$\begin{aligned} & x_{1,0}^* + \frac{\int Idt}{Q_1^*} \approx x_{2,0}^* + \frac{\int Idt}{Q_2^*} \\ \Rightarrow \quad & x_{1,0}^* - x_{2,0}^* \approx \frac{\int Idt}{Q_1^*} \frac{Q_1^* - Q_2^*}{Q_2^*}, \end{aligned} \tag{5.11}$$

where $\int Idt$ is the change in stored energy (in amp hour) from the reference point to the end of charging. When the capacity imbalance is within $\pm 5\%$, we have $Q_1^* \approx Q_2^* \approx Q_0$, giving

$$x_{1,0}^* - x_{2,0}^* \approx \frac{\int Idt}{Q_0} \frac{Q_1^* - Q_2^*}{Q_0} \Rightarrow \Delta x_0^* \approx \frac{\int Idt}{Q_0} \Delta Q_{\%}^*. \tag{5.12}$$

Since $\int Idt$ is close to the rated capacity Q_0 from the reference point (around 0% SOC) to the end of charging (near 100% SOC), Eq.(5.12) yields

$$\Delta x_0^* \approx \Delta Q_{\%}^*. \tag{5.13}$$

Consequently, the weakly robust combinations lie along the diagonal of the $\Delta x_0^* - \Delta Q^*$ plane.

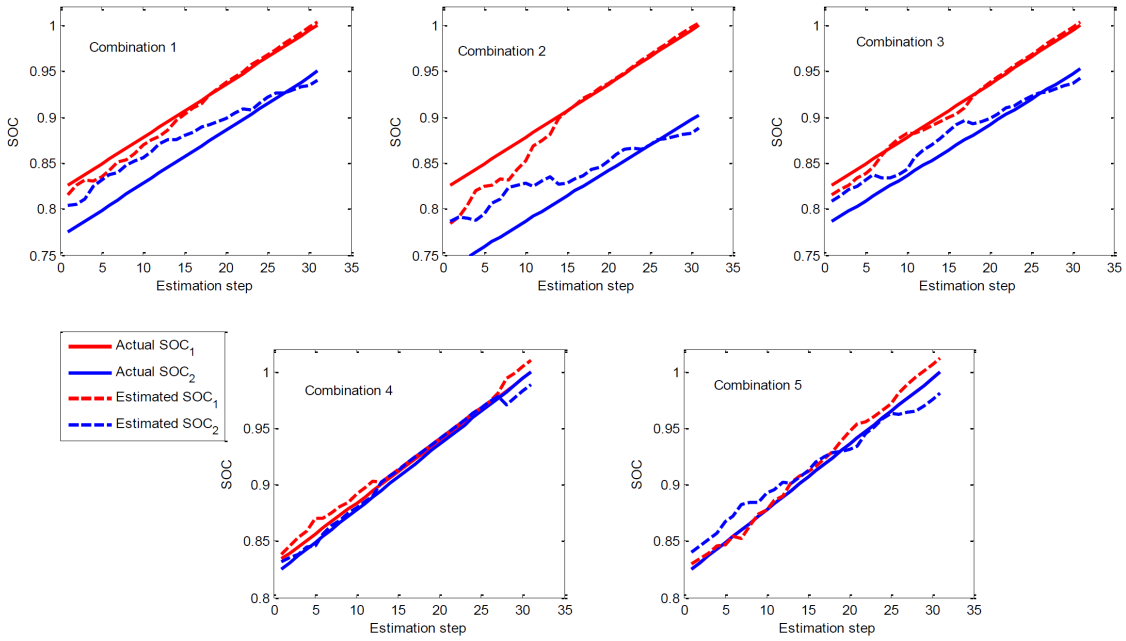

Figure 5.4: Simulated SOC Estimation under 5 Combinations of SOC Imbalance and Degradation.

To quantify the impact of robustness, the SOC estimation errors under some combinations of SOC and capacity/resistance imbalance is to be discussed as examples. Five combinations are considered, which locate at the labeled spots ①-⑤ on the $\Delta x_0^* - \Delta Q^*$ plane in Fig. 5.3. The specifications of these combinations are listed in Table 5.1. The imbalance in capacity and resistance is assumed to be caused by differing degree of battery degradation, and the percentage of capacity fade is projected to be the same as that of resistance growth. The singular values and condition number of the sensitivity matrix, as well as the predicted estimation errors based on Eq.(5.7) are listed in Table 5.1. Combinations ①-③ are in the strongly robust region, with singular value $\sigma_2 > 0.04$ and condition number $\kappa \leq 50$. Combinations ④ and ⑤, lying on the diagonal of the $\Delta x_0^* - \Delta Q^*$ plane, are weakly robust with $\sigma_2 < 0.03$ and condition number $\kappa \geq 99$. The SOC estimation of the Newton observer for these combinations is simulated and shown in Fig. 5.4. It can be seen that the SOC estimation of combinations ①-③ is not greatly affected by the model uncertainty, especially for the critical cell 1, which is fully charged at the end. The SOC estimation errors seen in simulation are close to the predicted errors based on Eq.(5.7). For combinations ④ and ⑤, the SOCs of the two cells are almost the same at the end of charging, yielding weak robustness and hence larger estimation errors. In case ⑤

especially, because the SOCs of the two cells are identical, one of the singular values of S_x is zero, resulting in infinite theoretical SOC estimation errors under capacity uncertainty. However, the errors seen in simulation are not unbounded (only -1.25% for cell 1 and 1.91% for cell 2). The reason is that the designed Newton observer uses the Levenberg-Marquardt iteration in Eq.(4.43) for SOC estimation. In the original Newton observer (Eq.(4.41)), the Jacobian matrix $\frac{\partial H}{\partial x_{str,k}}(\hat{x}^j_{str,k})$ needs to be inverted during the computation process. It is noted that the Jacobian matrix takes the same form as the sensitivity matrix S_x, except that the estimated $x_{str,k}$ is used in place of the actual SOCs. Therefore, the estimation could not be performed for case ⑤ (equivalent to infinite estimation error) because the Jacobian matrix is not invertible. When the Levenberg-Marquardt iteration is applied, a factor $b\mathbf{I}$ is added to the Jacobian matrix to make the matrix inversion feasible, and thus prevent the estimation errors from being unbounded.

Table 5.1: Robustness of SOC Estimation under Certain Combinations of Imbalance and Degradation.

No.	Initial SOC	Degradation	Q^*	R^*	σ	κ	Predicted $e_{x,\%}$	Simulated $e_{x,\%}$
①	$x_{1,0} = 5\%$	Cell1: 5%	$Q_1^* = 0.95Q_0$	$R_1^* = 1.05R_0$	1.95	44	$e_{x,1,\%} = -0.40\%$	$e_{x,1,\%} = -0.38\%$
	$x_{2,0} = 0\%$	Cell2: 5%	$Q_2^* = 0.95Q_0$	$R_2^* = 1.05R_0$	0.045		$e_{x,2,\%} = 1.10\%$	$e_{x,2,\%} = 1.03\%$
②	$x_{1,0} = 5\%$	Cell1: 5%	$Q_1^* = 0.95Q_0$	$R_1^* = 1.05R_0$	1.94	45	$e_{x,1,\%} = -0.3\%$	$e_{x,1,\%} = -0.27\%$
	$x_{2,0} = 0\%$	Cell2: 0%	$Q_2^* = Q_0$	$R_2^* = R$	0.043		$e_{x,2,\%} = 1.57\%$	$e_{x,2,\%} = 1.51\%$
③	$x_{1,0} = 5\%$	Cell1: 0%	$Q_1^* = Q$	$R_1^* = R$	1.95	41	$e_{x,1,\%} = -0.38\%$	$e_{x,1,\%} = -0.40\%$
	$x_{2,0} = 5\%$	Cell2: 5%	$Q_2^* = 0.95Q$	$R_2^* = 1.05R$	0.048		$e_{x,2,\%} = 1.07\%$	$e_{x,2,\%} = 1.30\%$
④	$x_{1,0} = 5\%$	Cell1: 0%	$Q_1^* = Q$	$R_1^* = R$	2.72	99	$e_{x,1,\%} = -1.84\%$	$e_{x,1,\%} = -1.05\%$
	$x_{2,0} = 0\%$	Cell2: 5%	$Q_2^* = 0.95Q$	$R_2^* = 1.05R$	0.028		$e_{x,2,\%} = 2.08\%$	$e_{x,2,\%} = 1.11\%$
⑤	$x_{1,0} = 5\%$	Cell1: 5%	$Q_1^* = 0.95Q$	$R_1^* = 1.05R$	2.69	∞	$e_{x,1,\%} = \infty$	$e_{x,1,\%} = -1.25\%$
	$x_{2,0} = 5\%$	Cell2: 5%	$Q_2^* = 0.95Q$	$R_2^* = 1.05R$	0		$e_{x,2,\%} = \infty$	$e_{x,2,\%} = 1.91\%$

5.3 Joint Estimation of Cell SOCs and Capacities

It has been shown that the SOC estimation will not be robust under all combinations of SOC and capacity imbalance. Although the Levenberg-Marquardt iteration can be used to improve the robustness, it cannot eradicate the impact of uncertainty in battery capacity. Capacity estimation is highly desirable due to three reasons. First, with correct capacity values, SOC estimation by the Newton observer will be more accurate under all combinations in the high SOC range. Second, in the middle SOC range where the cell SOCs are not observable from the string voltage, the open-loop SOC estimation can still be applied based on coulomb counting, and its accuracy can be improved with correct capacity. In addition, monitoring capacity fade is an important aspect of evaluating battery state of health (SOH) [127, 128].

In this section, the capacities of the two-cell string will be estimated jointly with SOCs under reduced voltage sensing. Based on the Cramer-Rao bound analysis, it is shown that the voltage trajectory required for accurate joint estimation of SOCs and capacities needs to cover a wide range of SOC variation and include large number of data points. The Newton-Raphson method is then applied for estimation, where singular value decomposition of the Jacobian matrix is used to enhance the robustness of estimation. The overall estimation scheme, which includes the real-time SOC estimation and off-line joint estimation of SOCs and capacities, will also be discussed.

5.3.1 Determination of Data Collection Strategy based on Cramer-Rao Bound

Like SOC estimation, the joint estimation of capacity and SOC will be based on the trajectory of the total voltage over multiple time instants. The procedures of calculating the Cramer-Rao bound of SOC and capacity estimation based on the voltage trajectory is to be introduced first. It will then be used to determine the SOC variation and number of data points that are needed in a voltage trajectory to achieve certain accuracy of estimation.

The first step is to write the total voltage trajectory (under constant charging

current) as a function of capacities and SOCs,

$$V_{str,[k,k+N]} = H(x_{str,k+N}, Q) = \begin{bmatrix} g\big(x_{1,k+N} - \frac{NI\Delta t}{Q_1}\big) + g\big(x_{2,k+N} - \frac{NI\Delta t}{Q_2}\big) \\ \cdots \\ g\big(x_{1,k+N} - \frac{I\Delta t}{Q_1}\big) + g\big(x_{2,k+N} - \frac{I\Delta t}{Q_2}\big) \\ g(x_{1,k+N}) + g(x_{2,k+N}) \end{bmatrix} + I(R_1 + R_2). \tag{5.14}$$

It is noted that the SOC variable is chosen as $x_{str,k+N}$, which is the SOC when the batteries are close to being fully charged. This is because SOC estimation is most critical at high end to prevent overcharge, and thus the variance of SOC estimation at that point is of most interest. Based on Eq.(5.14), the sensitivity matrix of the voltage trajectory to SOCs and capacities can be obtained as

$$\frac{\partial H}{\partial(x_{str,k+N}, Q)} = \begin{bmatrix} g'\big(x_{1,k+N} - \frac{NI\Delta t}{Q_1}\big) & g'\big(x_{2,k+N} - \frac{NI\Delta t}{Q_2}\big) & g'\big(x_{1,k+N} - \frac{NI\Delta t}{Q_1}\big)\frac{NI\Delta t}{(Q_1)^2} & g'\big(x_{2,k+N} - \frac{NI\Delta t}{Q_2}\big)\frac{NI\Delta t}{(Q_2)^2} \\ \cdots & \cdots & \cdots & \cdots \\ g'\big(x_{1,k+N} - \frac{I\Delta t}{Q_1}\big) & g'\big(x_{2,k+N} - \frac{I\Delta t}{Q_2}\big) & g'\big(x_{1,k+N} - \frac{I\Delta t}{Q_1}\big)\frac{I\Delta t}{(Q_1)^2} & g'\big(x_{2,k+N} + \frac{I\Delta t}{Q_2}\big)\frac{I\Delta t}{(Q_2)^2} \\ g'(x_{1,k+N}) & g'(x_{2,k+N}) & 0 & 0 \end{bmatrix}. \tag{5.15}$$

If the variance of voltage measurement noises is σ_V^2, the Fisher information matrix [85] of the voltage trajectory is

$$F_{info} = \left(\frac{\partial H}{\partial(x_{str,k+N}, Q)}\right)^T \begin{bmatrix} \frac{1}{\sigma_V^2} & & \\ & \cdots & \\ & & \frac{1}{\sigma_V^2} \end{bmatrix} \frac{\partial H}{\partial(x_{str,k+N}, Q)}. \tag{5.16}$$

The Cramer-Rao bound can be obtained as

$$cov(\hat{x}_{str,k+N}, \hat{Q}) \geq F_{info}^{-1}, \tag{5.17}$$

which provides the lower bound on the covariance of the SOC and capacity estimation. Specifically, the diagonal elements of the 4×4 F_{info}^{-1} matrix represent the lower bound

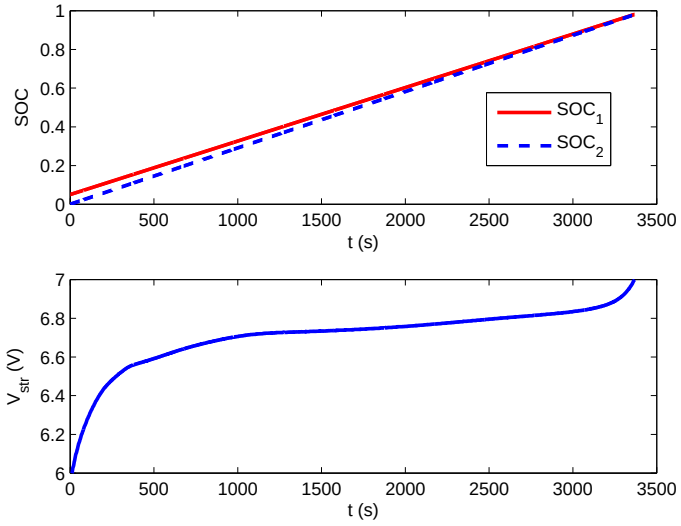

Figure 5.5: Evolution of cell SOCs under constant charging current of 1 C when $x_{1,0} = 0.05 \quad x_{2,0} = 0, \quad Q_1 = Q_0, \quad Q_2 = 0.95Q_0$.

on the variance of the 4 variables to be estimated,

$$\begin{aligned} \sigma^2_{CR} &= \left[\sigma^2_{CR}(x_{1,k+N}), \quad \sigma^2_{CR}(x_{2,k+N}), \quad \sigma^2_{CR}(Q_1), \quad \sigma^2_{CR}(Q_2)\right]^T = diag(F^{-1}_{info}), \\ &\sigma_{est}(\hat{\theta}) \geq \sigma_{CR}(\theta), \quad \forall \theta = x_{1,k+N}, x_{2,k+N}, Q_1, Q_2, \end{aligned} \tag{5.18}$$

where σ_{CR} stands for the standard deviation specified by the Cramer-Rao bound, and σ_{est} is the standard deviation of the estimation.

The Cramer-Rao bound can be used to evaluate the sufficiency of the dataset to achieve a certain level of estimation accuracy. For joint estimation of individual cell SOCs and capacities, the Cramer-Rao bound is shown to be highly dependent on the SOC variation covered by and the number of data points contained in the voltage trajectory, which correspond to the terms $\frac{NI\Delta t}{Q}$ and N in Eq.(5.14) respectively. Consider the case

$$x_{1,0} = 0.05 \quad x_{2,0} = 0, \quad Q_1 = Q_0, \quad Q_2 = 0.95Q_0 \tag{5.19}$$

as an example. Under constant charging current of 1 C, the SOC evolution of the two cells is shown in Fig. 5.5. The relationship between the normalized σ_{CR},

$$\sigma_{CR,\%}(Q_i) = \frac{\sigma_{CR}(Q_i)}{Q_i}, \quad \sigma_{CR,\%}(x_{i,k+N}) = \frac{\sigma_{CR}(x_{i,k+N})}{x_{i,k+N}}, \quad i = 1, 2 \tag{5.20}$$

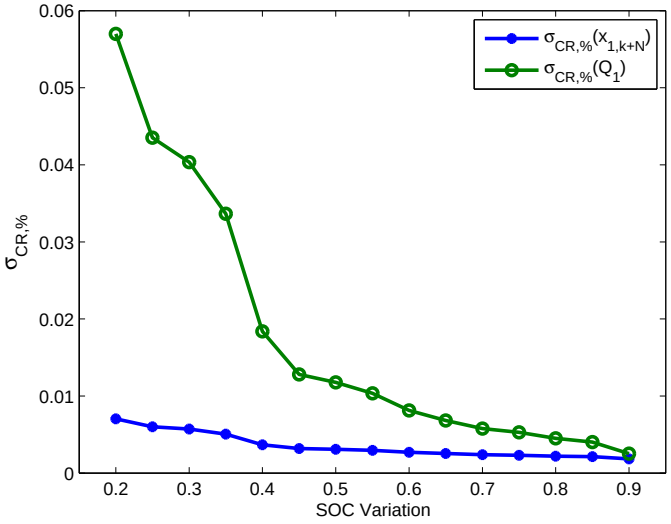

Figure 5.6: $\sigma_{CR,\%}$ of capacity and SOC estimation versus SOC variation covered by the voltage trajectory (for the case $x_{1,0} = 0.05 \quad x_{2,0} = 0, \quad Q_1 = Q_0, \quad Q_2 = 0.95Q_0$).

and the SOC variation of the voltage trajectory is plotted in Fig. 5.6. The standard deviation of the voltage measurement noises is set as 3 mV and the sampling period is 1 s. The end-points of different voltage trajectories are fixed at $t = 3368s$, where the SOCs of both cells are at 98%. The starting points vary from $t = 344s$ to $t = 2750s$, corresponding to initial SOCs of 10% and 80%. Hence the SOC variation represented in the x-axis in Fig. 5.6 ranges from 20% to 90%. The reason of considering different voltage trajectories in this way is that the batteries in PHEVs and BEVs are usually charged to nearly 100% during overnight charging, but they are not necessarily discharged to the same low point in daily usage. Only the Cramer-Rao bounds of x_1 and Q_1 are shown in Fig. 5.6, since those of x_2 and Q_2 are similar. It can be seen that the standard deviation of the capacity estimation is greatly affected by the SOC variation of the voltage trajectory. The accuracy of capacity estimation is improved (with small standard deviation) under large SOC variation. The standard deviation of estimation is also dependent on the number of data points contained in the voltage trajectory (sampling rate of voltage measurement). In Fig 5.7, values of $\sigma_{CR_\%}$ are plotted for voltage trajectories which cover the same SOC variation (80%) but with different number of data points. The x-axis at the bottom denotes the number of data points contained in the voltage trajectory (N in Eq. (5.14)), and the x-axis at the top represents the corresponding sampling rate ($1/\Delta t$ in Eq. (5.14)). It is noted that good estimation accuracy needs to be achieved with large number of data points.

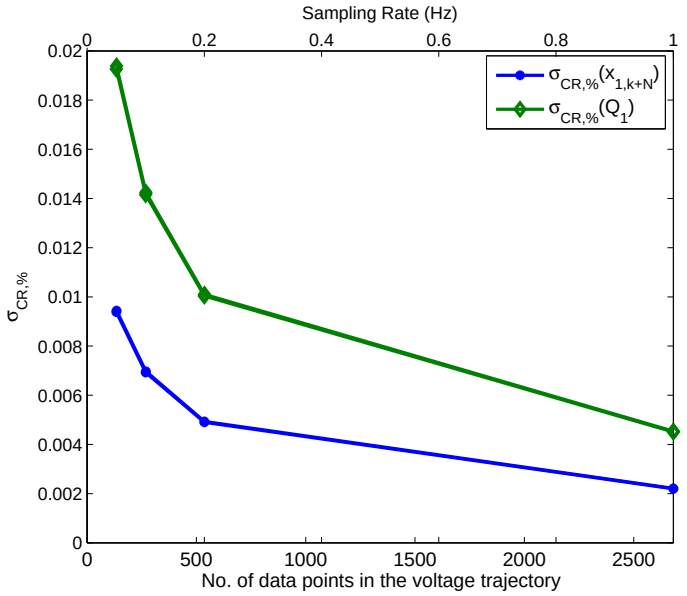

Figure 5.7: $\sigma_{CR,\%}$ of capacity and SOC estimation versus number of data points in the voltage trajectory (for the case $x_{1,0} = 0.05 \quad x_{2,0} = 0, \quad Q_1 = Q, \quad Q_2 = 0.95Q$).

For onboard estimation of SOC and capacity, the data collection strategy, including selection of SOC variation and number of data points in the voltage trajectory, needs to satisfy required estimation accuracy under all possible combinations of SOC and capacity imbalance. Here, a range of combinations of SOC and capacity is considered,

$$\begin{aligned} &x_{1,0} = 0.05, \quad Q_1 = 0.95Q_0, \\ &x_{2,0} \in [0, 0.1], \quad Q_2 \in [0.9Q_0, Q_0]. \end{aligned} \tag{5.21}$$

corresponding to SOC and capacity imbalance of

$$\begin{aligned} &\Delta x_0 = x_{1,0} - x_{2,0} \in [-0.05, 0.05], \\ &\Delta x_{k+N} = x_{1,k+N} - x_{2,k+N} \in [-0.1, 0.1], \\ &\Delta Q_{\%} = \frac{Q_1 - Q_2}{Q_0} \in [-0.05, 0.05], \end{aligned} \tag{5.22}$$

where x_{k+N} is the SOC at the high end when the batteries are charged. As an example, the values of $\sigma_{CR,\%}(x_{1,k+N})$ and $\sigma_{CR,\%}(Q_1)$ for all the considered combinations under SOC variation range of 90% and sampling rate of 0.2 Hz are shown in Fig. 5.8 and Fig. 5.9. It is noted that the estimation accuracy is poor (with large values of $\sigma_{CR,\%}$)

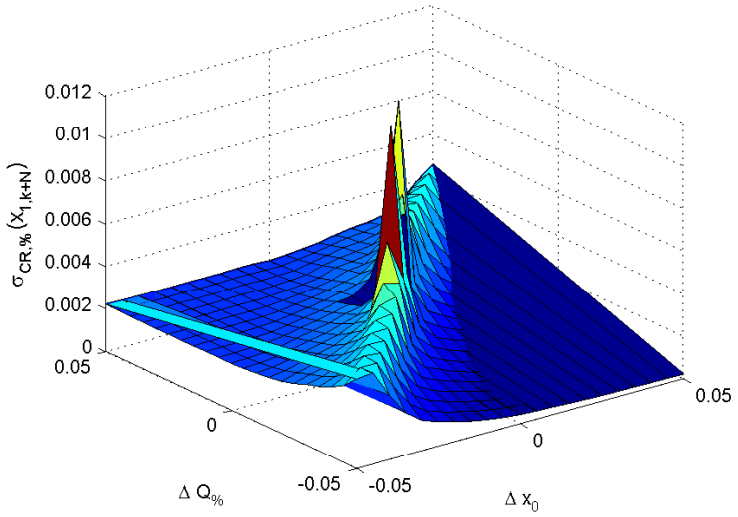

Figure 5.8: $\sigma_{CR,\%}(x_{1,k+N})$ for all combinations of SOC and capacity imbalance in Eq.(5.22) when $\frac{NI\Delta t}{Q} = 90\%$ and $1/\Delta t = 0.2Hz$.

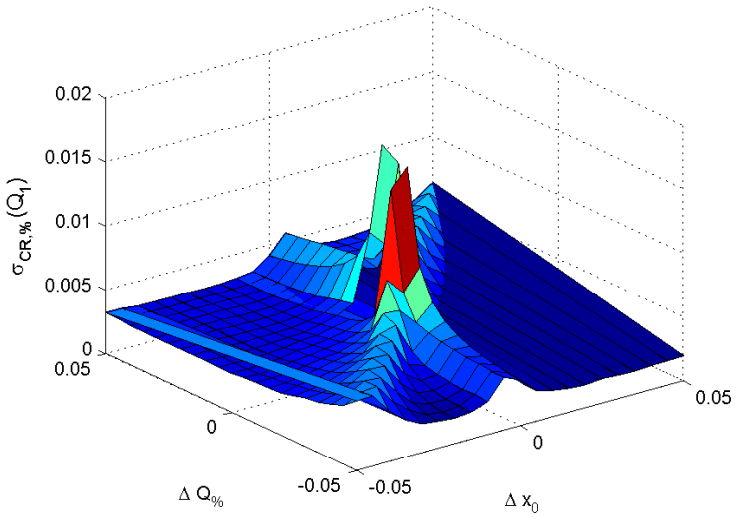

Figure 5.9: $\sigma_{CR,\%}(Q_1)$ for all combinations of SOC and capacity imbalance in Eq.(5.22) when $\frac{NI\Delta t}{Q} = 90\%$ and $1/\Delta t = 0.2Hz$.

when both $|\Delta Q_{\%}|$ and $|\Delta x_0|$ are small. The reason is that for those combinations, the imbalance between the two cell capacities and SOCs (throughout the trajectory) are very small, and thus the first two and the last two columns of the sensitivity matrix $\frac{\partial H}{\partial(x_{str,k+N},Q)}$ in Eq.(5.15) are almost identical. Therefore, the sensitivity matrix will have small singular values, resulting in large diagonal elements of the inverse of F_{info}

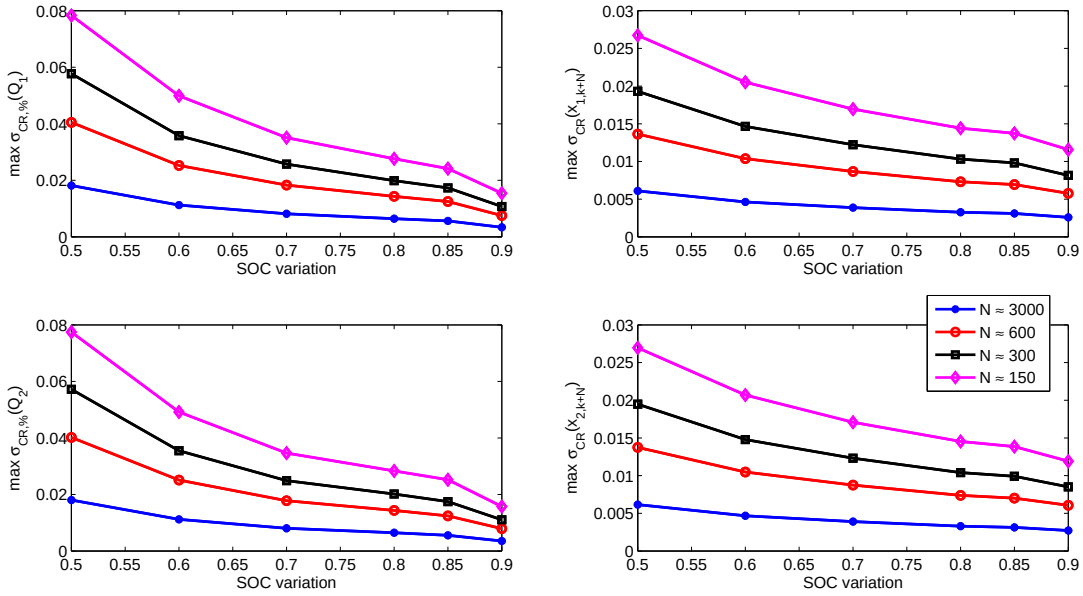

Figure 5.10: Worst-case σ_{CR} of all considered combinations of SOC and capacity imbalance for voltage trajectories with different SOC variation and number of data points.

which contains the sensitivity matrix. For such combinations, direct estimation of all four parameters, x_1 x_2, Q_1 and Q_2, will be inaccurate and unrobust. Nevertheless, since the imbalance between the SOCs and capacities is insignificant, estimation of the average SOC and capacity will be adequate for these combinations. In the next subsection, the Newton-Raphson algorithm for capacity and SOC joint estimation will be introduced, which is based on singular value decomposition of the sensitivity matrix. The designed observer will estimate only the average SOC and capacity when both $|\Delta Q_{\%}|$ and $|\Delta x_0|$ are small. Here, when determining the data collection strategy, we only consider the combinations with $|\Delta Q_{\%}| > 1\%$ and $|\Delta x_0| > 1\%$. The maximum (worst-case) $\sigma_{CR,\%}$ of all the considered combinations under voltage trajectories with different SOC variation and number of data points are shown in Fig. 5.10. The presented data are also listed in Table. 5.2. The data collection strategy can be determined based on Table. 5.2 according to the specified estimation accuracy. For example, if it is required that the standard deviation of SOC estimation needs to be less than 1%, and that of capacity estimation within 1.5%, the SOC variation should be larger than 80% and the data points need to be more than 600. Obviously, larger SOC variation and number of data points in the voltage trajectory

SOC Variation	No. of Data	$\sigma_{CR,\%}(Q_1)$	$\sigma_{CR,\%}(Q_2)$	$\sigma_{CR}(x_{1,k+N})$	$\sigma_{CR}(x_{2,k+N})$
50%	150	$\leq 7.83\%$	$\leq 7.74\%$	$\leq 2.67\%$	$\leq 2.70\%$
60%	150	$\leq 5.00\%$	$\leq 4.91\%$	$\leq 2.05\%$	$\leq 2.07\%$
70%	150	$\leq 3.51\%$	$\leq 3.46\%$	$\leq 1.69\%$	$\leq 1.71\%$
80%	150	$\leq 2.76\%$	$\leq 2.83\%$	$\leq 1.44\%$	$\leq 1.45\%$
85%	150	$\leq 2.42\%$	$\leq 2.52\%$	$\leq 1.37\%$	$\leq 1.39\%$
90%	150	$\leq 1.54\%$	$\leq 1.57\%$	$\leq 1.16\%$	$\leq 1.19\%$
50%	300	$\leq 5.77\%$	$\leq 5.72\%$	$\leq 1.93\%$	$\leq 1.95\%$
60%	300	$\leq 3.58\%$	$\leq 3.55\%$	$\leq 1.47\%$	$\leq 1.48\%$
70%	300	$\leq 2.57\%$	$\leq 2.49\%$	$\leq 1.22\%$	$\leq 1.23\%$
80%	300	$\leq 1.99\%$	$\leq 2.02\%$	$\leq 1.03\%$	$\leq 1.04\%$
85%	300	$\leq 1.73\%$	$\leq 1.75\%$	$\leq 0.98\%$	$\leq 0.99\%$
90%	300	$\leq 1.07\%$	$\leq 1.10\%$	$\leq 0.81\%$	$\leq 0.85\%$
50%	600	$\leq 4.05\%$	$\leq 4.02\%$	$\leq 1.36\%$	$\leq 1.38\%$
60%	600	$\leq 2.53\%$	$\leq 2.51\%$	$\leq 1.04\%$	$\leq 1.05\%$
70%	600	$\leq 1.83\%$	$\leq 1.78\%$	$\leq 0.87\%$	$\leq 0.87\%$
80%	600	$\leq 1.43\%$	$\leq 1.44\%$	$\leq 0.73\%$	$\leq 0.74\%$
85%	600	$\leq 1.25\%$	$\leq 1.24\%$	$\leq 0.69\%$	$\leq 0.70\%$
90%	3000	$\leq 0.75\%$	$\leq 0.79\%$	$\leq 0.58\%$	$\leq 0.61\%$
50%	3000	$\leq 1.82\%$	$\leq 1.80\%$	$\leq 0.61\%$	$\leq 0.62\%$
60%	3000	$\leq 1.12\%$	$\leq 1.12\%$	$\leq 0.46\%$	$\leq 0.47\%$
70%	3000	$\leq 0.82\%$	$\leq 0.80\%$	$\leq 0.39\%$	$\leq 0.39\%$
80%	3000	$\leq 0.64\%$	$\leq 0.64\%$	$\leq 0.33\%$	$\leq 0.33\%$
85%	3000	$\leq 0.56\%$	$\leq 0.56\%$	$\leq 0.31\%$	$\leq 0.31\%$
90%	3000	$\leq 0.34\%$	$\leq 0.35\%$	$\leq 0.26\%$	$\leq 0.27\%$

Table 5.2: Initial guess and identification results of parameters.

are favored for better estimation accuracy. However, as has been mentioned, since the batteries are not necessarily discharged to low SOC on a daily basis, e.g. 20%, large SOC variation may not be achievable at every overnight charging. Meanwhile, computational load and required data storage will increase with the number of data processed, which might be a concern for onboard microprocessors. In addition, it is noted that the Cramer-Rao bound indicates the theoretical best accuracy that can be achieved by any unbiased estimator, but the existence of an estimator that could achieve the bound is not guaranteed. Therefore, the requirements on the voltage trajectory based on the Cramer-Rao bound should be considered as necessary but not sufficient conditions.

5.3.2 SOC and Capacity Joint Estimation Algorithm based on the Newton-Raphson Method

Based on the voltage trajectory in Eq.(5.14), the Newton-Raphson method can be used to estimate both SOC and capacity over iterations,

$$\begin{bmatrix} \hat{x}^{j+1}_{str,k+N} \\ \hat{Q}^{j+1} \end{bmatrix} = \begin{bmatrix} \hat{x}^{j}_{str,k+N} \\ \hat{Q}^{j} \end{bmatrix} + \left[\mathbf{J}(\hat{x}^{j}_{str,k+N}, \hat{Q}^{j})\right]^{-1} \left(V_{str,[k,k+N]} - H(\hat{x}^{j}_{str,k+N}, \hat{Q}^{j})\right), \tag{5.23}$$
$$\mathbf{J}(\hat{x}^{j}_{str,k+N}, \hat{Q}^{j}) = \frac{\partial H}{\partial (x_{str,k+N}, Q)}(\hat{x}^{j}_{str,k+N}, \hat{Q}^{j})$$

where the Jacobian matrix $\mathbf{J}$ is the same as the sensitivity matrix specified in Eq.(5.15) except that the actual SOCs and capacities are replaced by the estimates.

As has been mentioned, when the SOC and capacity imbalance is very small, the Jacobian matrix in Eq.(5.23) will be close to rank-deficient, no matter what SOC variation $\frac{NI\Delta t}{Q}$ and number of data points N are chosen. The estimation will be unrobust as the Jacobian is hardly invertible with large condition number. Several methods can be used to address this issue. For example, the previously introduced Levenberg-Marquardt iteration in Eq.(4.43) can be used instead, where a stabilizing factor b is applied to improve the condition number of the Jacobian. Nevertheless, it is not clear how to tune the stabilizing factor to make the estimation robust for all combinations.

Another method to improve the robustness of estimation under slight imbalance is based on singular value decomposition (SVD) of the Jacobian matrix [65]. The

SVD [129] of the Jacobian matrix can be represented as

$$\begin{aligned} \mathbf{J}(\hat{x}^j_{str,k+N}, \hat{Q}^j) &= \mathbf{U}\mathbf{\Sigma}\mathbf{V}^T, \\ \mathbf{U} \in &\mathbf{R}^{N+1\times N+1}, \quad \mathbf{\Sigma} \in \mathbf{R}^{N+1\times 4}, \quad \mathbf{V} \in \mathbf{R}^{4\times 4}, \end{aligned} \tag{5.24}$$

where $\mathbf{U}$ and $\mathbf{V}$ are unitary matrices consisting of the left and right singular vectors of $\mathbf{J}$ respectively, and $\mathbf{\Sigma}$ is a rectangular diagonal matrix whose diagonal elements correspond to the singular values of $\mathbf{J}$,

$$\mathbf{\Sigma} = \begin{bmatrix} \sigma_1 & 0 & 0 & 0 \\ 0 & \sigma_2 & 0 & 0 \\ 0 & 0 & \sigma_3 & 0 \\ 0 & 0 & 0 & \sigma_4 \\ 0 & 0 & 0 & 0 \\ & \cdots & \cdots & \\ 0 & 0 & 0 & 0 \end{bmatrix}. \tag{5.25}$$

Let's arrange the four singular values as $\sigma_1 \geq \sigma_2 \geq \sigma_3 \geq \sigma_4$. The pseudoinverse of $\mathbf{J}$ can be obtained based on SVD as

$$\mathbf{J}^{-1} = \mathbf{V}\mathbf{\Sigma}^{-1}\mathbf{U}^T, \tag{5.26}$$

where

$$\mathbf{\Sigma}^{-1} = \begin{bmatrix} {\sigma_1}^{-1} & 0 & 0 & 0 & \cdots & 0 \\ 0 & {\sigma_2}^{-1} & 0 & 0 & \cdots & 0 \\ 0 & 0 & {\sigma_3}^{-1} & 0 & \cdots & 0 \\ 0 & 0 & 0 & {\sigma_4}^{-1} & \cdots & 0 \end{bmatrix}. \tag{5.27}$$

When the SOC and capacity imbalance is insignificant, the two smaller singular values of $\mathbf{J}$, σ_3 and σ_4, will be close to zero. Therefore, according to Eq.(5.27), the inversion of $\mathbf{J}$ will be unrobust because σ_3^{-1} and σ_4^{-1} are close to infinity. To address this issue, a modified pseudoinverse can be used instead, where the σ_i^{-1} term in Eq.(5.27) is replaced by 0 if σ_i is smaller than a certain threshold [65]. Two thresholds, δ_1 and δ_2, are applied here to constrain the singular values as well as the condition number of $\mathbf{J}$, which are

$$\sigma_i^{-1} \to 0 \quad \text{if} \quad \sigma_i < \delta_1 \quad \text{or} \quad \frac{\sigma_i}{\sigma_{max}} < \delta_2. \tag{5.28}$$

By applying Eq.(5.28), the estimation will proceed only in the robustly observable part of the system, which are indicated by the right singular vectors in $\mathbf{V}$. Consider

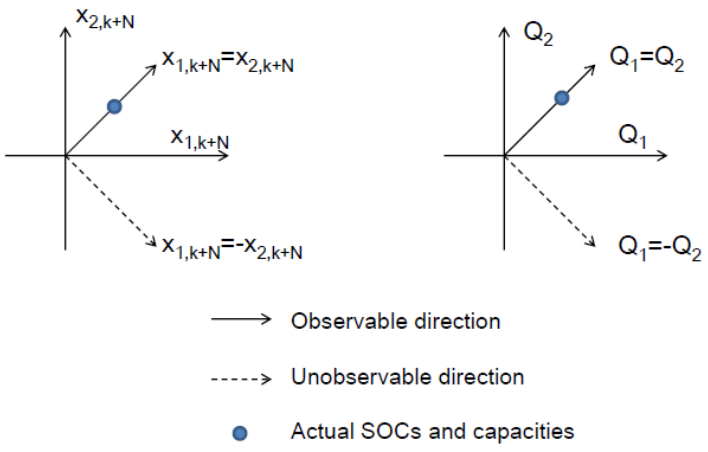

Figure 5.11: Directions of the observable and unobservable parts of capacity and SOC estimation for the case in Eq.(5.29).

the case

$$x_{1,0} = 0.05 \quad x_{2,0} = 0.05, \quad Q_1 = 0.95Q_0, \quad Q_2 = 0.95Q_0 \tag{5.29}$$

as an example. Under SOC variation $\frac{NI\Delta t}{Q} = 90\%$ and number of data points $N = 300$, the $\mathbf{\Sigma}$ and $\mathbf{V}$ matrices are calculated as

$$\begin{aligned} \mathbf{\Sigma} &= \begin{bmatrix} 1.66(\sigma_1) & 0 & 0 & 0 \\ 0 & 0.56(\sigma_2) & 0 & 0 \\ 0 & 0 & 0(\sigma_3) & 0 \\ 0 & 0 & 0 & 0(\sigma_4) \\ & \cdots & \cdots & \\ 0 & 0 & 0 & 0 \end{bmatrix}, \\ \mathbf{V} &= \begin{bmatrix} -0.6775 & 0.2024 & -0.5129 & 0.4868 \\ -0.6775 & 0.2024 & 0.5129 & -0.4868 \\ -0.2024 & -0.6775 & -0.4868 & -0.5129 \\ -0.2024 & -0.6775 & 0.4868 & 0.5129 \end{bmatrix}. \end{aligned} \tag{5.30}$$

The first two columns of $\mathbf{V}$, which correspond to the non-zero singular values σ_1 and σ_2, represent the (strongly) observable part of $\begin{bmatrix} x_{1,k+N} & x_{2,k+N} & Q_1 & Q_2 \end{bmatrix}^T$, and the last two columns (with 0 singular values) are associated with the unobservable part. The directions of the observable and unobservable parts are shown in Fig. 5.11. When the inverse of Jacobian is calculated based on Eq.(5.26)-Eq.(5.28), the estimation will

proceed along the observable direction, which are $x_{1,k+N} = x_{2,k+N}$ and Q_1 and Q_2. This direction is where the actual SOCs and capacities lie in, as specified in Eq.(5.29). Therefore, the estimates will still converge to the actual values, and the robustness of estimation is greatly enhanced compared to the algorithm without SVD. When the imbalance between SOCs and capacities is small but non-zero, all four singular values will be greater than zero. The directions are then categorized as strongly observable directions and weakly observable directions. The (strongly) observable directions will be roughly aligned with $x_{1,k+N} = x_{2,k+N}$ and $Q_1 = Q_2$. By neglecting the weakly observable directions based on Eq.(5.28), the estimates will converge to the approximate average values of SOC and capacity, which are good enough under slight imbalance.

Many methods are available for implementing the singular value decomposition of the Jacobian matrix $\mathbf{J}$ online. The simplest way is to apply principal component analysis (PCA) to $\mathbf{J}^T\mathbf{J}$ [129, 130]. However, this method may suffer from numerical issues. For example, it is shown in [131] that $\mathbf{J}^T\mathbf{J}$ might lose rank if certain entries of $\mathbf{J}$ are remarkably smaller than 1. In order to improve the robustness of SVD, various methods can be considered, including the iterative method based on bidiagonal matrix transformation [129], alternating $L1$ regression algorithm [130] among others.

Simulation has been conducted to show the performance of the estimation algorithm for different combinations of SOC and capacity imbalance under measurement noises. The results for the five cases in Table 5.1 (with no uncertainty in resistance) by using voltage trajectories covering two different SOC variation $\frac{NI\Delta t}{Q}$ and two different number of data points (N) are shown in Fig. 5.12 - Fig. 5.15 (one for each variable) as examples. The standard deviation of the Gaussian voltage measurement noises is set as 3 mV, and simulation is repeated for 100 times so that the standard deviation of the estimates can be calculated approximately. It is noted that the Cramer-Rao bound for case 6, which has no SOC and capacity imbalance, is not listed because the Fisher information matrix is not invertible due to zero singular values of the sensitivity matrix in Eq.(5.15). It can be seen from the figures that the standard deviation calculated from simulation is generally larger than that specified by the Cramer-Rao bound with very few exceptions (the reason might be that 100 repetitions are still not sufficient for characterizing the standard deviation of the estimation). The maximum standard deviation (in percentage) is listed in Table 5.3 and compared with the Cramer-Rao bound for the shown $\frac{NI\Delta t}{Q}$ and N in Fig. 5.12 - Fig. 5.15. The trend of estimation accuracy seen in simulation is the same as that based on Cramer-Rao bound, which improves under larger SOC variation and number of

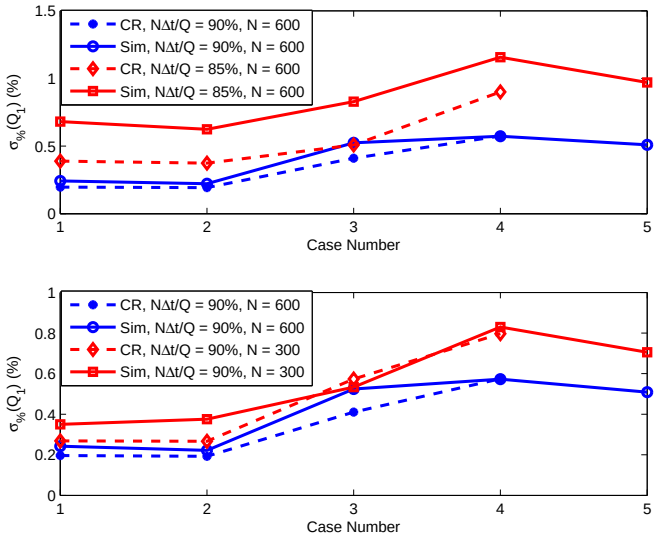

Figure 5.12: Standard deviation of the estimate of Q_1 calculated based on simulation and Cramer-Rao bound.

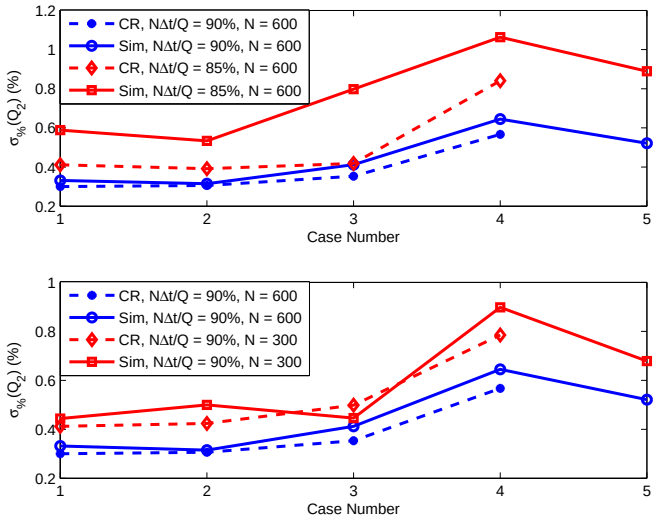

Figure 5.13: Standard deviation of the estimate of Q_2 calculated based on simulation and Cramer-Rao bound.

data points covered by the voltage trajectory.

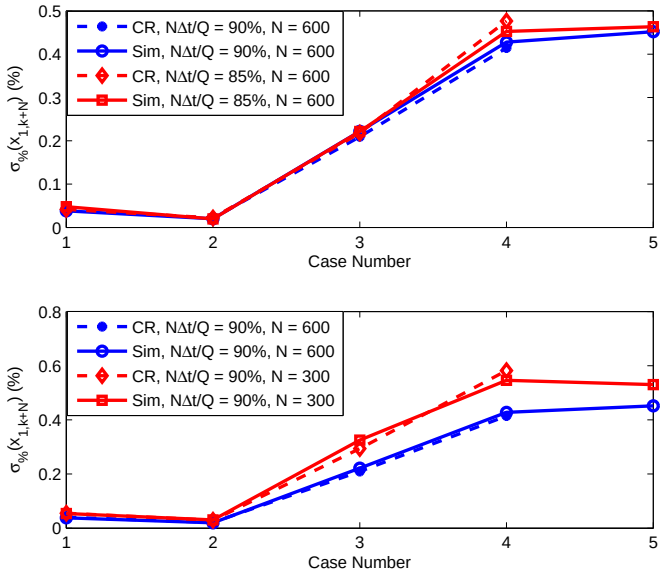

Figure 5.14: Standard deviation of the estimate of $x_{1,k+N}$ calculated based on simulation and Cramer-Rao bound.

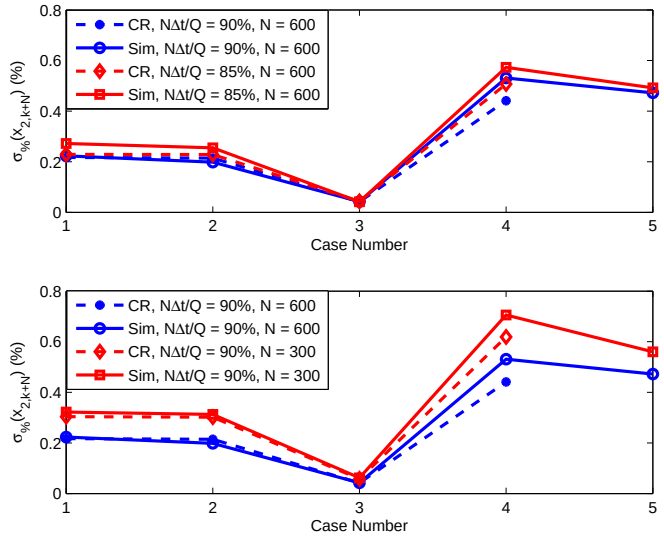

Figure 5.15: Standard deviation of the estimate of $x_{2,k+N}$ calculated based on simulation and Cramer-Rao bound.

5.4 Overall Estimation Scheme - Combining Real-Time SOC Estimation and Off-line Joint Estimation of SOC and Capacity

The SOC estimation algorithm under reduced voltage sensing based on the Newton observer has been studied in Chapter IV, and the algorithm for joint estimation of

$\frac{NI\Delta t}{Q}$ and N	$\frac{NI\Delta t}{Q} = 90\%$ $N = 600$	$\frac{NI\Delta t}{Q} = 85\%$ $N = 600$	$\frac{NI\Delta t}{Q} = 90\%$ $N = 300$
$\sigma_{CR,\%}(Q_1)$	$\leq 0.57\%$	$\leq 0.90\%$	$\leq 0.80\%$
$\sigma_{Sim,\%}(Q_1)$	$\leq 0.57\%$	$\leq 1.16\%$	$\leq 0.83\%$
$\sigma_{CR,\%}(Q_2)$	$\leq 0.57\%$	$\leq 0.84\%$	$\leq 0.79\%$
$\sigma_{Sim,\%}(Q_2)$	$\leq 0.64\%$	$\leq 1.06\%$	$\leq 0.90\%$
$\sigma_{CR,\%}(x_{1,k+N})$	$\leq 0.41\%$	$\leq 0.48\%$	$\leq 0.58\%$
$\sigma_{Sim,\%}(x_{1,k+N})$	$\leq 0.43\%$	$\leq 0.45\%$	$\leq 0.55\%$
$\sigma_{CR,\%}(x_{2,k+N})$	$\leq 0.44\%$	$\leq 0.51\%$	$\leq 0.62\%$
$\sigma_{Sim,\%}(x_{2,k+N})$	$\leq 0.53\%$	$\leq 0.57\%$	$\leq 0.71\%$

Table 5.3: Comparison of the standard deviation calculated based on Cramer-Rao bound and simulation.

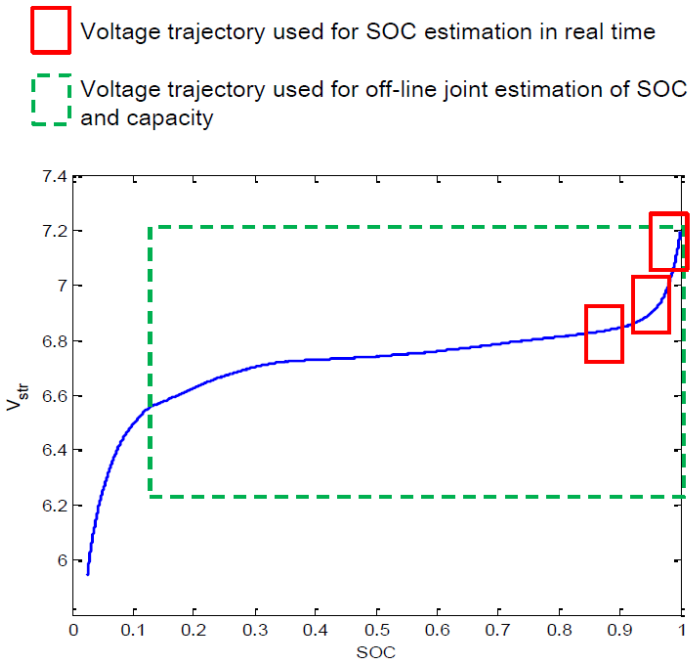

Figure 5.16: Voltage trajectories used for real-time SOC estimation and off-line joint estimation of SOC and capacity.

SOC and capacity is discussed in the previous section. The overall estimation scheme which could be used in the onboard BMS will be formulated in this section.

Since the overcharge of batteries should be prevented strictly, the SOC estimation algorithm in Eq.(4.41) needs to be performed in real time. The algorithm is currently designed primarily for constant current charging, which emulates the daily (overnight) charging of PHEVs and BEVs. At each estimation step, the moving window of the voltage trajectory used could not be too large (with small SOC variation and number of data points), as shown in Fig. 5.16, for two reasons. First, due to real

time requirement, computation needs to be fast enough and thus the number of data points used should be limited. Second, small SOC variation could reduce the estimation error caused by the uncertainty in capacity. In addition, the change in SOC between consecutive estimation windows also needs to be small enough to eradicate the risk of overcharging the battery during estimation interval. Therefore, as has been mentioned in Chapter IV, the number of data points contained in the voltage trajectory is chosen as $N = 15$, which are sampled 10 seconds apart (10 s from k to $k + 1$). The time interval between each estimation step is chosen as 20 seconds. In this way, SOC estimation is updated every 20 seconds, corresponding to an SOC increment of 0.5%.

As for the joint estimation of SOC and capacity, it will not be performed in real time but rather in off-line mode. The reason is that in order to achieve high estimation accuracy, the algorithm needs to use voltage trajectories that cover a wide range of SOC variation and large number of data points (hundreds and even thousands), as shown in Fig. 5.16. Therefore, the joint estimation is only performed once after the charging is completed due to the high computational load. The estimates obtained from real-time SOC estimation are used as the initial guess for joint estimation. In addition, the algorithm is scheduled to perform on a weekly or monthly basis instead of on a daily basis. This is because, on one hand, the battery capacity is usually changing very slowly over lifetime due to degradation, and thus weekly or monthly update is sufficient. On the other hand, the batteries in EVs are not necessarily discharged to a low SOC (e.g. 20%) everyday, but possibly once every week or month. The joint estimation will be conducted when low SOC is reached so that the SOC variation in the voltage trajectory is large enough to provide good estimation accuracy. The estimated capacities will be used in the subsequent real-time SOC estimation.

5.5 Conclusions

The issue of joint estimation of battery capacity and SOC imbalance is discussed in this chapter. First, it is shown that the accuracy of the previously designed SOC estimation algorithm will be affected by uncertainty (and imbalance) in battery capacity. The impact could be inegligible under some combinations of SOC and capacity imbalance. An algorithm for joint estimation of SOC and capacity is then designed based on the Newton-Raphson method. Based on the sensitivity and Cramer-Rao bound analysis, it is found that to achieve high estimation accuracy, the voltage

trajectory needs to cover large SOC variation and number of data points. The quantitative relationship between SOC variation, number of data points and the variance of the estimates is established based on the Cramer-Rao bound. In order to improve the robustness of estimation under small imbalance, singular value decomposition is applied to the Jacobian matrix to constrain the estimation along the strongly observable directions. The estimation of battery capacity can not only improve the accuracy of SOC estimation, but also be used to evaluate battery health based on capacity shrink. Finally, the overall estimation scheme is introduced, where the SOC estimation is scheduled to perform in real time, and the joint estimation of SOC and capacity is conducted on a weekly or monthly basis.

CHAPTER VI

Conclusions and Future Work

6.1 Conclusions

This dissertation is dedicated to studying advanced techniques for battery state estimation, which is critical for the battery management system.

First, adaptive estimation of battery thermal dynamics is investigated both on the single-cell level and on the pack level. On the single-cell level, an on-line parameterization algorithm is designed to identify the parameters of a two-state thermal model. The parameters are then used in the model-based observer to estimate the unmeasurable core temperature of a cylindrical battery cell. The identified battery internal resistance can also be used for battery state of health estimation. Pack-level temperature estimation is then studied by using a battery string thermal model constructed based on the single-cell model. Temperature sensor deployment strategy is explored based on observability analysis of the string thermal model. Nevertheless, since the number of sensors implemented in commercial battery packs is much less than the number required for observability, robust optimal observers for temperature estimation are then designed under unobservable condition subject to uncertainty in battery internal resistance. The proposed methodology can be used for robust and adaptive estimation of temperature distribution in a battery pack, which captures the temperature difference both between cells and across a single cell.

Second, the method is designed for estimating individual cell state of charge and capacity under reduced voltage sensing. It is first shown that the observability of the individual cell SOCs from the total voltage depends on the nonlinearity of the voltage-SOC relationship. The Newton observer is then used to implement the SOC estimation by using the trajectory of the measured total voltage over time. The discussion is later extended to the more complicated case where both SOC and capacity imbalance exist in the battery string. Robustness of the previously developed

SOC estimation algorithm under capacity imbalance (and hence uncertainty) is first examined. The Newton observer is then applied for joint estimation of SOC and capacity. In addition, the quantitative relationship between the measurement noise and the variance of estimates is established based on Cramer-Rao bound analysis to guide the data collection strategy. The developed estimation technique provides the potential of reducing the voltage sensing in battery packs by half, which is significant for cutting the cost of the battery management system.

6.2 Recommendations for Future Work

Future work for improving and/or extending the research in this dissertation is summarized as follows.

6.2.1 Temperature Estimation on the Battery Pack Level

First, the thermal model of the battery string constructed in Chapter III needs to be validated under experiments. With experimental data, some pack-level thermal parameters, such as the cell-to-cell heat conduction resistance, can also be identified. Based on the validated model, the developed methodology, including the observability analysis and optimal observer design, could produce more accurate results.

Second, the 1-D battery string model, as shown in Fig. 3.1, considers only the temperature gradient across the cells along the coolant flow path. The underlying assumption is that the temperature gradient across different rows (perpendicular to the flow direction) is negligible. This assumption may not be valid for some pack configurations, e.g. where the cooling conditions are not the same for cells in different rows. In this case, a more complicated model, such as a 2-D model, needs to be considered.

Meanwhile, the measurement technique for pack-level temperature monitoring is undergoing fast development. For example, in [132], a thin-film temperature sensor is being developed, which can be easily attached to a single cell to measure its temperature and pressure. With this small and cheap sensor, more temperature measurements could be implemented inside a battery pack, which would improve the model-based temperature estimation by enhancing the observability of temperature states.

6.2.2 SOC and Capacity Estimation under Reduced Voltage Sensing

The work on battery SOC and capacity estimation under reduced voltage sensing can be extended in the following directions.

First, it is desirable to extend the algorithm to real-world driving conditions, which are more commonly seen in the daily operation of electric vehicles. The SOC estimation algorithm developed in this dissertation based on the Newton Observer has been validated by experiments under the constant-current charging condition. The observer is built upon a coulomb counting model, which is sufficient for capturing the battery voltage dynamics under constant-current charging. When extended to the complicated driving conditions, the coulomb counting model is no longer adequate for capturing the battery voltage dynamics. More complicated models need to be used in this case, including the equivalent circuit model, the simplified electro-chemical model among others. For example, the equivalent circuit model parameterized in [81, 133] for the $LiFePO_4$/graphite battery can be considered as a suitable choice. Ideally, the Newton observer can be built directly upon the new model. However, model uncertainty will become a major concern. It is impossible to predict the battery voltage perfectly under dynamic current input with a model, and the mismatch in voltage could be much larger than that under constant current charging. The voltage mismatch will translate into SOC estimation error and thus affect the accuracy of estimation. The robustness of the algorithm is expected to be a major challenge for SOC estimation under dynamic current.

Second, reduced voltage sensing is limited to the case when the voltage is measured at a two-cell interval. It is desirable to investigate the more general case of measuring every n-cell interval so as to further reduce the amount of voltage sensing. It is possible to extend the methodology developed in this dissertation, such as the observability analysis and the Newton observer, to the general cases. But some practical limitations are anticipated. For example, the requirement on the voltage-SOC relationship for observability of individual cell SOCs will become more stringent. Given the same battery chemistry, observability will be weaker as more cells are involved. Computational load might also be a concern as the dimension of the Jacobian matrix to be inverted in the Newton observer will increase with the number of cells.

In addition, the imbalance (and uncertainty) in battery internal resistance, though considered in the robustness analysis of SOC estimation, has not been incorporated in the estimation algorithm. It is noted that when only the total voltage is measured, it is impossible to identify the resistance of each cell, since they always add up and show as a lumped ohmic voltage drop. Estimation of the total resistance can be addressed by augmenting the Newton observer to include the total resistance as a new variable. Furthermore, the voltage-SOC relationship is assumed to be known and unchanged in this dissertation. However, as reported in literature [134], the shape

of the open-circuit-voltage curve may also change over battery lifetime for certain battery chemistries. The degradation pattern of the shape change and its impact on imbalance estimation remains to be investigated.

APPENDIX

APPENDIX A

Discrete-time Parameter Identification Algorithm for Single Cell Battery Thermal Model

For a discrete-time parametric model,

$$z(k) = \theta^T \phi(k), \tag{A.1}$$

the recursive least squares algorithm for parameter identification takes the form [135]

$$\begin{aligned} \hat{\theta}(k) &= \hat{\theta}(k-1) + P(k)\phi(k)\epsilon(k) \\ P(k) &= P(k-1) - \frac{P(k-1)\phi(k)\phi^T(k)P(k-1)}{\phi^T(k)P(k-1)\phi(k)} \\ \epsilon(k) &= z(k) - \hat{\theta}(k-1)\phi(k), \end{aligned} \tag{A.2}$$

where k denotes the time instant, θ is the parameter vector, $z(k)$ and $\phi(k)$ are the observation and regressor in discrete time.

The discrete-time parametric model for single cell battery thermal dynamics is derived as follows. Based on Eq.(2.1) under small sampling period Δt, the thermal model in discrete time can be obtained as

$$\begin{aligned} T_c(k) &\approx T_c(k-1) + \frac{I^2(k-1)R_e}{C_c}\Delta t + \frac{T_s(k-1) - T_c(k-1)}{R_c}\Delta t \\ T_s(k) &\approx T_s(k-1) + \frac{T_c(k-1) - T_s(k-1)}{R_c}\Delta t + \frac{T_f(k-1) - T_s(k-1)}{R_u}\Delta t, \end{aligned} \tag{A.3}$$

or

$$
\begin{aligned}
T_c(k) &= (1 - \frac{\Delta t}{R_c C_c})T_c(k-1) + \frac{\Delta t}{R_c C_c}T_s(k-1) + \frac{\Delta t R_e}{C_c}I^2(k-1) \\
T_s(k) &= \frac{\Delta t}{R_c C_s}T_c(k-1) + (1 - \frac{\Delta t}{R_c C_s} - \frac{\Delta t}{R_u C_s})T_s(k-1) + \frac{\Delta t}{R_u C_s}T_f(k-1).
\end{aligned}
\tag{A.4}
$$

By combining the two equations in Eq.(A.4) and replacing the unmeasured T_c with measured I, T_f , and T_s, the parametric model is derived as

$$
\begin{aligned}
T_s(k+2) = &\left(2 - \frac{\Delta t}{R_c C_s} - \frac{\Delta t}{R_c C_c} - \frac{\Delta t}{R_u C_s}\right)T_s(k+1) \\
&+ \left(\frac{\Delta t}{R_c C_s} + \frac{\Delta t}{R_c C_c} + \frac{\Delta t}{R_u C_s} - \frac{\Delta t^2}{R_c C_c R_u C_s} - 1\right)T_s(k) \\
&+ \frac{\Delta t}{R_u C_s}T_f(k+1) - \left(1 - \frac{\Delta t^2}{R_c C_c R_u C_s}\right)T_f(k) + \frac{R_e \Delta t^2}{R_c C_s C_c}I^2(k).
\end{aligned}
\tag{A.5}
$$

When T_f is regulated as a steady output, we have $T_f(k+1) = T_f(k)$, and Eq.(A.5) will be reduced to

$$
\begin{aligned}
T_s(k+2) = &\left(2 - \frac{\Delta t}{R_c C_s} - \frac{\Delta t}{R_c C_c} - \frac{\Delta t}{R_u C_s}\right)T_s(k+1) \\
&+ \left(\frac{\Delta t}{R_c C_s} + \frac{\Delta t}{R_c C_c} + \frac{\Delta t}{R_u C_s} - \frac{\Delta t^2}{R_c C_c R_u C_s} - 1\right)T_s(k) \\
&+ \left(\frac{\Delta t^2}{R_c C_c R_u C_s}\right)T_f(k) + \frac{R_e \Delta t^2}{R_c C_s C_c}I^2(k).
\end{aligned}
\tag{A.6}
$$

By using the notation for the lumped parameters in Eq.(2.11), the parametric model is denoted as

$$
\begin{aligned}
T_s(k+2) = &\alpha \Delta t^2 I^2(k) + \beta \Delta t^2 \big(T_f(k) - T_s(k)\big) \\
&+ (2 - \gamma \Delta t)T_s(k+1) + (\gamma \Delta t - 1)T_s(k).
\end{aligned}
\tag{A.7}
$$

The least squares algorithm in Eq.(A.2) can then be applied to identify the lumped parameters α, β and γ, and the original physical parameters could be obtained based on Eq.(2.12).

BIBLIOGRAPHY

BIBLIOGRAPHY

[1] *International Energy Outlook 2013.* U.S. Energy Information Administration, 2013.

[2] *Monthly Energy Review: March 2014.* U.S. Energy Information Administration, 2014.

[3] T. M. Bandhauer, S. Garimella, and T. F. Fuller, "A critical review of thermal issues in lithium-ion batteries," *Journal of The Electrochemical Society*, vol. 158, pp. 1–25, 2011.

[4] M. Wakihara, "Recent developments in lithium ion batteries," *Material Science and Engineering*, vol. 33, pp. 109–134, 2001.

[5] M. Winter and R. J. Brodd, "What are batteries, fuel cells, and supercapacitors?," *Chem. Rev.*, vol. 35, pp. 4245–4269, 2004.

[6] J. McDowat, "Conventional battery technologies-present & future," in *IEEE Power Engineering Society Summer Meeting*, 2000.

[7] A. Affanni, A. Bellini, G. Franceschini, P. Guglielmi, and C. Tassoni, "Battery choice and management for new-generation electric vehicles," *IEEE Transactions on Industrial Electronics*, vol. 52, pp. 1343–1349, 2005.

[8] L. Lu, X. Han, J. Li, J. Hua, and M. Ouyang, "A review on the key issues for lithium-ion battery management in electric vehicles," *Journal of Power Sources*, vol. 226, pp. 272–288, 2013.

[9] C. Vyas and D. Hurst, *Electric Vehicle Consumer Survey: Consumer Attitudes, Opinions, and Preferences for Electric Vehicles and EV Charging Stations.* Navigant Research, 2013.

[10] *http://www.slashgear.com/denso-announces-new-lithium-ion-battery-pack-for-startstop-systems-04250329/.*

[11] *http://www.greencarcongress.com/2013/09/20130911-jc.html*.

[12] D. Konishi, J. Ueda, T. Kusunoki, O. Ushijima, T. Aoki, and Y. Mizuta, "Development of 12 v lithium-ion battery for start and stop vehicle system," tech. rep., GS Yuasa International, 2013.

[13] *Global Lithium Battery Market 2011-2015*. TechNavio, 2012.

[14] J. Bates, N. Dudney, B. Neudecker, A. Ueda, and C. Evans, "Thin-?lm lithium and lithium-ion batteries," *Solid State Ionics*, vol. 135, pp. 33–45, 2000.

[15] C.-G. Kim, D.-H. Seo, J.-S. You, J.-H. Park, and B. H. Cho, "Design of a contactless battery charger for cellular phone," *IEEE Transactions on Industrial Electronics*, vol. 48, pp. 1238–1247, 2001.

[16] J. Hall, A. Schoen, A. Powers, P. Liu, and K. Kirby, "Resistance growth in lithium ion satellite cells. i. non destructive data analyses," in *208th ECS Meeting MA2005-02, October 16-October 21, 2005 , Los Angeles, California*, 2005.

[17] Q. Wang, P. Ping, X. Zhao, G. Chu, J. Sun, and C. Chen, "Thermal runaway caused fire and explosion of lithium ion battery," *Journal of Power Sources*, vol. 208, pp. 210–224, 2012.

[18] J. Briscoe and N. Raman, "Lithium ion batteries: Power sources for military aircraft," in *SAE Technical Paper 2002-01-3240*, 2002.

[19] B. Dunn, H. Kamath, and J.-M. Tarascon, "Electrical energy storage for the grid: A battery of choices," *Science*, vol. 334, pp. 928–935, 2011.

[20] B. Scrosati and J. Garche, "Lithium batteries: Status, prospects and future," *Journal of Power Sources*, vol. 195, pp. 2419–2430, 2010.

[21] S. Hossain, Y. Saleh, and R. Loutfy, "Carbon-carbon composite as anodes for lithium-ion battery systems," *Journal of Power Sources*, vol. 96, pp. 5–13, 2001.

[22] Y.-S. Lee and M.-W. Cheng, "Intelligent control battery equalization for series connected lithium-ion battery strings," *IEEE Transactions on Industrial Electronics*, vol. 52, pp. 1297–1307, 2005.

[23] X. Feng, M. Fang, X. He, M. Ouyang, L. Lu, H. Wang, and M. Zhang, "Thermal runaway features of large format prismatic lithium ion battery using extended

volume accelerating rate calorimetry," *Journal of Power Sources*, vol. 255, p. 294C301, 2014.

[24] T. Yoshida, M. Takahashi, S. Morikawa, C. Ihara, H. Katsukawa, T. Shiratsuchi, and J. ichi Yamakic, "Degradation mechanism and life prediction of lithium-ion batteries," *Journal of The Electrochemical Society*, vol. 153, pp. A576–A582, 2006.

[25] Z. Li, L. Lu, M. Ouyang, and Y. Xiao, "Modeling the capacity degradation of lifepo4/graphite batteries based on stress coupling analysis," *Journal of Power Sources*, vol. 196, pp. 9757–9766, 2011.

[26] X. Lin, J. Park, L. Liu, Y. Lee, A. M. Sastry, and W. Lua, "A comprehensive capacity fade model and analysis for li-ion batteries," *Journal of The Electrochemical Society*, vol. 160, pp. A1701–A1710, 2013.

[27] C. Forgez, D. V. Do, G. Friedrich, M. Morcrette, and C. Delacourt, "Thermal modeling of a cylindrical lifepo4/graphite lithium-ion battery," *Journal of Power Sources*, vol. 195, pp. 2961–2968, 2010.

[28] G. Zhang, L. Cao, S. Ge, C.-Y. Wang, C. E. Shaffer, and C. D. Rahn, "In situ measurement of li-ion battery internal temperature," in *224th Electrochemical Society Meeting*, 2013.

[29] E. Thomas, H. Case, D. Doughty, R. Jungst, G. Nagasubramanian, and E. Roth, "Accelerated power degradation of li-ion cells," *Journal of Power Sources*, vol. 124, pp. 254–260, 2003.

[30] K. Amine, J. Liu, and I. Belharouak, "High-temperature storage and cycling of c-lifepo4/graphite li-ion cells," *Electrochemistry Communications*, vol. 7, pp. 669–673, 2005.

[31] P. Liu, J. Wang, J. Hicks-Garner, E. Sherman, S. Soukiazian, M. Verbrugge, H. Tataria, J. Musser, and P. Finamore, "Aging mechanisms of lifepo4 batteries deduced by electrochemical and structural analyses," *J. Electrochem. Soc.*, vol. 157, pp. 499–507, 2010.

[32] F. Hoffart, "Proper care extends li-ion battery life," *Power Electronics Technology*, 2008.

[33] C. Y. Wang and V. Srinivasan, "Computational battery dynamics (cbd) – electrochemical/thermal coupled modeling and multi-scale modeling," *Journal of Power Sources*, vol. 110, pp. 364–376, 2002.

[34] S. A. Hallaj, H. Maleki, J. Hong, and J. Selman, "Thermal modeling and design considerations of lithium-ion batteries," *Journal of Power Sources*, vol. 83, pp. 1–8, 1999.

[35] H. Maleki and A. K. Shamsuri, "Thermal analysis and modeling of a notebook computer battery," *Journal of Power Sources*, vol. 115, pp. 131–136, 2003.

[36] W. B. Gu and C. Y. Wang, "Thermal-electrochemical modeling of battery systems," *Journal of The Electrochemical Society*, vol. 147, pp. 2910–2922, 2000.

[37] R. Mahamud and ChanwooPark, "Reciprocating airflow for li-ion battery thermal management to improve temperature uniformity," *Journal of Power Sources*, vol. 196, pp. 5685–5696, 2011.

[38] K. Smith and C.-Y. Wang, "Power and thermal characterization of a lithium-ion battery pack for hybrid-electric vehicles," *Journal of Power Sources*, vol. 160, p. 662C673, 2006.

[39] D. Bernardi, E. Pawlikowski, and J. Newman, "A general energy balance for battery systems," *J. Electrochem. Soc.*, vol. 132, pp. 5–12, 1985.

[40] D. G. Marchand, J. F. Szentes, D. C. Orr, and J. J. Bernardi, "System and method for determining battery temperature," *US patent No. 7,514,904*, 2005.

[41] T. Yamamoto, "Controller for rechargeable battery and temperature estimation method and deterioration determination method for rechargeable battery," *U.S patent No. 7,646,176*, 2006.

[42] C. W. Park and A. K. Jaura, "Dynamic thermal model of li-ion battery for predictive behavior in hybrid and fuel cell vehicles," in *SAE 2003-01-2286*, pp. 1835–1842, 2003.

[43] C. Mi, B. Li, D. Buck, and N. Ota, "Advanced electro-thermal modeling of lithium-ion battery system for hybrid electric vehicle applications," in *0-7803-9761-4/07/IEEE*, 2007.

[44] M. Kimishima and H. Echigoya, "Vehicle battery cooling apparatus," Nov. 19 2002. US Patent 6,481,230.

[45] T. Etoh, K. Inui, Y. Kikuchi, T. Matsuno, M. Mimoto, and S. Suzaki, "Battery cooling system for vehicle," Aug. 17 1999. US Patent 5,937,664.

[46] T. Takamura, A. Otsu, and T. Sone, "Battery temperature regulating system and method for an electric vehicle, battery housing box for an electric vehicle, and vehicle incorporating same," May 1 2012. US Patent 8,167,070.

[47] R. Williams and D. Lawrence, *Linear state-space control systems*. Wiley, 2007.

[48] R. E. Kalman, "A new approach to linear filtering and prediction problems," *Transactions of the ASME Journal of Basic Engineering*, vol. 82 (Series D), pp. 35–45, 1960.

[49] Y. Cadirci and Y. Ozkazanc, "Microcontroller-based on-line state-of-charge estimator for sealed leadcacid batteries," *Journal of Power Sources*, vol. 129, pp. 330–342, 2004.

[50] V. Johnson, A. Pesaran, and T. Sack, "Temperature-dependent battery models for high-power lithium-lon batteries," in *Proceedings of the 17th Electric Vehicle Symposium*, 2000.

[51] X. Hu, S. Li, and H. Peng, "A comparative study of equivalent circuit models for li-ion batteries," *Journal of Power Sources*, vol. 175, pp. 359–367, 2012.

[52] B. Y. Liaw, G. Nagasubramanian, R. G. Jungst, and D. H. Doughty, "Modeling of lithium ion cellsa simple equivalent-circuit model approach," *Solid State Ionics*, vol. 175, pp. 835–839, 2004.

[53] D. D. Domenico, A. Stefanopoulou, and G. Fiengo, "Lithium-ion battery state of charge and critical surface charge estimation using an electrochemical model-based extended kalman filter," *Journal of Dynamic Systems, Measurement, and Control*, vol. 132, pp. 061302–061313, 2010.

[54] K. A. Smith, C. D. Rahn, and C.-Y. Wang, "Model-based electrochemical estimation and constraint management for pulse operation of lithium ion batteries," *IEEE Transactions on Control Systems Technology*, vol. 18, pp. 654–663, 2010.

[55] N. A. Windarko and J. Choi, "Soc estimation based on ocv for nimh batteries using an improved takacs model," *Journal of Power Electronics*, vol. 10, pp. 181–186, 2010.

[56] X. Lin, A. G. Stefanopoulou, P. Laskowsky, J. S. Freudenberg, Y. Li, and R. D. Anderson, "State of charge estimation error due to parameter mismatch in a generalized explicit lithium ion battery model," in *ASME Dynamic Systems and Control Conference*, 2011.

[57] X. Hu, S. Li, H. Peng, and F. Sun, "Robustness analysis of state-of-charge estimation methods for two types of li-ion batteries," *Journal of Power Sources*, vol. 217, pp. 209–219, 2012.

[58] D. G. Luenberger, "Observers for multivariable systems," *IEEE Transactions on Automatic Control*, vol. 11, pp. 190–197, 1966.

[59] Y. Song and J. W. Grizzle, "The extended kalman filter as a local asymptotic observable for discrete-time nonlinear systems," *Journal of Mathematical Systems, Estimations and Control*, vol. 5, pp. 59–78, 1995.

[60] G. L. Plett, "Extended kalman filtering for battery management systems of lipb-based hev battery packs part 3. state and parameter estimation," *Journal of Power Sources*, vol. 134, pp. 277–292, 2004.

[61] S. Santhanagopalan and R. E. White, "Online estimation of the state of charge of a lithium ion cell," *Journal of Power Sources*, vol. 16, no. 2, pp. 1346–1355, 2006.

[62] C. Speltino, A. G. Stefanopoulou, and G. Fiengo, "Cell equalization in battery stacks through state of charge estimation polling," in *American Control Conference*, 2010.

[63] R. Hermann and A. J. Krener, "Nonlinear controllability and observability," *IEEE Transactions on Automatic Control*, vol. 5, pp. 728–740, 1977.

[64] P. E. Moraal and J. W. Grizzle, "Observer design for nonlinear systems with discrete-time measurements," *IEEE Transactions on Automatic Control*, vol. 40, pp. 395–404, 1995.

[65] P. E. Moraal and J. W. Grizzle, "Asymptotic observers for detectable and poorly observable systems," in *Proceedings of the 34th IEEE Conference on Decision & Control*, 1995.

[66] A. J. Krener and A. Isidori, "Linearization by output injection and nonlinear observers," *Systems & Control Letters*, vol. 3, pp. 47–52, 1983.

[67] D. Bestle and M. Zeitz, "Canonical form observer design for non-linear time-variable systems," *International Journal of Control*, vol. 38, pp. 419–431, 1983.

[68] S.-T. Chung and J. W. Grizzle, "Sampled-data observer error linearization," *Automatica*, vol. 26, pp. 997–1007, 1990.

[69] M. Zeitz, "The extended luenberger observer for nonlinear systems," *Systems & Control Letters*, vol. 9, pp. 149–156, 1987.

[70] J.-J. E. Slotine, J. K. Hedrick, and E. A. Mlsawa, "On sliding observers for nonlinear systems," in *American Control Conference*, 1986.

[71] S. Drakunov, "Sliding-mode observers based on equivalent control method," in *IEEE Conference on Decision and Control*, 1992.

[72] J. . P. Gauthier, H. Hammouri, and S. Othman, "A simple observer for nonlinear systems applications to bioreactors," *IEEE Transactions on Automatic Control*, vol. 37, pp. 875–880, 1992.

[73] F. Deza, E. Busvelle, J. Gauthier, and D. Rakotopara, "High gain estimation for nonlinear systems," *Systems & Control Letters*, vol. 18, pp. 295–299, 1992.

[74] J. Tsinias, "Further results on the observer design problem," *Systems & Control Letters*, vol. 14, pp. 411–418, 1990.

[75] X. Lin, H. E. Perez, J. B. Siegel, A. G. Stefanopoulou, Y. Li, and R. D. Anderson, "Quadruple adaptive observer of li-ion core temperature in cylindrical cells and their health monitoring," in *Proceedings of American Control Conference*, 2012.

[76] X. Lin, H. Perez, J. Siegel, A. Stefanopoulou, Y. Li, R. D. Anderson, Y. Ding, and M. Castanier, "Online parameterization of lumped thermal dynamics in cylindrical lithium ion batteries for core temperature estimation and health monitoring," *IEEE Transactions on Control Systems Technology*, vol. 21, pp. 1745–1755, 2013.

[77] X. Lin, H. Fu, H. E. Perez, J. B. Siegel, A. G. Stefanopoulou, Y. Ding, and M. P. Castanier, "Parameterization and observability analysis of scalable battery clusters for onboard thermal management," *Oil & Gas Science and Technology Rev. IFP Energies nouvelles, France*, vol. 68, pp. 165–178, 2013.

[78] P. A. Ioannou and J. Sun, *Robust Adaptive Control*. Prentice Hall, 1996.

[79] K. Smith, G.-H. Kim, E. Darcy, and A. Pesaran, "Thermal/electrical modeling for abuse-tolerant design of lithium ion modules," *International Journal of Energy Research*, vol. 34, p. 204C215, 2009.

[80] Y. Hu, S. Yurkovich, Y. Guezennec, and B. Yurkovich, "Electro-thermal battery model identification for automotive applications," *Journal of Power Sources*, vol. 196, pp. 448–457, 2011.

[81] H. E. Perez, J. B. Siegel, X. Lin, A. G. Stefanopoulou, Y. Ding, and M. P. Castanier, "Parameterization and validation of an integrated electro-thermal lfp battery model," in *ASME Dynamic Systems and Control Conference (DSCC)*, 2012.

[82] J. Vetter, P. Novak, M. Wagner, C. Veit, K.-C. Moller, J. Besenhard, M. Winter, M. Wohlfahrt-Mehrens, C. Vogler, and A. Hammouche, "Ageing mechanisms in lithium-ion batteries," *Journal of Power Sources*, vol. 147, pp. 269–281, 2005.

[83] J. Shim, R. Kostecki, T. Richardson, X. Song, and K. Striebel, "Electrochemical analysis for cycle performance and capacity fading of a lithium-ion battery cycled at elevated temperature," *Journal of Power Sources*, vol. 112, pp. 222–230, 2002.

[84] D. Aurbach, "Electrodecsolution interactions in li-ion batteries: a short summary and new insights," *Journal of Power Sources*, vol. 119-121, pp. 497–503, 2003.

[85] A. P. Schmidt, M. Bitzer, and L. Guzzella, "Experiment-driven electrochemical modeling and systematic parameterization for a lithium-ion battery cell," *Journal of Power Sources*, vol. 195, pp. 5071–5080, 2010.

[86] M. Verbrugge and E. Tate, "Adaptive state of charge algorithm for nickel metal hydride batteries including hysteresis phenomena," *Journal of Power Sources*, vol. 126, pp. 236–249, 2004.

[87] B. Saha, K. Goebel, S. Poll, and J. Christophersen, "Prognostics methods for battery health monitoring using a bayesian framework," *IEEE Transactions on Instrumentation and Measurement*, vol. 58, pp. 291–296, 2009.

[88] A. Zukauskas, "Heat transfer from tubes in crossflow," *Advances in Heat Transfer*, vol. 8, pp. 93–160, 1972.

[89] T.-K. Lee, Y. Kim, A. G. Stefanopoulou, and Z. Filipi, "Hybrid electric vehicle supervisory control design reflecting estimated lithium-ion battery electrochemical dynamics," in *American Control Conference*, 2011.

[90] J. Windsor, L. Silverberg, and G. Lee, "Convergence rate analysis of a multivariable recursive least squares parameter estimator," in *American Control Conference*, 1994.

[91] A. Astrom and B. Wittenmark, *Adaptive Control*. Addison Wesley, 1989.

[92] M. Dubarry, N. Vuillaume, and B. Y. Liaw, "From single cell model to battery pack simulation for li-ion batteries," *Journal of Power Sources*, vol. 186, pp. 500–507, 2009.

[93] M. Dubarry, N. Vuillaume, and B. Y. Liaw, "Origins and accommodation of cell variations in li-ion battery pack modeling," *International Journal of Energy Research*, vol. 34, pp. 216–231, 2010.

[94] *Cooling Fins Help Keep Chevrolet Volt Battery at Ideal Temperature*. General Motors Company, 2011.

[95] *Sustainable Mobility-More Than Vehicles*. Toyota Motor Corporation, 2010.

[96] A. H. Jazwinski, *Stochastic Processes and Filtering Theory*. Dover, 2007.

[97] U. Shaked and Y. Theodor, "h_∞ - optimal estimation: a tutorial," in *Proceedings of the 31st Conference on Decision and Control*, 1992.

[98] D. Simon, *Optimal state estimation: Kalman, H infinity, and nonlinear approaches*. Wiley, 2006.

[99] K. M. Grigoriadis and J. T. Watson, "Reduced-order h_∞ and $l_2 - l_\infty$ filtering via linear matrix inequalities," *IEEE Transactions on Aerospace and Electronic Systems*, vol. 33, pp. 1326–1338, 1997.

[100] R. M. Palhares and P. L. Peres, "Robust filtering with guaranteed energy-to-peak performance-an lmi approach," *Automatica*, vol. 36, pp. 851–858, 2000.

[101] D. A. Wilson, "Convolution and hankel operator norms for linear systems," in *Proceedings of the 27th Conference on Decision and Control*, 1988.

[102] R. M. Palhares and P. L. Peres, "Robust h_∞ filtering design with pole placement constraint via linear matrix inequalities," *Journal of Optimization Theory and Applications*, vol. 102, pp. 239–261, 1999.

[103] J. F. Sturm, "Using sedumi 1.02, a matlab toolbox for optimization over symmetric cones," *Optimization Methods and Software*, vol. 11, pp. 625–653, 1999.

[104] J. Efberg, "Yalmip : A toolbox for modeling and optimization in matlab," in *Proceedings of 2004 IEEE International Symposium on Computer Aided Control Systems Design*, 2004.

[105] S. Boyd and L. Vandenberghe, *Convex Optimization*. Cambridge University Press, 2004.

[106] R. T. Rockafellar, *Convex Analysis*. Princeton University Press, 1997.

[107] A. A. Pesaran, "Battery thermal models for hybrid vehicle simulations," *Journal of Power Sources*, vol. 110, pp. 377–382, 2002.

[108] W. F. Bentley, "Cell balancing considerations for lithium-ion battery systems," in *Battery Conference on Applications and Advances*, 1997.

[109] L. Y. Wang, M. Polis, G. Yin, W. Chen, Y. Fu, and C. Mi, "Battery cell identification and soc estimation using string terminal voltage measurements," *IEEE Transactions on Vehicular Technology*, vol. 61, pp. 2915–2935, 2012.

[110] X. Lin, A. G. Stefanopoulou, Y. Li, and R. D. Anderson, "State of charge estimation of cells in series connection by using only the total voltage measurement," in *Proceedings of the American Control Conference*, 2013.

[111] X. Lin, A. G. Stefanopoulou, Y. Li, and R. D. Anderson, "Parameterization and observability analysis of scalable battery clusters for onboard thermal management," *IEEE Transactions on Control Systems Technology*, Accpeted Pending Minor Revision, 2014.

[112] F. Albertini and D. D'Alessandro, "Observability and forwardcbackward observability of discrete-time nonlinear systems," *Mathematics of Control, Signals and Systems*, vol. 15, pp. 275–290, 2002.

[113] V. I. Utkin, "Variable structure systems with sliding modes," *IEEE Transactions on Automatic Control*, vol. 22, pp. 212–222, 1977.

[114] K. Levenberg, "A method for the solution of certain non-linear problems in least squares," *Quarterly of Applied Mathematics*, vol. 2, pp. 164–168, 1944.

[115] D. W. Marquardt, "An algorithm for least-squares estimation of nonlinear parameters," *Journal of the Society for Industrial and Applied Mathematics*, vol. 11, pp. 431–441, 1963.

[116] J. Kim, J. Shin, C. Chun, and B. H. Cho, "Stable configuration of a li-ion series battery pack based on a screening process for improved voltage/soc balancing," *IEEE Transactions on Power Electronics*, vol. 27, pp. 411–424, 2012.

[117] E. Wan and A. Nelson, *Kalman Filtering and Neural Networks, Chapter 5: Dual extended Kalman filter methods*. Wiley/Inter-Science, 2001.

[118] S. Lee, J. Kim, J. Lee, and B. Cho, "State-of-charge and capacity estimation of lithium-ion battery using a new open-circuit voltage versus state-of-charge," *Journal of Power Sources*, vol. 185, pp. 1367–1373, 2008.

[119] J. Kim, S. Lee, and B. H. Cho, "Complementary cooperation algorithm based on dekf combined with pattern recognition for soc/capacity estimation and soh prediction," *IEEE Transactions on Power Electronics*, vol. 27, pp. 436–451, 2012.

[120] M. Rubagotti, S. Onori, and G. Rizzoni, "Automotive battery prognostics using dual extended kalman filter," in *Proceedings of the ASME 2009 Dynamic Systems and Control Conference*, 2009.

[121] C. Hu, B. D. Youn, and J. Chung, "A multiscale framework with extended kalman filter for lithium-ion battery soc and capacity estimation," *Applied Energy*, vol. 92, pp. 694–704, 2012.

[122] H. He, R. Xiong, and H. Guo, "Online estimation of model parameters and state-of-charge of lifepo4 batteries in electric vehicles," *Applied Energy*, vol. 89, pp. 413–420, 2012.

[123] H. Dai, X. Wei, and Z. Sun, "State and parameter estimation of a hev li-ion battery pack using adaptive kalman filter with a new soc-ocv concept," in *International Conference on Measuring Technology and Mechatronics Automation*, 2009.

[124] G. L. Plett, "Recursive approximate weighted total least squares estimation of battery cell total capacity," *Journal of Power Sources*, vol. 196, pp. 2319–2331, 2011.

[125] G. L. Plett, "Sigma-point kalman filtering for battery management systems of lipb-based hev battery packs part 2: Simultaneous state and parameter estimation," *Journal of Power Sources*, vol. 161, pp. 1369–1384, 2006.

[126] B. R. Jayasankar, A. Ben-Zvi, and B. Huang, "Identifiability and estimability study for a dynamic solid oxide fuel cell model," *Computers and Chemical Engineering*, vol. 33, pp. 484–492, 2009.

[127] G. L. Plett, "Extended kalman filtering for battery management systems of lipb-based hev battery packs part 1. background," *Journal of Power Sources*, vol. 134, pp. 252–261, 2004.

[128] B. Saha and K. Goebel, "Modeling li-ion battery capacity depletion in a particle filtering framework," in *Annual Conference of the Prognostics and Health Management Society*, 2009.

[129] G. Golub and W. Kahan, "Calculating the singular values and pseudo-inverse of a matrix," *Journal of the Society for Industrial and Applied Mathematics Series B Numerical Analysis*, vol. 2, pp. 205–224, 1965.

[130] D. M. Hawkins, L. Liu, and S. S. Young, "Robust singular value decomposition," tech. rep., National Institute of Statistical Sciences, 2001.

[131] V. Klema and A. Laub, "The singular value decomposition: Its computation and some applications," *IEEE Transactions on Automatic Control*, vol. 25, pp. 164–176, 1980.

[132] *http://arpa-e.energy.gov/?q=arpa-e-projects/thin-film-temperature-sensors-batteries*. 2013.

[133] X. Lin, H. E. Perez, S. Mohan, J. B. Siegel, A. G. Stefanopoulou, Y. Ding, and M. P. Castanier, "A lumped-parameter electro-thermal model for cylindrical batteries," *Journal of Power Sources*, vol. 257, pp. 1–11, 2014.

[134] B. Y. Liaw, R. G. Jungst, G. Nagasubramanian, H. L. Case, and D. H. Doughty, "Modeling capacity fade in lithium-ion cells," *Journal of Power Sources*, vol. 140, no. 1, pp. 157 – 161, 2005.

[135] L. Ljung and T. Soderstrom, *Theory and practice of recursive identification.* MIT Press, 1983.